A Thesis Submitted for the Degree of PhD at the University of Warwick

http://go.warwick.ac.uk/wrap/1990

Passive Permeation in Model Biological Membranes

by

John M. A. Grime

Thesis

Submitted to the University of Warwick

for the degree of

Doctor of Philosophy

Depts. of Chemistry and Physics

June 2008

THE UNIVERSITY OF
WARWICK

Contents

List of Tables v

List of Figures ix

Acknowledgments xxii

Declarations xxiii

Abstract xxiv

Abbreviations xxvi

Chapter 1 Introduction 1

Chapter 2 Surfactants 4

2.1 Introduction 4

2.2 Phospholipids - biological surfactants 5

2.3 Experimental monolayer formation 7

2.4 Experimental bilayer formation 8

Chapter 3 Electrochemistry and electrodes 12

3.1 Introduction 12

3.2 Redox reactions 13
3.3 Electrode kinetics 15
3.4 Mass transport 16
    3.4.1 Diffusion 17
    3.4.2 Convection 17
    3.4.3 Migration 18
    3.4.4 The Nernst-Planck equation 18
3.5 Scanning electrochemical microscopy (SECM) 19
3.6 UME Manufacture 20

Chapter 4 Laser confocal scanning microscopy **23**
4.1 Introduction 23
4.2 Selective excitation and emission: fluorescein 25

Chapter 5 Finite element models **29**

Chapter 6 Molecular Dynamics **32**
6.1 Introduction 32
6.2 The force field 33
    6.2.1 Intermolecular forces 34
    6.2.2 Intramolecular forces 36
6.3 Integration 39
6.4 Practicalities 41
    6.4.1 Periodic boundary conditions 41
    6.4.2 Treatment of the electrostatic potential 43
    6.4.3 Thermostat 46
6.5 Calculation of average properties 48

6.5.1 Umbrella sampling and the Weighted Histogram Analysis Method (WHAM) 51

Chapter 7 Oxygen permeation in phospholipid monolayers 54

7.1 Introduction 54

7.2 Experimental materials and methods 55

7.2.1 Reagents 55

7.2.2 Apparatus and methods 56

7.3 FEM simulation details 58

7.4 MD simulation details 61

7.5 Results 64

7.6 Conclusion 83

Chapter 8 Weak acid permeation in lecithin bilayers 84

8.1 Introduction 84

8.2 Weak acid permeation and Overton's Rule 90

8.3 Experimental materials and Methods 92

8.3.1 Reagents 92

8.3.2 Apparatus and methods 92

8.4 FEM simulation details 95

8.5 Results 97

8.6 Conclusion 105

Chapter 9 Weak acid permeation in POPC bilayers 107

9.1 Introduction 107

9.2 Experimental materials and Methods 110

9.2.1 Reagents 110

9.2.2 Apparatus and methods 110

9.3 FEM simulation details 111

9.4 MD simulation details 112

9.5 Results 114

9.6 Conclusion 125

Chapter 10 Mass transport in the unstirred layer 126

10.1 Introduction 126

10.2 FEM simulation details 129

10.3 Results 131

10.4 Conclusion 143

Chapter 11 Conclusions and further work 145

List of Tables

7.1 Oxygen molecule parameters for the MD simulation of permeation in DSPC monolayers, after Vrabec [67] and Galbraith [68]. Listed are the Lennard-Jones radius and well depth : σ and ϵ, the LJ site separation L and quadrupole moment Q. 61

7.2 First order rate constants for the transfer of oxygen across two phospholipid monolayers, as determined from finite element models as described in the text 66

7.3 Mean surface tension, γ, standard deviation (bracketed) and surface pressure Π for the three simulated monolayer systems (see Eqn. (7.10)). 70

7.4 Mean and standard deviation (bracketed) of the angle formed between the major axis of the lipid acyl tails and the interfacial normal, $\hat{n} = (0, 0, -1)$, for the Sn1 and Sn2 chains of the simulated DSPC monolayers at $z < 0$ and $z > 0$. See Fig. 7.9 72

7.5 Heights of the simulation free energy barriers for the acyl and interfacial regions (A_a, A_i), and the height of the interfacial free energy barrier normalised against the acyl region (A_i/A_a). Data listed under the headings "$-z$" and "$+z$" to denote the positions of the respective monolayers, see Fig. 7.4. 80

7.6 Predicted increases in the rate limiting excess free energy barriers for oxygen permeation, according to experimental rates from Table 7.2, for a DSPC monolayer under varying levels of compression. 82

7.7 Predicted rates of permeation given the simulated monolayer results and assuming APL 60 $\AA^2$ as the reference system. 82

8.1 Lipid and lipid-type components of various human cell membranes by percentage [91]. 85

8.2 Selected lipid components of soybean lecithin. 87

8.3 Diffusion coefficients, $\mathrm{pK_a}$ values and bulk pH measurements for the FEM model. Taken from [75]. 95

8.4 Permeation coefficients from various weak acid permeation studies (units of 10^{-4} cm s^{-1}). All studies used egg PC, except DMPC in [95] and soybean PC in this study. The results from [95] represent two values if P, measured in the gel phase (20 ° C) and the liquid phase (26 ° C). 102

9.1 Diffusion coefficients, $\mathrm{pK_a}$ values and bulk pH measurements for the POPC FEM simulations. pH$_P$ denotes the measured bulk pH for the pure POPC experimental bilayers, pH$_{Pc}$ denotes the bulk pH for the mixed POPC/cholesterol bilayer experiments. P_{Pc} for acetic acid is missing due to later analysis revealing that the BLM was in contact with the UME tip at the time of measurement, and hence the data was ignored. 112

9.2 Comparison of P values, determined via the combined LCSM/FEM method, for a homologous series of weak acids in planar bilayers formed from soybean lecithin (P_l), POPC (P_P) and a POPC/cholesterol mixture (P_{Pc}). Units are 10^{-4} cm s^{-1}. 115

9.3 Details of the POPC/weak acid MD simulations performed with $\delta z = 1.0\mathring{A}$ and $k = 25$ kJ mol^{-1}. *Insertion window* refers to the region on the x, y plane in which a low energy insertion point was sought for the weak acid, see Fig. 9.4. The surface tension, γ, was evaluated according to Eqn. (7.10) for all the individual simulations in a particular set, with standard deviation, σ, as listed. 120

9.4 Details of the POPC/weak acid MD simulations performed with $\delta z = 0.5\mathring{A}$ and $k = 50$ kJ mol^{-1}. *Insertion window* refers to the region on the x, y plane in which a low energy insertion point was sought for the weak acid, see Fig. 9.4. The surface tension, γ, was evaluated according to Eqn. (7.10) for all the individual simulations in a particular set, with standard deviation, σ, as listed. 123

10.1 Compositions by concentration (mM) of the simulated systems, from [5]. Species are labelled as follows: NaSal, sodium salicylate; Sal, salicylic acid; NaCit, trisodium citrate; NaPhos, trisodium phosphate. 129

10.2 Modelled species and respective diffusion coefficients for the FEM simulations of the USL. All D values are taken from [75]. *Cit* refers to constituents of the citrate buffer used in the *cis* chamber, and *Phos* relates to the components of the phosphate buffer in the *trans* chamber. Note that the same D values are used for all buffer species of the same family; this is not expected to significantly affect the findings. 130

10.3 Equilibria and pK$_a$ values used in the FEM simulations of the USL. All pK$_a$ values are taken from [75], and are activity corrected using the Davies formulation [126]. *Cit* refers to constituents of the citrate buffer used in the *cis* chamber, and *Phos* relates to the components of the phosphate buffer in the *trans* chamber. 131

10.4 Fluxes measured experimentally by Gutknecht and Tosteson [5] for the systems simulated in this chapter. 139

10.5 P values for a range of weak acids as measured experimentally by Walter and Gutknecht [6]. 139

10.6 Maximum flux values ($\mathsf{J}_{\mathsf{max}}$) measured in the simulated systems (see Table 10.1), and the P values which produced them, along with approximately half the maximum measured flux values ($\approx \mathsf{J}_{\mathsf{max}}/2$) and the P values which produced them. Data is given for the three values of δ discussed in this chapter. Units of flux are mol cm^{-2} s^{-1}, and units of P are cm s^{-1}. 143

10.7 Values of flux and P predicted by Eqn. (10.1) for the data listed in Table 10.6. The predicted fluxes are generated from the known δ, D, P and concentrations in the simulated systems. The predicted P values follow a similar method, but instead use the fluxes as determined by the simulations. Units of flux are mol cm^{-2} s^{-1}, and units of P are cm s^{-1}. 144

List of Figures

2.1 The structure of the phospholipids dimyristoyl phosphatidylcholine (DMPC, left) and distearoyl phosphatidylcholine (DSPC, right). 5

2.2 Illustration of simple structures formed by amphipathic molecules.
a: monolayer formed at aqueous (light) and oily (dark) phases.
b; bilayer formed from two monolayers, with same colour scheme for aqueous and oily phases. In this case, the oily phase may be formed by the lipid tails themselves. 6

2.3 Illustration of complex phases formed by phospholipids.
a: micelle (aqueous exterior region), **b**: inverse micelle (aqueous interior region),
c: vesicle (separate aqueous interior and exterior regions). 6

2.4 Example of an experimental Langmuir trough of the type used in this thesis. 7

2.5 Illustration of the formation of a Langmuir monolayer. Left to right; lipids dissolved in a nonpolar solvent (eg. chloroform) are deposited on the aspirated surface of a Langmuir trough, and the nonpolar solvent evaporates to leave a monolayer at the air/water interface. 8

2.6 Bilayer formation via the “dipping” method. A pierced PTFE sheet is lowered into a Langmuir monolayer, and a bilayer is formed in the central channel. . . 9

2.7 Bilayer formation via the “patch clamp” method. A capillary or other suitable implement is lowered into a Langmuir monolayer under positive hydrostatic pressure, before being withdrawn to remove a section of the monolayer. The capillary is then lowered once again, forming a bilayer in the central channel. 10

2.8 Bilayer formation via the “painting” method. The bristles of a fine brush, dipped in a suitable solution of lipids, is drawn across the opening where the bilayer is intended to form. The lipids are deposited, and after a certain amount of time a single bilayer forms in the central channel. 10

3.1 Illustration of the Fermi level, E_f, in a metal electrode (grey box) and the electron transfer process to an acceptor molecule (white box) as defined by the relative HOMO and LUMO states of the acceptor. **a**; the equilibrium condition. **b**; under the applied *negative* potential, the Fermi state of the metal rises, until it is higher than the LUMO of the acceptor species, which is then reduced (**c**). 14

3.2 Assorted electrode geometries, shown from the top down and in a slice through the profile view. 15

3.3 Illustration of diffusion on macro- and microelectrodes. White regions are insulating sheath, grey are electrochemically active regions. **a**: macroelectrode mass transport dominated by planar diffusion to the active region of the electrode tip, creating a depleted region of reactants and limiting the reaction kinetics. **b**: ultramicroelectrodes, with relatively large contributions from lateral diffusion and shorter length scales, allow mass transport to the tip unhindered by the formation of a depletion layer. 16

3.4 UME manufacture for the electrodes used in this work. **a**: the capillary is heated in a coil, and a force is applied to induce a tapering. **b**: the capillary is severed in the tapered region. **c**: a Pt wire is introduced to the capillary, and sealed in via heating the tip before polishing with rotating discs of progressively finer abrasive (**d**). Finally, the tip is polished microscopically smooth against a polishing cloth with Al_2O_3 paste (**e**). 22

3.5 Conventional light microscope image of the tip of a 25 μm diameter Pt UME. The apparent flaws on the surface are residual fluid and debris from the polishing process, and were easily removed by rinsing with water. 22

4.1 The principle of confocal microscopy; two pinhole apertures allow a precise focal plane to be created, greatly reducing interference from other regions of the sample. 24

4.2 Illustration of the confocal principle as applied to a 3-D system of interest. The individual focal planes from a number of samples of a 3-D system can be recombined into a good approximation of the original geometry, with data on the interior of the system also available. 25

4.3 Illustration of the image improvement offered by LCSM (left) compared to a conventional widefield fluorescence microscope image (right) of mouse intestine. Images courtesy of Molecular Expressions, the Florida State University. . . . 26

4.4 The structure of the fluorophore fluorescein. Protonation sites are on the phenolic group (labelled **1**, pK_a 6.5 [31]), the carboxylic group (**2**, pK_a 4.4 [32])and, at very low pH, the carbonyl group marked **3** (pK_a 2.1). 27

4.5 Illustration of pH vs. intensity of fluorescence after fluorescein excitation at 488 nm and detection at 530 nm a room temperature. Experimental data courtesy of Dr. N. C. Rudd. 28

5.1 Illustration of finite difference mesh approximations. From left to right; target system geometry, coarse resolution mesh approximation, finer resolution mesh approximation. See also Fig. 5.2. 30

5.2 Illustration of finite element mesh approximation. Note greater level of detail on the central curve, and contrast the variable mesh resolution with Fig. 5.1. 31

6.1 Illustration of the definition of r_{ij}, as used in the nonbonded potentials . . . 34

6.2 Illustration of the definition of a basic bond between sites i and j, with intrasite separation r_{ij} 37

6.3 Illustration of a basic angle definition, θ, between sites i, j and k 38

6.4 Illustration of a basic dihedral definition, ϕ, between sites i, j, k and l 39

6.5 Periodic images of a two dimensional simulation cell. Only nearest neighbour cells on the lateral axis are depicted (dashed lines), with the actual simulation cell central and delineated with a solid line. Also shown is the treatment of the movement of sites into and out of the simulation cell 42

6.6 Periodic images of a two dimensional simulation cell. Only nearest neighbour cells are depicted (dashed lines), with the actual simulation cell central and delineated with a solid outline. Also shown is the minimum image convention separation between bound sites i and j, $r_{ij'}$ (solid line), and the non-minimum image convention separation r_{ij} (dotted line). 43

6.7 Illustration of the Gaussian charge contributions to the Ewald sum. **a**; representation of the interacting sites as point charges, **b**; addition of point charges, screening charge distributions and compensatory charge distributions recovers the original point charges, **c**; the reciprocal space contributions to the Ewald sum as shown in neighbouring periodic cells 44

6.8 Illustration of the umbrella sampling technique. Left to right: overlapping probability histograms from independent simulations with harmonic biasing potentials; excess free energy fragments determined from Eqn. (6.29) and the process of alignment to create a unified description of excess free energy across all the simulations. 52

7.1 Structure of the phospholipids DMPC (a) and DSPC (b). Both surfactants feature an identical phosphatidylcholine head group, with 14 and 18 carbon groups in the acyl "tails" of DMPC and DSPC respectively. 56

7.2 **a**: Schematic of experimental apparatus. A Langmuir trough allows the controlled formation of lipid monolayers at the air/water interface, while a submarine UME induces the reduction of the oxygen permeating into the aqueous phase. **b**: Detail of the transfer of oxygen through the monolayer, where it is reduced at the exposed Pt wire in the centre of the electrode tip. This reduction generates a measurable current, and hence the determination of rate constants for the permeation. 57

7.3 Axisymmetric FEM geometry used to determination experimental values for the k', the first order rate constant for oxygen transfer across the a monolayer, which is the only adjustable parameter in the model. The simulated distance between the electrode and the interface, d, is progressively reduced to model the approach of the submarine UME to the experimental Langmuir monolayer. 60

7.4 *a*: Schematic of symmetrical DSPC monolayers around a TIP3P water box as used in the simulations. *b*: Illustration of symmetrical insertion and harmonic restraining potentials for oxygen permeant molecules at reaction coordinate z. Restraints act on the centres of mass of the oxygen molecules and the remainder of the system, with the minimum energy of the restraint at centre of mass separation $z = z_0$ 63

7.5 Selected normalized steady-state diffusion limited current vs. UME-interface separation for the reduction of oxygen at a DMPC monolayer. From top to bottom, the dashed curves correspond to the experimental approach to a clean interface and surface pressures of 0, 10, 20 and 35 mN m^{-1}. The solid lines represent a clean theoretical approach (no lipid barrier present), and $k'/10^{-8}$ = 6.76, 3.16, 1.9, and 1.18. The experimental results are readily reproducible to distances of circa 2 μm, at which point experimental deformation processes of the monolayer may vary dependent on the precise geometry of the UME tip. 65

7.6 Selected normalized steady-state diffusion limited current vs. UME-interface separation for the reduction of oxygen at a DSPC monolayer. From top to bottom, the dashed curves correspond to the experimental approach to a clean interface and surface pressures of 0, 10, 20 and 35 mN m^{-1}. The solid lines represent a clean theoretical approach, and $k'/10^{-8}$ = 5.68, 3.7, 2.8, and 2.32. 66

7.7 Surface pressure, Π vs experimental permeation rate constant k for DMPC and DSPC monolayers, with lines of best fit. 68

7.8 Illustration of the lipid tail major axis tilt angle (a) and S_{CD} order parameter angle (b). Interfacial normal is labelled $\hat{n}$ 71

7.9 Tilt angle distributions of the lipid tail major axis and the interfacial normal $\hat{n} = (0, 0, -1)$ for simulated monolayers at APL 55 (solid line), 57.5 (dashed line) and 60 $\AA^2$ (dotted line). See also Table 7.4. **a**: Sn1 chain. **b**: Sn2 chain. 72

7.10 $|S_{CD}|$ order parameters for the simulated monolayers at APL 55 $\AA^2$. Solid lines denote the Sn1 chain, dotted lines the Sn2 chain. **a**: $z < 0$. **b**: $z > 0$. 73

7.11 $|S_{CD}|$ order parameters for the simulated monolayers at APL 57.5 $\AA^2$. Solid lines denote the Sn1 chain, dotted lines the Sn2 chain. **a**: $z < 0$. **b**: $z > 0$. 74

7.12 $|S_{CD}|$ order parameters for the simulated monolayers at APL 60 $\AA^2$. Solid lines denote the Sn1 chain, dotted lines the Sn2 chain. **a**: $z < 0$. **b**: $z > 0$. 74

7.13 Density profile for the simulated monolayers of APL 55 $\AA^2$. Note pronounced "shoulders" in the density profiles of TIP3P and acyl CH$_2$ at $z \approx 20\AA$. . . . 75

7.14 Density profile for the simulated monolayers of APL 57.5 $\AA^2$. 76

7.15 Density profile for the simulated monolayers of APL 60 $\AA^2$. Note slight "shoulder" in the density profile of acyl CH$_2$ at $z \approx 20\AA$. 76

7.16 Excess free energy profiles for the 3 simulated monolayer systems; APL of 55 $\AA^2$ (solid line), 57.5 $\AA^2$ (dashed line) and 60 $\AA^2$ (dotted line). The heights of the free energy barriers at the apex of the curves in the acyl and interfacial regions (see Fig. 7.4 b, and Table 7.5) are relative to the free energy nadir in the vacuum region immediately beyond the monolayers. 78

7.17 Excess free energy profile for the simulated monolayer system of APL of 55 $\AA^2$. 78

7.18 Excess free energy profile for the simulated monolayer system of APL of 57.5 $\AA^2$. 79

7.19 Excess free energy profile for the simulated monolayer system of APL of 60 $\AA^2$. 79

8.1 A basic bilayer structure; the acyl tails of two monolayers are arranged to minimise contact with water, creating two headgroup/aqueous interfaces on the bilayer exterior and a hydrocarbon-rich "oily" interior region. 85

8.2 Structures of some common membrane components (see Table 8.1): **a**, cholesterol; **b**, sphingomyelin; **c**, phosphatidylethanoylamine based lipid; **d**, phosphatidylserine based lipid; **e**, phosphatidylcholine based lipid. Note the net negative charge on the phosphatidylserine head group. 86

8.3 Schematic of standard BLM permeation apparatus; the permeating species is introduced to the *cis* chamber (left)and the concentration change in the *trans* chamber is examined. Mechanical stirring of the solutions in either chamber is used to reduce the width of the unstirred layer (USL). The combined permeative process is a serial combination of transport in the bulk solution and permeation through the membrane itself. 89

8.4 Illustration of the local pH perturbation induced by galvanostatic UME controlled oxidation of water. Protons are generated at the UME tip, generating a concentration profile along the axis marked z. This proton concentration profile is visualised via LCSM in the presence of a pH sensitive fluorescent dye, with higher pH giving a larger fluorescence signal (see Fig. 4.5) 90

8.5 Illustration of the "step" introduced in a UME controlled proton concentration profile by the presence of a BLM; the BLM presents a barrier to the free diffusion of protons (see Fig. 8.4) which is easily identifiable in the presence of a pH sensitive fluorescent dye under LCSM visualisation. The BLM effectively prevents proton diffusion beyond the BLM, other than those carried through the BLM by a weak acid mediator. 91

8.6 Schematic of the PTFE cell arrangement. Two PTFE sections form the upper and lower chambers, with holes for pressure equilibration [105]. The dipping lens of a LCSM is positioned at a working distance of circa 2 mm above the bilayer to inspect the formation of proton gradients. 93

8.7 Schematic of the FEM geometry and boundaries (see text for conditions). . . 96

8.8 Illustration of Bezier curve fit to pH vs. fluorescence intensity of fluorescein. Solid line denotes the experimental data (see Fig. 4.5), dashed line the Bezier fit. 98

8.9 Fluorescence-distance plots normal to the center of the microelectrode: **(a)** Bezier fit to the experimental fluorescence profile of acetic acid, **(b)** fitted simulation data for P (units 10^{-4} cm s^{-1}) from FEM calculations of acetic acid under the experimental conditions and geometry. 99

8.10 Experimental fluorescence profile for a propionic acid solution of pH 7.1, with diffusion unhindered by the presence of a BLM. Simulated fluorescence profiles for three separate bulk pH values (6.8, 7.0, 7.2) are also shown to illustrate the robust nature of the LCSM/FEM technique with respect to bulk pH. 100

8.11 Fluorescence profiles for three separate bulk pH values, with $P = 10^{-3}$ cm s^{-1}. Left; raw profiles, right; profiles normalised at 300 μm, illustrating the relative insensitivity of the system to the bulk pH. 101

8.12 Fluorescence profiles for three separate bulk pH values, with $P = 5 \times 10^{-3}$ cm s^{-1}. Left; raw profiles, right; profiles normalised at 300 μm, illustrating the relative insensitivity of the system to the bulk pH. 101

8.13 Fluorescence profiles for three separate bulk pH values, with $P = 10^{-2}$ cm s^{-1}. Left; raw profiles, right; profiles normalised at 300 μm, illustrating the relative insensitivity of the system to the bulk pH. 101

8.14 Fluorescence-distance plots normal to the center of the microelectrode: **(a)** valeric acid, **(b)** hexanoic acid. Units of P are 10^{-4} cm s^{-1}. 102

8.15 **(a)** P vs acyl length; **(b)** P vs water/octanol partition coefficient, K ($\log_{10}$ scale); **(c)** P vs water/olive oil partition coefficient, K ($\log_{10}$ scale). Key for **b**, **c**: solid line denotes data from this study, dotted line from [107] and dashed line [6]). All K values taken from [107] and [6]. Note that partition coefficient data was not available for the same weak acids in the two studies cited. . . . 103

8.16 **(a)** Simulated pH profile (left) and experimental pH profile (right) for the permeation of hexanoic acid. Bilayer position is marked with a solid line in the simulated profile, and a dashed line in the experimental profile. **(b)** Illustration of the LCSM scan plane with respect to the experimental bilayer (see also Fig. 8.6). 105

9.1 Structures of POPC (left) and cholesterol (right). 108

9.2 Illustration of the location of cholesterol in a typical lipid bilayer. Hydrophilic groups are shown in red, and hydrophobic groups in green. Note - cholesterol is not shown to scale with respect to the lipid molecules, and as such this diagram is purely illustrative. 109

9.3 Structures of protonated weak acids used in the MD simulation of permeation in a POPC bilayer. Left to right; acetic, butanoic and hexanoic acid. 113

9.4 Illustration of the location of the weak acid insertion windows as detailed in Table 9.3. 113

9.5 Illustration of typical experimental geometries for the POPC and POPC/cholesterol BLMs. Left; pure POPC BLM in propionic acid solution. Right; POPC/cholesterol BLM formed in propionic acid solution. Note that the differing pH values measured in each system make comparisons by eye difficult. 114

9.6 Fluorescence profiles for acetic acid in a pure POPC bilayer. Left; profile to 300 μm, right; profile to 100 μm. 115

9.7 Fluorescence profiles for propionic acid (left) and butanoic acid (right) in a pure POPC bilayer. 116

9.8 Fluorescence profiles for valeric acid in a pure POPC bilayer. 116

9.9 P vs water / octanol partition coefficient, $K_{octanol}$ (left) and P vs water / olive oil partition coefficient, $K_{oliveoil}$ (both log10 scale). Valeric acid P for pure POPC bilayer is highlighted. See Table 9.2. 117

9.10 Acyl tail length vs P for the weak acid permeants in pure POPC and mixed POPC/cholesterol bilayers. See Table 9.2. 118

9.11 Fluorescence profiles for propionic acid (left) and butanoic acid (right) in a POPC / cholesterol bilayer. 118

9.12 Fluorescence profiles for valeric acid (left) and hexanoic acid (right) in a POPC / cholesterol bilayer. 119

9.13 MD density profiles for selected groups (left) and the total density profile (right) for the latter 4 ns of the POPC bilayer simulation equilibrations. 120

9.14 MD S_{CD} order parameter for the latter 4 ns of the POPC bilayer equilibration. 120

9.15 Excess free energy profiles for a protonated acetic acid molecule in a POPC bilayer. Left; Acetic 1. Right; Acetic 2 (see Table 9.3). 121

9.16 Excess free energy profiles for a protonated butanoic acid molecule in a POPC bilayer. Left; Butanoic 1. Right; Butanoic 2 (see Table 9.3). 122

9.17 Excess free energy profiles for a protonated hexanoic acid molecule in a POPC bilayer. Left; Hexanoic 1. Right; Hexanoic 2 (see Table 9.3). 122

9.18 Relative errors for the Butanoic 1 and Butanoic 2 simulation sets (see Table 9.4). 123

9.19 RMS deviation from the initial insertion position on the x, y plane for the MD simulations detailed in Table 9.19. 124

9.20 Excess free energy profiles for protonated acetic (left), butanoic (middle) and hexanoic (right) acids using a staggering of 0.5 $\mathring{A}$ on the z coordinate and a restraining potential with $k = 50$ kJ mol^{-1}, see Table 9.4. 124

10.1 Illustration of the traditional permeation study, with two stirred chambers separated by a BLM; the permeant species is added to the *cis* chamber, and the change in concentrations in the *trans* chamber is measured. Where permeation through the BLM is fast, the rate limiting step may be the mass transport of protons, along with both the charged and neutral species, through the bulk solution and USL. 127

10.2 The 1-D FEM geometry used in the simulations. The boundary conditions at the exterior of the *cis* and *trans* chambers are the bulk concentrations for each species i, $c^*_{i,\text{cis}}$ and $c^*_{i,\text{trans}}$. Flux across the central bilayer is determined as shown, with r the special coordinate. 129

10.3 Surface plot for flux in the unbuffered *cis* system of pH 3.9. Flux contours are shown as coloured lines as in the boxed key. 132

10.4 Surface plot for flux in the unbuffered *cis* system of pH 4.9. Flux contours are shown as coloured lines as in the boxed key. 133

10.5 P vs flux in the unbuffered *cis* system of pH 3.9 for three USL widths, see Fig. 10.3. Error bars are generated from USL width ± 10%. 133

10.6 P vs flux in the unbuffered *cis* system of pH 4.9 for three USL widths, see Fig. 10.4. Error bars are generated from USL width ± 10%. 134

10.7 Surface plot for flux in the buffered *cis* system of pH 4.9. Flux contours are shown as coloured lines as in the boxed key. 136

10.8 P vs flux in the buffered *cis* system of pH 4.9 for three USL widths, see Fig. 10.7. Error bars are generated from USL width ± 10%. 136

10.9 USL location vs pH for the systems in Table 10.1. Clockwise from top left; $\delta = 50$ μm, $\delta = 250$ μm and $\delta = 500$ μm. The graphs are discontinuous at the location of the BLM in the centre of the simulations. 137

10.10 Left column; concentration profiles for the protonated weak acid carrier, HX, when P is set such that the BLM flux is half of the maximum flux achieved in the simulations. Right column; concentration profiles for protonated weak acid carrier where the largest simulated flux was attained. Rows from top to bottom; $\delta = 50$ μm, 250 μm and 500 μm. 141

10.11 Left column; concentration profiles for the weak acid anion, [X$^-$], when P is set such that the BLM flux is half of the maximum flux achieved in the simulations. Right column; concentration profiles for protonated weak acid carrier where the largest simulated flux was attained. Rows from top to bottom; $\delta = 50$ μm, 250 μm and 500 μm. 142

Acknowledgments

First and foremost I would like to thank my supervisors, Profs. Mike Allen and Pat Unwin, for their invaluable support, advice and enthusiasm. Thanks are also due to Prof. Mark Rodger for help and advice in using the DL_POLY molecular dynamics code, and to Dr. Nicola Rudd for help and advice in the experimental aspects of this thesis.

The *Molecular Organisation and Assembly in Cells* (MOAC) doctoral training centre under the careful guidance of Prof. Alison Rodger has provided an agreeably stimulating and diverse working environment these past four years; I would like to take this opportunity to formally recognise the fine efforts of all involved, and their contributions to my development.

Special mention should be made of the input of Martin Edwards, whose uncanny ability to reduce complex problems into a simple function of alcohol and rugby has proven priceless, and to the affectionate support of Christina Evans, whose frequently bizarre anecdotes and timely interventions have ensured my sanity remains largely intact.

A final heartfelt thanks is owed to Roger and Ann, my parents, and my brothers Paul and Mike. It was your unstinting support that made this possible.

Declarations

The work contained in this thesis is entirely original and my own work, except where acknowledged in the text. I confirm that this thesis has not been submitted for a degree at another university.

Abstract

The subject of this thesis is the study of mass transport using experimental and theoretical techniques, specifically the investigation of transport through phospholipid barriers which serve as a model for biological systems. To this end, experimental monolayer and bilayer membranes are produced, and the permeation of gas and weak acid molecules is quantitatively measured.

Potentiostatic measurement of oxygen permeation in monolayers formed using two varieties of phospholipid at the air/water interface, under varying levels of compression (and hence surface pressure), was performed using ultramicroelectrodes, followed by finite element simulations to parameterise the approach curves produced and hence determine the first-order rate constant for the permeation process. As expected, the rate of permeation decreases significantly as the monolayers are compressed, with a simple surface pressure model proving insufficient to describe these trends. Molecular dynamics simulations are employed to investigate the excess free energy barriers for permeating oxygen molecules using umbrella sampling and the weighted histogram analysis method. The results are shown to be unreliable in their description of the permeation process.

Experimental bilayers are formed from lecithin, pure POPC, and a mixture of POPC and cholesterol in a supporting electrolyte solution. The permeation of a homologous series of protonated weak acids is studied using laser scanning confocal microscopy to selectively excite and detect the state of fluorescein, a dye with pH-sensitive fluorescence intensity. These experimental results are again parameterised with finite element models, and the trend of decreasing permeation coefficient as the weak acid molecules increase in size is reported. This is in direct contradiction to the established *Overton's Rule*. Molecular dynamics simulations of the permeation of three of the weak acids in a POPC bilayer is performed to determine excess free energy profiles using umbrella sampling, combined with the weighted histogram analysis method. Serious flaws are found in the method and execution of this aspect of the work.

Abbreviations

AMBER	Assisted Model Building with Energy Refinement
CHARMM	Chemistry at Harvard Molecular Modelling
BLM	Bilayer Membrane
DLPOLY	Daresbury Laboratories Poly-modeller
DMPC	Dimyristoyl Phosphatidyl Choline
DPPC	Dipalmitoyl Phosphatidyl Choline
DSPC	Distearoyl Phosphatidyl Choline
FDM	Finite Difference Method
FEM	Finite Element Model
GROMACS	Groningen Machine for Chemical Simulations
HOMO	Highest Occupied Molecular Orbital
LCSM	Laser Confocal Scanning Microscopy
LUMO	Lowest Unoccupied Molecular Orbital
MD	Molecular Dynamics
NVT	Constant particle count (N), volume (V), temperature (T)
PC	Phosphatidyl Choline
PE	Phosphatidyl Ethanolamine
POPC	1-Palmitoyl-2-Oleoyl Phosphatidyl Choline
PS	Phosphatidyl Serine
PTFE	Polytetrafluoroethylene
UME	Ultramicroelectrode
WHAM	Weighted Histogram Analysis Method

Chapter 1

Introduction

From the smallest unicellular organisms to the largest of multicellular creatures, we find structures embedded in structures - each with varying degrees of thermal and chemical isolation from their surroundings. Life requires barriers, which on the largest scales might involve collections of specialised cells, as in the skin, and on the smallest scales may consist of films the width of a single molecule. This work examines permeation in models of the biological barriers which help to regulate various cellular processes, and also provide a controlled boundary to maintain homeostasis.

Even in the membranes of cells as ostensibly different as the bacterium *Staphylococcus* and the human erythrocyte, one may find surprisingly conserved structural motifs. On a fundamental level, such cell membranes consist of a variety of amphipathic phospholipids combined with a huge array of support molecules, and additional proteins with specific functions in cell adhesion, signalling and transport. Where the latter aspect requires the use of energy, in the sodium/potassium pumps of neurons for example, the transport is described as *active*.

The scope of this thesis is restricted to the study of *passive* transport; that is, the permeation of substances through a medium along a concentration gradient and without additional energy expenditure or specialised transport structures. The aim of the thesis is to examine the passive permeation of a variety of molecular species across biologically relevant phospholipid barriers. A combination of experimental and theoretical techniques will be employed to gain a deeper understanding of the permeation processes, and novel methods of experimental data collection and numerical analysis are introduced. Any weaknesses in traditional studies will be highlighted in the context of these new techniques, and potential solutions to overcome such weaknesses will be discussed where appropriate.

Chapters 2 to 6 detail the techniques used in this thesis; Chapter 2 introduces the concept of surfactants, certain experimental methods of monolayer and bilayer production. Chapter 3 explains some basic properties of electrochemical systems, with a particular focus on aqueous electrochemistry and small-scale electrodes. The next three chapters (Chapters 4 to 6) outline the experimental and theoretical techniques which form the basis of the work in this thesis, specifically laser scanning confocal microscopy, finite element models and molecular dynamics simulations.

Initially, the transport of gaseous oxygen across Langmuir monolayers at the air/water interface will be studied in Chapter 7; monolayers of varying composition and levels of compression are examined to determine what effects these parameters exert. Experimental data is accumulated via SECM, and numerical analysis is performed with a FEM of the system of interest. Molecular dynamics studies of one of the model systems is used to provide an estimate for the free energy barriers the permeating oxygen might encounter in the monolayer structures.

Chapters 8 and 9 introduce a combined SECM/FEM method of determining the permeation coefficients of a series of homologous weak acid protonophores. The experimental system involves the use of SECM and LCSM, with permeation coefficients determined via FEM models of the experimental geometry and chemical composition. Molecular dynamics studies are once again employed to examine the microscopic free energy barriers, in this instance for a model POPC bilayer system.

Chapter 10 examines the theoretical behaviour of the traditional methods of gathering such information, with a particular emphasis on the limitations and weaknesses of those techniques which might lead to disagreements between the various previous studies. A previously published experimental system is used as the basis for the models studied, and analysis of the mass transport properties of this system provide a basis for the discussion of such systems in a general sense, with conclusions drawn as to the limits of previous work.

The final section, Chapter 11, discusses the work as a whole, and draws together the various aspects of passive transport studied in this thesis, with a particular focus on the experimental implications for permeative processes which are potentially limited by mass transport. Potentially interesting directions for future study are suggested.

Chapter 2

Surfactants

2.1 Introduction

Surfactants are substances which reduce interfacial tension by aggregating at the boundary region between liquids and gases [1, 2], the interfaces of immiscible liquid phases or the transition of solids to other states of matter. Interfacial tension arises naturally from the difference in attractive forces experienced by molecules in the bulk and interfacial regions; in the bulk, a molecule is surrounded by others of the same type, and the attractive forces experienced lead to a low energy state compared to the same molecule at an interface, where only partial surrounding (and hence, fewer attractive interactions from a certain direction) takes place. Where differing attractive forces act between separate species (eg. water and oil), we find that energy is required to create an interface between the two and hence any such shared surfaces between will tend to minimise in area. It is therefore typical to observe two immiscible phases aligning in such a manner that the interfacial surface area shared between the two is minimised, for example a film of oil forming on top of water rather than dissolving or forming droplets in the bulk aqueous phase.

A substance will therefore display surfactant properties due to its molecular structure [1]; typically, surfactants feature a region which is soluble in a particular phase connected to a region which is relatively insoluble in the same medium; the aggregation of surfactants at an interface, and the resultant lowering of the surface tension, is therefore a natural effect of the partition of the surfactant between the phases producing a system with subsequently lower free energy at the interface.

2.2 Phospholipids - biological surfactants

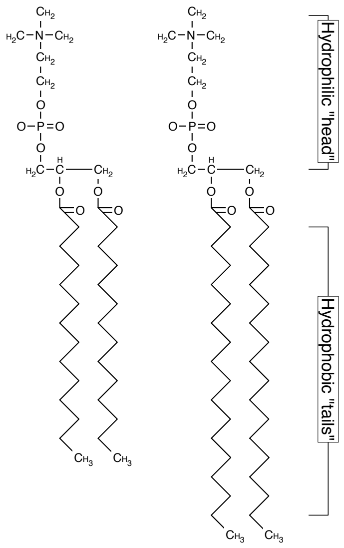

Figure 2.1: The structure of the phospholipids dimyristoyl phosphatidylcholine (DMPC, left) and distearoyl phosphatidylcholine (DSPC, right).

Phospholipids consist of both a hydrophilic polar head region and one or more hydrophobic tail groups, generally carbon chains (eg. DMPC and DSPC, Fig. 2.1). The hydrophilic head groups, when combined with the hydrophobic nature of the tails, will produce phase separation in aqueous solution to maximise the exposure of the head groups to the water while minimising the contact between water and the tail groups.

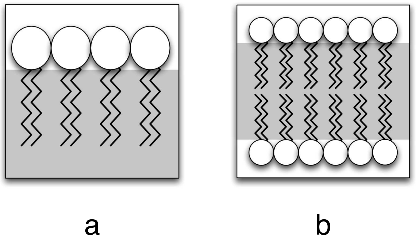

Figure 2.2: Illustration of simple structures formed by amphipathic molecules.
a: monolayer formed at aqueous (light) and oily (dark) phases.
b; bilayer formed from two monolayers, with same colour scheme for aqueous and oily phases. In this case, the oily phase may be formed by the lipid tails themselves.

It is this amphipathic nature which allows the formation of monolayers in a binary mixture of polar/nonpolar solvents (Fig. 2.2 a) and may lead to bilayers in a purely polar solvent (Fig. 2.2 b).

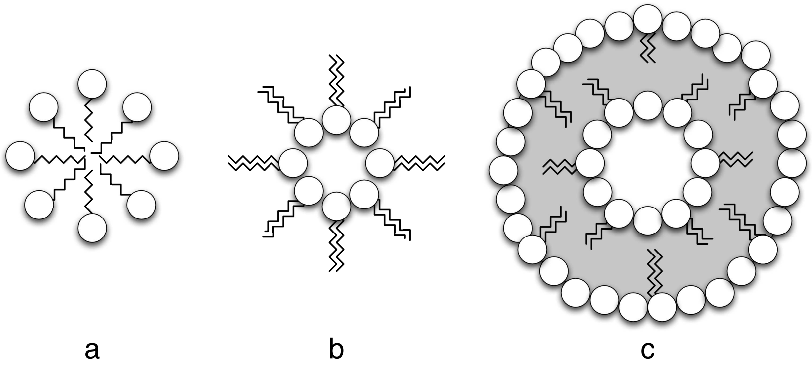

Figure 2.3: Illustration of complex phases formed by phospholipids.
a: micelle (aqueous exterior region), **b**: inverse micelle (aqueous interior region), **c**: vesicle (separate aqueous interior and exterior regions).

The exact nature of the structures formed in polar solution depends, amongst other things, on the relative size of the head groups, the concentration of the phospholipid, the number of hydrophobic tails and the presence of certain other substances [3] (Figs. 2.3 a,b,c).

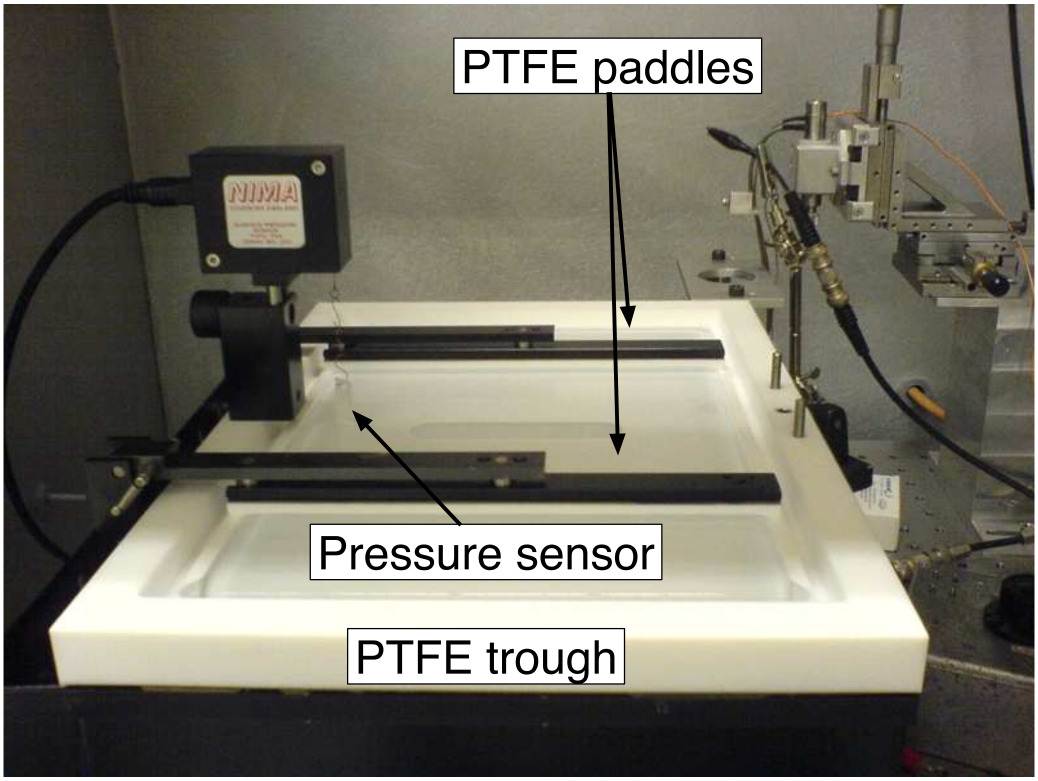

Figure 2.4: Example of an experimental Langmuir trough of the type used in this thesis.

2.3 Experimental monolayer formation

The hydrophilic head group and hydrophobic tail group of a typical phospholipid molecule typically prevent effective solution in aqueous phases. This is frequently used to experimental advantage in the controlled production of monolayers in a *Langmuir trough*, see Fig. 2.4; many phospholipid types readily dissolve in non-polar solvents such as chloroform, and when such a solution is carefully deposited on the surface of an aqueous phase the resultant evaporation of the solvent leads to the formation of a phospholipid monolayer at the air/water interface (see Fig. 2.5). The presence of movable "paddles" at the interface, when combined with a suitable pressure sensing apparatus, allows ex-

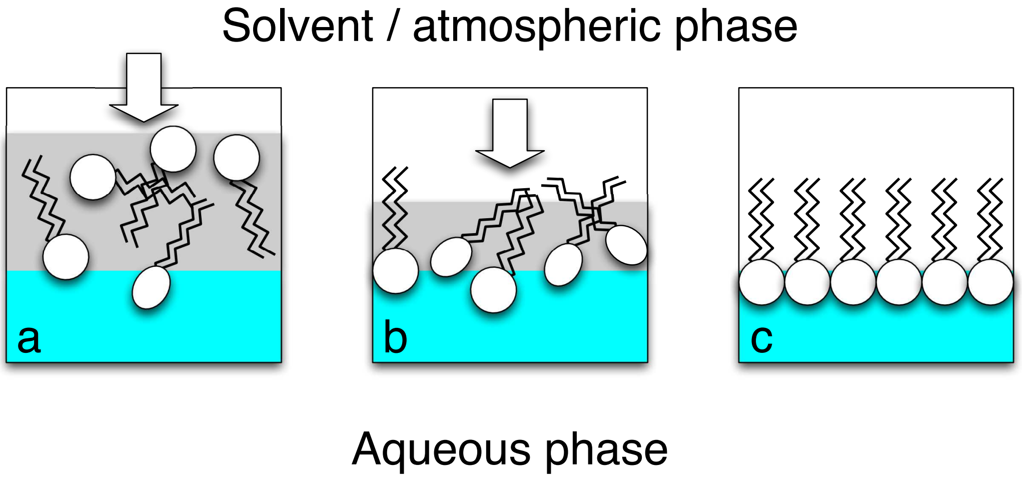

Figure 2.5: Illustration of the formation of a Langmuir monolayer. Left to right; lipids dissolved in a nonpolar solvent (eg. chloroform) are deposited on the aspirated surface of a Langmuir trough, and the nonpolar solvent evaporates to leave a monolayer at the air/water interface.

perimental investigation of monolayers at various surface pressures and area per lipid values. Extensive use of such experimental apparatus is made in Chapter 7 to study the permeation of atmospheric oxygen through a variety of phospholipid monolayers.

2.4 Experimental bilayer formation

Phospholipids, like other surfactants, will spontaneously self-assemble into a variety of structures given appropriate conditions. There are a number of experimental methods which can specifically produce bilayers, the most common of which can be grouped under the labels of *dipping*, *patch clamps* and *painting*.

The dipping method [4] relies on the large energies associated with exposure of the lipid tails to ionic solutions such as water. By introducing a punctured PTFE sheet vertically through a Langmuir monolayer (Fig. 2.6), it is possible to encourage the

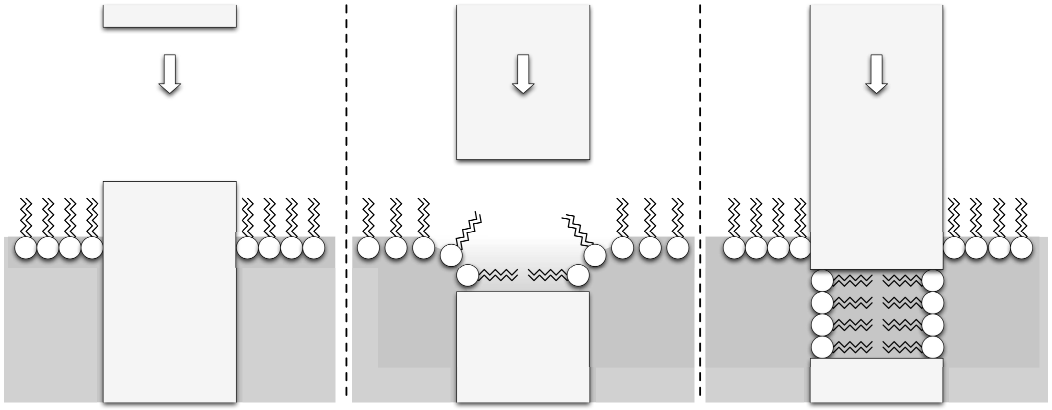

Figure 2.6: Bilayer formation via the "dipping" method. A pierced PTFE sheet is lowered into a Langmuir monolayer, and a bilayer is formed in the central channel.

formation of a bilayer in the central gap formed by the perforation; as the two sides of the monolayer are "dragged" down into solution, the tendency to minimise exposure of the tails to water causes them to align such that they preserve their monolayer structure contiguous with their original neighbours, while the head groups simultaneously remain in contact with the aqueous phase in a process analogous to the closing of a zip. This method is useful in studies of aqueous permeation between two adjacent chambers; if the PTFE sheet is arranged as a separating barrier between the chambers, it is then simple to aspirate the surface to remove the monolayer and introduce the permeant into one of the chambers before monitoring the concentration increase over time in the other chamber [5–7].

The use of a patch clamp to form bilayers [8] also relies on the presence of a monolayer at the air/water interface; a narrow capillary (the eponymous patch clamp) is filled with water and lowered down into the monolayer while maintaining an aqueous efflux from the tip to prevent the lipids agglomerating in the opening of the capillary. The tip is then raised in the absence of flow; the hydrophilic head groups of some of

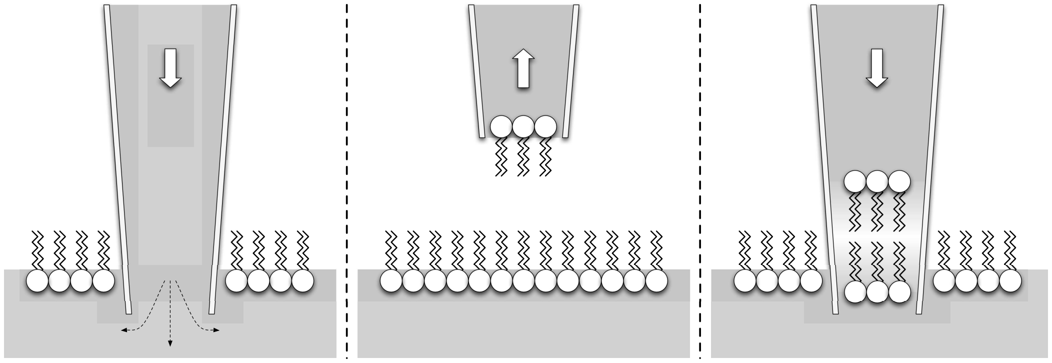

Figure 2.7: Bilayer formation via the “patch clamp” method. A capillary or other suitable implement is lowered into a Langmuir monolayer under positive hydrostatic pressure, before being withdrawn to remove a section of the monolayer. The capillary is then lowered once again, forming a bilayer in the central channel.

the lipids now adhere to the secondary, newly formed air/water interface in the opening of the capillary, and a monolayer is formed with orientation opposite to the original system (Fig. 2.7). When the patch clamp is introduced for a second time, the newly formed monolayer is “pushed up” by the tails of the original monolayer - which has since recovered from the disruption caused by the earlier application of the patch clamp. Hence, a bilayer is formed in the opening of the capillary.

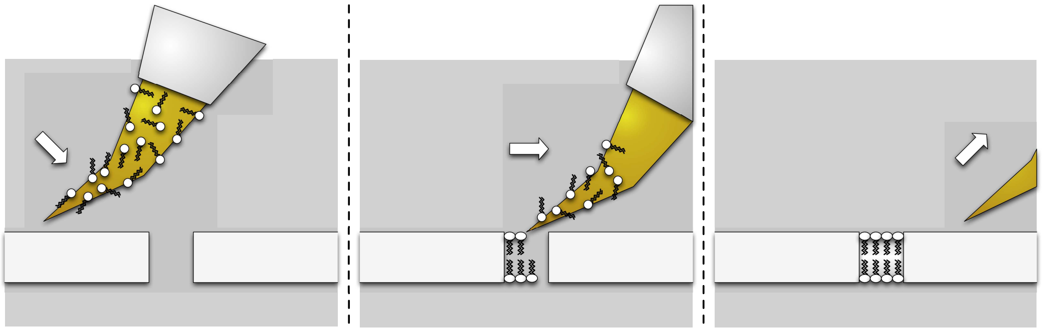

Figure 2.8: Bilayer formation via the “painting” method. The bristles of a fine brush, dipped in a suitable solution of lipids, is drawn across the opening where the bilayer is intended to form. The lipids are deposited, and after a certain amount of time a single bilayer forms in the central channel.

The final method discussed in this work is the painting, or paintbrush method [9]. A fine brush is introduced to a concentrated solution of lipids, and the bristles are gently draw across a small opening in a PTFE sheet (Fig. 2.8). The lipids are deposited in the PTFE channel, and this deposition results in a bilayer forming. Bilayers rarely form instantly with the paintbrush method; typically, a nonplanar deposition of lipids takes place in the opening which acts to support the bilayer before the solvent and excess lipid are expelled to the exterior of the of the channel and the final bilayer structure forms. This technique, although rudimentary, is effective despite the somewhat arbitrary nature of the lipid placement and is the method used in all experimental bilayer studies contained in this thesis.

Chapter 3

Electrochemistry and electrodes

3.1 Introduction

The first scientific recognition of the differences between magnetism and static electricity is attributed to Gilbert's *De Magnete* [10], but it was almost a further 150 years before Du Fey determined the existence of positive and negative charges in static electricity [11]. These repulsive and attractive charges were later elucidated in the work of Priestley [12] and in the 1785 and 1787 memoirs of Coulomb to the *Academie Royale des Sciences* [13].

By 1800, Volta demonstrated apparatus for the chemical generation of electrical currents [14], but it was not until the research of Faraday that the unification of the electrical fields began; before this point the static, "Voltaic" and electromagnetic effects were not generally recognised as being closely related.

Of great importance to experimental electrochemistry was the work of Nernst, who deployed thermodynamics to describe the behaviour of ions in solution. Through these techniques, Nernst derived a relationship between the chemical reactions in a galvanic cell and the potential difference produced.

The descriptions of the relationship between chemical reactions, potential differences and electrical current allow the rigorous investigation of a variety of phenomena using electrochemical techniques. When such methods are combined with an accurate description of mass transport it becomes possible to create detailed theoretical models of experimental systems, to the extent that one may feasibly determine unknown rate constants and transport processes via numerical simulations.

3.2 Redox reactions

The movement and sharing of electrons between substances is of fundamental importance to chemistry. A process where a species loses electrons, while another species gains electrons, is described as a *redox* reaction (with *red*uction being the gain of electrons, and *ox*idation the conjugate loss). Electrons reside in a variety of discrete energy levels (described as *orbitals*) in a substance, selectively filling orbitals with progressively higher energy levels according to the Pauli exclusion principle. As such, the HOMO (highest occupied molecular orbital) is the orbital with the highest energy containing one or more electrons, and the LUMO (lowest unoccupied molecular orbital) is the next orbital "up" from the HOMO in terms of energy.

A metal contains many close-packed atoms which have overlapping orbitals, and as a result the discrete energy levels attainable by an electron become a continuum, with the *Fermi level* denoting the energy of the most energetic electrons. If a *negative* potential energy is applied to a metal, the Fermi level *increases* and an electron may be donated to an adjacent electrochemically-active molecule (which is "reduced") provided the Fermi level is larger than the LUMO of the acceptor molecule. Alternatively, if a *positive* applied potential moves the Fermi level of a metal below the HOMO state of an

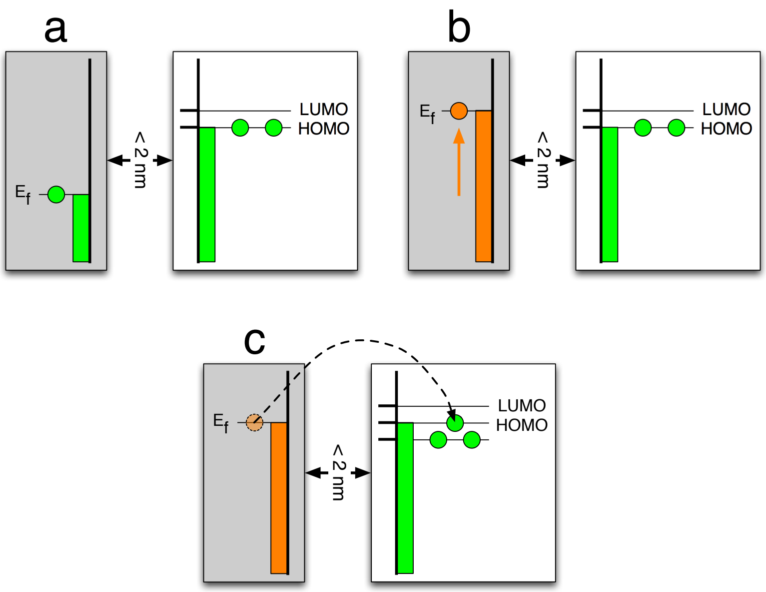

Figure 3.1: Illustration of the Fermi level, E_f, in a metal electrode (grey box) and the electron transfer process to an acceptor molecule (white box) as defined by the relative HOMO and LUMO states of the acceptor. **a**; the equilibrium condition. **b**; under the applied *negative* potential, the Fermi state of the metal rises, until it is higher than the LUMO of the acceptor species, which is then reduced (**c**).

adjacent molecule, that molecule can be "oxidised" and donate electrons to the metal. It is therefore possible to generate a potential-dependent flow of electrons to or from a metal electrode, causing redox reactions with nearby molecules. An illustration of this process may be seen in Fig. 3.1.

The simplest experimental system includes a working electrode (the location of the redox reactions) and a reference electrode relative to which the applied potential is measured. Where the typical current is expected to be greater than 100 nA, a three electrode arrangement (working, reference and auxiliary electrodes) is to be preferred to prevent the current polarising the reference potential due to the relatively high current density [15]. All experimental work detailed in this thesis uses currents of less than

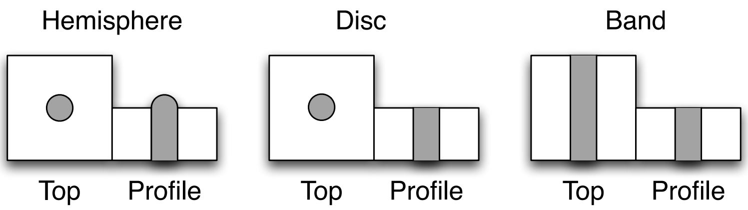

Figure 3.2: Assorted electrode geometries, shown from the top down and in a slice through the profile view.

10nA, and a two-electrode arrangement is therefore sufficient.

The current which flows in such a system may be limited by the kinetics of electron transport at the working electrode (see 3.2) or the rate at which the redox-active molecules can reach the working electrode; the latter case is an example of *mass transport* limited electrochemistry (see 3.4), where the movement of electrons (and hence the current) is dependent on the rate at which the redox active species can be supplied to the electrochemically active region of the electrode tip.

3.3 Electrode kinetics

The dynamical properties of an electrode are dependent on its size. The *ultramicroelectrodes* (UMEs) which re the focus of this work typically have one dimension around 25 μm or less [15]. Although this restriction allows for a number of configurations, including hemispheres discs and bands (see Fig. 3.2), this work will focus on the use of disc UMEs.

The restricted dimensions of the UME convey certain benefits over conventional, larger electrodes; they can provide relatively high *mass transport* (see 3.4) due to the hemispherical diffusion which occurs (Fig. 3.3), giving a faster response time and pre-

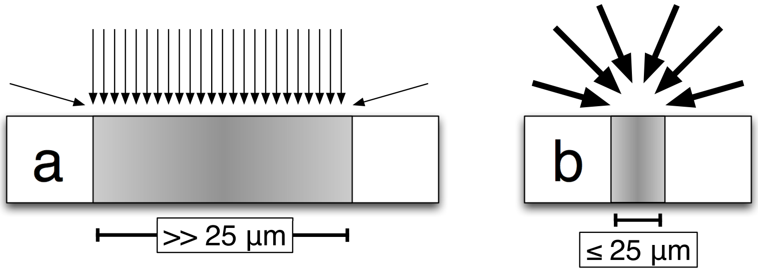

Figure 3.3: Illustration of diffusion on macro- and microelectrodes. White regions are insulating sheath, grey are electrochemically active regions. **a**: macroelectrode mass transport dominated by planar diffusion to the active region of the electrode tip, creating a depleted region of reactants and limiting the reaction kinetics. **b**: ultramicroelectrodes, with relatively large contributions from lateral diffusion and shorter length scales, allow mass transport to the tip unhindered by the formation of a depletion layer.

venting the formation of any depletion zone of exhausted reactants which might act to *decrease* the electrode kinetics after an initial, temporary maximum. The steady state redox-induced current, i_{ss}, measured at a disc UME is described by the equation [15]:

$$i_{ss} = KnFaDc^* \tag{3.1}$$

where K is 4 for a disc electrode, n the number of electrons transferred in the electrode reaction, F is Faraday's constant, a the UME radius, D the diffusion coefficient of the reacting species and c^* its concentration.

3.4 Mass transport

Mass transport describes the movement in solution of a species of interest. Factors which contribute to mass transport include diffusion (movement along a concentration gradient), convection (the directed movement of the solution itself carrying the species) and migration of the species (for example, the directed motion of ions due to some applied electrostatic potential). An increase in any of these factors can promote mass transport, alleviating a possible rate limiting factor in reactions with fast electrode kinetics. To precisely quantify electrode reactions, it is therefore necessary to take each aspect of mass transport into consideration.

3.4.1 Diffusion

Where a system is in equilibrium, and the density distribution of the species of interest in solution does not change over time, flux due to diffusion may be described with the familiar *Fick's first law*, which connects a concentration gradient to flux via the diffusion coefficient of the species of interest:

$$J_{d,i} = -D_i \nabla c_i \quad . \tag{3.2}$$

Here, D_i is the diffusion coefficient of species i, with ∇ representing a partial derivative - in this case, the partial derivative of the concentration of the species of interest, c_i. Where the system is *not* in equilibrium, and the density distributions change in time, *Fick's second law* states:

$$\frac{\partial c_i}{\partial t} = D_i \nabla^2 c_i \quad . \tag{3.3}$$

3.4.2 Convection

Convective fluxes carry reactants to the electrode due to the overall movement of the solution itself, and the contribution to the overall flux is therefore a function of the velocity of the solution, V, and the concentration of the species of interest in that solution:

$$J_{c,i} = c_i V \quad . \tag{3.4}$$

A controlled artificial convective flux can be introduced to promote mass transport using a number of techniques, including rotating disc electrodes [15] and impinging fluid microjets [16]. Natural convective currents, from sources such as a thermal gradient, are difficult to control or fully eliminate, but they can be minimised via temperature control.

3.4.3 Migration

The migration of charged species can be induced by the application of a suitable electrostatic potential, which supplies a driving force to move ions in solution,

$$J_{m,i} = -\frac{z_i F}{RT} D_i c_i \nabla\phi \quad . \tag{3.5}$$

The flux is connected to this migration via z_i, the charge on species i, Faraday's constant F, D_i - the diffusion coefficient of species i, and the derivative of the electrostatic potential field, $\nabla\phi$. Here, T is the absolute temperature and R is the gas constant (the product of Boltzmann's constant and Avogadro's number). Migration is typically difficult to quantify precisely; however, the addition of a supporting electrolyte not only lowers the resistance of the solution, but also acts to reduce migratory fluxes. Where the ratio of supporting electrolyte to migratory ionic species is 100:1 and higher, the migratory contribution to the resultant overall flux is less than 1% [17].

3.4.4 The Nernst-Planck equation

The combined effects of diffusion, convection and migration may be expressed by the Nernst-Planck equation [15]:

$$\begin{aligned} J_i = &-D_i \nabla c_i \\ &+ c_i V \\ &- \frac{z_i F}{RT} D_i c_i \nabla\phi \quad . \end{aligned} \tag{3.6}$$

All mass transport models of fluxes in this thesis involve the addition of sufficient supporting electrolyte to render migration insignificant. The processes modelled also occur over very short ranges in relatively uniform solutions, with no net flow at room temperature; as such, it is assumed that the effects of natural convection may be safely discounted. The resultant models make use of only the diffusive aspects of the Nernst-Planck equation, significantly simplifying any numerical analysis of experimental results.

3.5 Scanning electrochemical microscopy (SECM)

Scanning electrochemical microscopy (SECM) dynamically positions an electrode tip, generally a UME, on one or more axes. This technique allows the investigation of targeted regions of a system, and given suitable UMEs and controlling machinery (piezoelectric positioners or micrometers) can attain sub-micron resolutions [18] dependent on the size of the electrode tip.

The precise nature of the positioning controllers is highly dependent on the problem domain the user wishes to study; for scanning over 2-D regions of a sample, it is obvious that control on the x, y axes is mandatory. On the other hand, where only a simple approach to some interface is required, a lone z axis positioner may well suffice. The hardware used to control the SECM tip can range from piezoelectric positioners [19] (which can provide nanometre to micrometre spatial resolution) to stepper motors [20, 21] which can be somewhat less accurate. Even a manual control system with differential micrometer can offer surprisingly high spatial resolution [22, 23] of ± 0.25 μm, but such systems are considerably less convenient than automated control - to say nothing of the steady hand the experimentalist would require to follow such a protocol.

The configuration of the SECM probe itself may use a large number of materials and follow a number of geometries, among these mercury hemispherical UMEs and platinum disc and UMEs (for example, [24] and [2] respectively). This thesis concerns itself solely with Pt disc UMEs, but for a overview of other geometries the reader is directed to Bard and Faulkner [15].

SECM is generally performed in either an amperometric or potentiometric regime [18]. As the name suggests, an amperometric SECM experiment allows the measurement of the current which results from a redox process induced by the application of a certain potential difference to the UME tip and some appropriate reference electrode. The (typically small) currents which result may then be amplified via a current-to-voltage converter before recording with suitable equipment. A potentiometric SECM system involves the application of a specified current, and the recording of the potential difference which must be applied to the UME tip maintain this current with respect to some reference electrode. The SECM studies performed in this work involve both amperometric and potentiometric modes, and the technique used will be specified where appropriate.

The applications of SECM to interfacial electrochemistry are widespread. For a limited set of example, the technique has been applied to air/water interfaces to study gas permeation [2], liquid/liquid interfaces [25], and liquid/solid interfaces [25, 26]. For further examples, Edwards *et al* [18] have produced a comprehensive review.

3.6 UME Manufacture

All UMEs used in this work were manufactured according to the process illustrated in Fig. 3.4. Borosilicate glass capillaries of outer and inner diameter 2 mm and 1.16 mm (Harvard Apparatus, Kent, UK) was heated in a pipette puller (Narashige PB-7, Narashige Ltd, Japan) with an applied tension on the lower barrel to produce a tapered midsection. After cutting the capillary along the central tapered region, an $\approx$5 mm length of 25 μm Pt wire (Goodfellow Ltd, Huntingdon, UK) was introduced into the thinnest end of one section, with $\approx$ 1 mm exposed outside the capillary, where the glass was then sealed by rotation in a bunsen burner flame. Coarse flattening of the electrode tip was achieved with cabrimet papers (240 and 600 grit, Beuhler, Coventry, UK). A series of impregnated diamond polishing discs (grade 9 μm to 0.1 μm, Buehler, Coventry, UK) was used with a home-made polishing wheel (ensuring the electrode was held normal to the polishing surface) to progressively reduce any surface roughness before final polishing in an 0.05 μm Al_2O_3 powder/distilled water paste on a fine polishing cloth (both Buehler, Coventry, UK). At each stage of polishing, the electrode surface was checked for imperfections under a light microscope (Olympus BH2-UMA with Nomarski objectives: x50 to x1000) until a visibly smooth interface was produced (Fig. 3.5).

After polishing, an electrical connection between the internal Pt wire and a connecting lead was produced via the application of silver-loaded epoxy resin to the interior Pt wire and the exposed tip of the lead, allowing 12 hours for the epoxy to harden. The connection was tested, and the open end of the electrode was sealed with Araldite Rapid (Bostik Ltd, Leicester) before a minimum of 12 hours in an oven as allowed for hardening.

Before every set of experiments, the tip of the UME was repolished with 0.05 μm Al_2O_3 powder/distilled water paste on a fine polishing cloth (both Buehler, Coventry, UK).

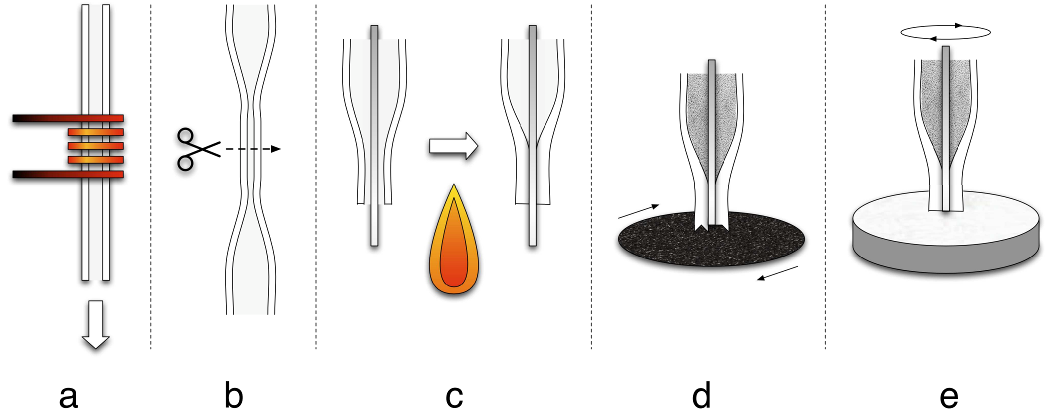

Figure 3.4: UME manufacture for the electrodes used in this work. **a**: the capillary is heated in a coil, and a force is applied to induce a tapering. **b**: the capillary is severed in the tapered region. **c**: a Pt wire is introduced to the capillary, and sealed in via heating the tip before polishing with rotating discs of progressively finer abrasive (**d**). Finally, the tip is polished microscopically smooth against a polishing cloth with Al_2O_3 paste (**e**).

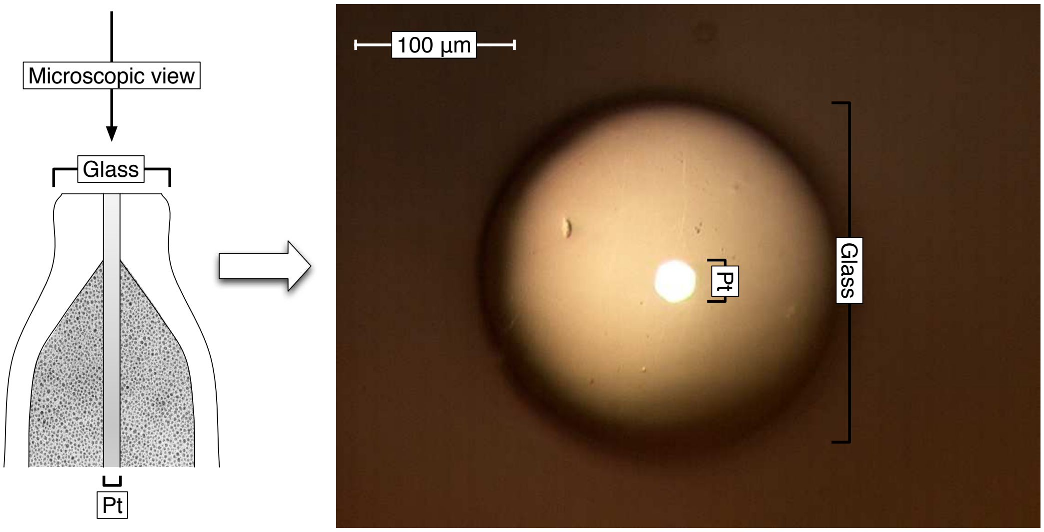

Figure 3.5: Conventional light microscope image of the tip of a 25 μm diameter Pt UME. The apparent flaws on the surface are residual fluid and debris from the polishing process, and were easily removed by rinsing with water.

Chapter 4

Laser confocal scanning microscopy

4.1 Introduction

Conventional "wide field" light microscopy, while relatively cheap and accessible, can suffer from a lack of precision in terms of the focal plane due to the illumination of large portions of the sample. As the technique relies on the reflection or transmission of light, the resultant focal plane may be poorly defined and subject to interference from matter which lies outside the region of interest. Confocal microscopy [27, 28] drastically reduces the out-of-plane interference by introducing two pinhole apertures at the light source and detecting apparatus of the microscope; this has the benefit of allowing the efficient filtering of light from regions outside the focal plane which may otherwise contribute to the signal. A basic schematic of the confocal microscopy principle is shown in Fig. 4.1. When used in conjunction with positioners which allow controlled scanning over a sample [28], high resolution 2-D or 3-D images with resolution on the micron scale can

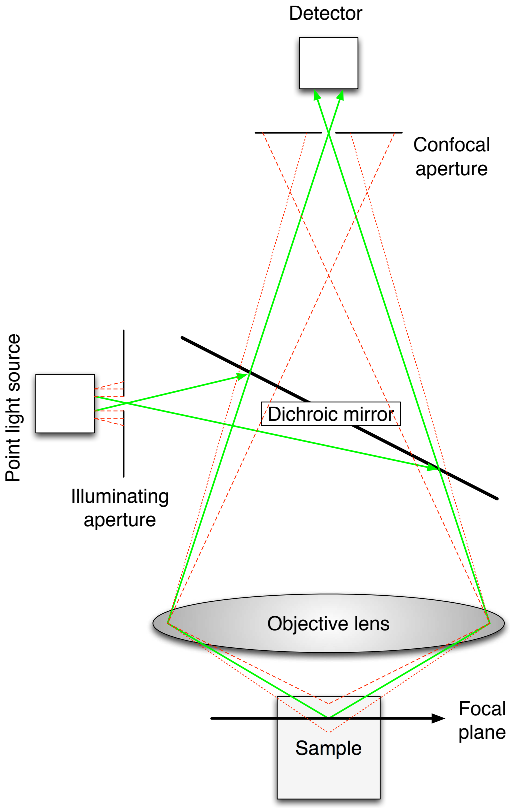

Figure 4.1: The principle of confocal microscopy; two pinhole apertures allow a precise focal plane to be created, greatly reducing interference from other regions of the sample.

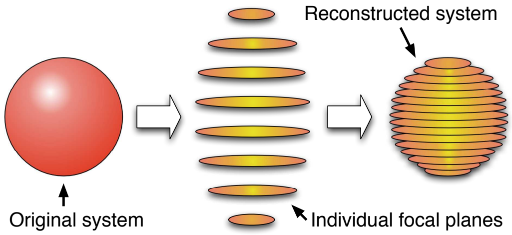

Figure 4.2: Illustration of the confocal principle as applied to a 3-D system of interest. The individual focal planes from a number of samples of a 3-D system can be recombined into a good approximation of the original geometry, with data on the interior of the system also available.

be produced for a variety of systems [29] by the sampling and subsequent recombination of a number of focal planes into a single data set (Fig. 4.1). This technique has the additional benefit of allowing the examination of the "interior" of systems which might otherwise be limited to views of some external coating or process.

4.2 Selective excitation and emission: fluorescein

Scanning confocal microscopy is particularly effective when combined with the precise laser excitation of fluorescent dyes, which can subsequently emit light of a sufficiently different wavelength to allow separation of the signals; where an electron is struck by radiation of a specific wavelength (and hence frequency, the reciprocal of wavelength, with lower wavelengths having greater energies), it can be excited from the usual "ground state" into one or more "excited states" of a higher energy. The electron may then relax, for example through proximity with other molecules [30] or the subsequent emitting of radiation at a lower wavelength. The discrepancy between the wavelength of radiation which excites an electron, and the wavelength of fluorescent light which is emitted when the electron returns to the ground state, is known as a *Stokes shift*. As

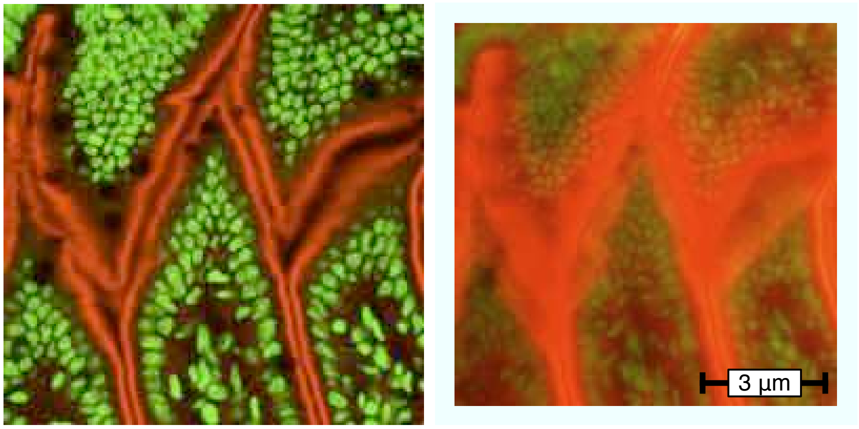

Figure 4.3: Illustration of the image improvement offered by LCSM (left) compared to a conventional widefield fluorescence microscope image (right) of mouse intestine. Images courtesy of Molecular Expressions, the Florida State University.

the absorbance and emittance wavelengths can be quite specific to individual molecules, it is possible to identify the location and structure of such molecules using the LCSM technique. A representative illustration of the image quality provided by LCSM, compared to conventional laser excited wide-field light microscopy, can be seen in Fig. 4.3.

A common fluorophore for use with the LCSM technique is fluorescein, Fig. 4.4. Fluorescein has 2 groups which act as weak acids (sites **1** and **2** from Fig. 4.4), and a further group able to protonate at low pH (site **3** from Fig. 4.4) Where sites **1** and **2** are deprotonated (pH circa 5 and above), the molecule absorbs radiation at a wavelengths of around 496 nm, and emits at approx. 518 nm [33] - giving it a Stoke's shift of circa 24 nm. At low pH, where the doubly and triply-protonated species dominate, the fluorescence signal is weak in experimental measurement. The specific intensity of the fluorescence is therefore dependent on the local pH (Fig. 4.5); it is this property of fluorescein which makes it useful in the non-invasive study of local pH gradients with

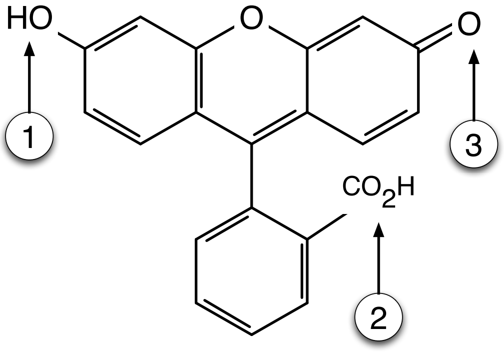

Figure 4.4: The structure of the fluorophore fluorescein. Protonation sites are on the phenolic group (labelled **1**, pK_a 6.5 [31]), the carboxylic group (**2**, pK_a 4.4 [32])and, at very low pH, the carbonyl group marked **3** (pK_a 2.1).

LCSM for a biologically relevant pH range.

The use of LCSM and fluorescein as a pH dependent probe of local pH is fundamental to Chapters 8 and 9.

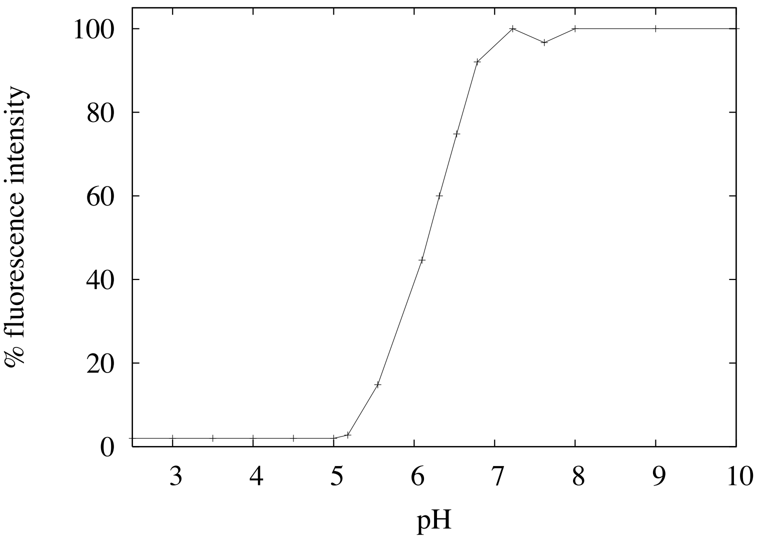

Figure 4.5: Illustration of pH vs. intensity of fluorescence after fluorescein excitation at 488 nm and detection at 530 nm a room temperature. Experimental data courtesy of Dr. N. C. Rudd.

Chapter 5

Finite element models

Physical systems are frequently modelled in terms of the way in which they change in response to one or more variables, including time. Given a set of differential equations which describe these changes, and their effects on the system of interest, it becomes possible to determine properties of the system which are not explicit in the differential equations themselves.

For complicated systems, such as those involving the movement of large numbers of molecules and the reactions they are subject to, the ability to analytically "solve" (ie. integrate) the differential equations becomes impossible. Hence, numerical methods of integration become essential. Two of the common approaches to solve such problems are "finite difference" methods and "finite element" methods.

A finite difference method (FDM) generally relies on the discretisation of the problem such that the differential equation may be approximated in matrix form as combinations of the discretised points, and then solved as simultaneous equations. Alternatively, the differential equation may be evolved in one or more parameters, typically time, to achieve successive solutions given some starting point.

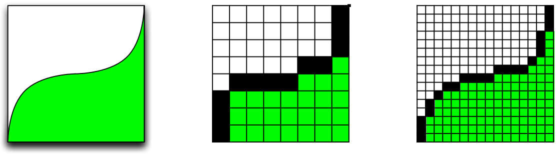

Figure 5.1: Illustration of finite difference mesh approximations. From left to right; target system geometry, coarse resolution mesh approximation, finer resolution mesh approximation. See also Fig. 5.2.

Although FDMs have been used to model chemical systems in terms of mass transport [34, 35] and reaction equilibria [36, 37], they have the disadvantages of a general requirement for equidistantly spaced points on the problem domain; although more sophisticated (and therefore complicated) expressions of the problem may allow heterogeneous spacing of the discretised points, the FDM is effectively limited to approximating the geometry of interest using a regular mesh, with squares or cubes etc on the spacial degrees of freedom. This ensures that modelling curved surfaces, for example, becomes problematic; a greater number of discretisation points may be used to allow finer detail, but at the cost of a greater computational overhead (Fig. 5.1).

Finite element models (FEMs) utilise a different approach. Whereas a finite difference model is an approximation to the differential equation, the FEM approximates the solution itself. An in-depth discussion of the finite element method is non-trivial, and will not be covered in this thesis. Those interested are directed towards standard a text such as Zimmerman's [38]. Briefly, the differential equation is convoluted with a so-called "basis function" of known form, and partial integration produces a separate set of equations which may be numerically solved in matrix form. The use of appropriate basis functions allows more sophisticated treatment of the problem geometry, allowing variable size and distribution of the individual "elements" used to describe the system

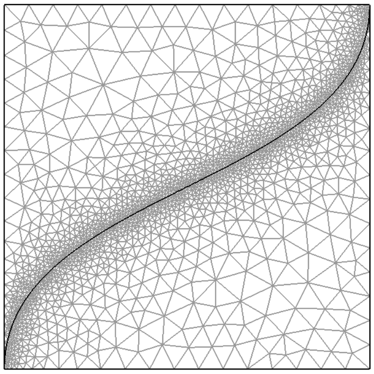

Figure 5.2: Illustration of finite element mesh approximation. Note greater level of detail on the central curve, and contrast the variable mesh resolution with Fig. 5.1.

(Fig. 5.2). Boundaries to the simulation are typically held at a constant value (*Dirichlet* boundary condition) or at a constant derivative (*von Neumann* boundary condition).

The finite element simulations performed in this work use the COMSOL Multiphysics toolkit (COMSOL Inc., Burlington, MA, USA) for the MATLAB software (The MathWorks Inc, Natick, MA, USA), a standard and well regarded numerical toolkit for the mathematical modelling of a variety of systems. COMSOL presents a simple user interface to the production and evaluation of finite element models with almost arbitrarily complex geometries, and provides standard functionality to perform mass transport simulations with reacting species (see, for example, [2, 29]). The use of FEM simulations is integral to chapters 7, 8, 9 and 10

Chapter 6

Molecular Dynamics

6.1 Introduction

The origins of molecular modelling are intimately tied to the development of general purpose computing machines. Although some early work on the properties of matter was performed with physical systems such as glass beads [39] and rubber balls [40], the flexibility and speed of reproducible calculations made the dawn of molecular simulation almost inseparable from the creation of the modern computer.

Many of the seminal early studies [41] relied on the "Monte Carlo" techniques which played a central role in the Manhattan Project during World War II. Such statistical methods allow the efficient stochastic sampling of problems with large dimensionality, and can map neatly onto many thermodynamic calculations which may be of interest to the scientist. However, this section concentrates on a somewhat different approach to the simulation of the properties of matter - molecular dynamics (MD), a technique which is concerned with the numerical integration of the equations of motion for a system of interest using a discretised timestep, δt.

Despite the extraordinary increases in computational power since the advent of the first electronic devices, modern MD simulations share the same fundamental strengths and weaknesses of the pioneering MD studies; although spacial and temporal resolutions of nanometres and nanoseconds are routinely achieved for simulations considering explicit atoms, this high level of detail comes at significant computational cost - so much so that macroscopic simulations of such models are currently impossible without significant loss of structural details.

Nonetheless, useful information may be gleaned from the limited scales available to MD. Detailed and reliable descriptions of the energies associated with various molecules are freely available from a number of sources (eg. CHARMM [42], AMBER, GROMOS etc), along with many tried and tested packages to translate these energies into effective forces, and hence the equations of motion for almost arbitrary collections of atoms may be integrated to examine their dynamics.

6.2 The force field

Given a detailed description of the energies in a system (a *force field*), it is possible to derive the appropriate equations of motion and to infer thermodynamic variables such as the excess free energy. The energies can generally be divided under two main headings; *kinetic* energy (energy due to motion, K) and *potential* energy (energy due to position, V). Kinetic energy may be formulated in the familiar manner:

$$K = \frac{1}{2}m\dot{\mathbf{r}}^2 \tag{6.1}$$

with m denoting the mass of the object, and $\mathbf{r}$ its position - hence $\dot{\mathbf{r}}$ describes the velocity of the object, the first derivative of its position with respect to time. Potential energy tends to be somewhat more complex; in a molecular system there are intermolecular (“non-bonded”) contributions from electrical charges and the van der Waals forces, and intramolecular (“bonded”) interactions which act to preserve molecular structures and shapes. The equations of motion for a system may be derived via the Lagrangian, L, defined as the difference between the kinetic and potential energies [43]:

$$L = K - V. \tag{6.2}$$

Given the following equation [43],

$$0 = \frac{d}{dt}\left(\frac{\partial L}{\partial \dot{\mathbf{r}}}\right) - \frac{\partial L}{\partial \mathbf{r}} \tag{6.3}$$

it is straightforward to recover Newton’s equations of motion

$$0 = \frac{d}{dt}\left(m\dot{\mathbf{r}}\right) - \left(-\nabla V(\mathbf{r})\right) \tag{6.4a}$$

$$-\nabla V(\mathbf{r}) = m\ddot{\mathbf{r}} \tag{6.4b}$$

$$\mathbf{F} = m\mathbf{a} \tag{6.4c}$$

6.2.1 Intermolecular forces

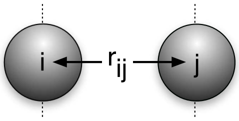

Figure 6.1: Illustration of the definition of r_{ij}, as used in the nonbonded potentials

The ideal gas model assumes that the constituent atoms of the gas do not interact. For the simulation of condensed matter, however, it is necessary to represent the interactions that atoms experience as a result of their relative arrangement; for the purposes of classical mechanics, these contributions can be broadly categorised as electrostatic interactions and van der Waals interactions, though both effects stem from the same quantum behaviour of electrons.

The simplest representation of the electrostatic interaction between two atoms is the Coulomb potential:

$$V_C = \frac{1}{4\pi\epsilon_0\epsilon_1}\frac{q_i q_j}{r_{ij}}. \tag{6.5}$$

Here, q_i and q_j are the values of point charges situated at the centres of mass of the interacting atoms and ϵ_0 is the permittivity of free space (which is multiplied by ϵ_1, the relative permittivity of the simulated medium). Although in reality the charge distribution on atoms is non-spherical, and may be influenced by the presence of other charges nearby, for large scale simulations it is common to assume that no polarisation of the atoms takes place to increase the efficiency of the calculations.

The electrostatic interactions are relatively long ranged; they decay as $\frac{1}{r_{ij}}$, and hence are time consuming to evaluate in the form of the Coulomb potential due to the potentially large number of surrounding atoms which may be influenced by any point charge. It is therefore prudent to evaluate such energies in a more sophisticated manner; one such method is the *Ewald sum* (Section 6.4.2), which relies on the separation of the electrostatic energies into real space and reciprocal space contributions, a particularly good fit with simulation techniques such as the periodic boundary condition (Section 6.4.1).

The electrostatic potential energy alone cannot reproduce all the nonbonded behaviour of interacting sites in a simulation. Consider an atom which displays no net charge or multipoles; such an atom, for example rare gases such as argon, can nonetheless display behaviour which can differ from that of an ideal gas, such as the formation of liquid and solid phases. It is therefore clear that another nonbonded potential may be necessary. One example is the familiar and eponymous *Lennard-Jones 12-6* potential

[44]:

$$V_{\mathsf{LJ}}(r_{ij}) = \begin{cases} 4\epsilon\left[\left(\frac{\sigma}{r_{ij}}\right)^{12} - \left(\frac{\sigma}{r_{ij}}\right)^{6}\right], & \text{if } r_{ij} \le r_{\mathsf{cut}}; \\ 0, & \text{if } r_{ij} > r_{\mathsf{cut}}. \end{cases} \tag{6.6}$$

here ϵ controls the depth of the potential "well" and σ defines the separation at which the *potential* is zero. The separate r_{ij}^{-6} and r_{ij}^{-12} contributions model the long ranged attractive and short ranged repulsive aspects of the van der Waals forces, respectively. An alternative formulation, as in the CHARMM force field, may be expressed as:

$$V_{\mathsf{LJ}}(r_{ij}) = \begin{cases} \epsilon\left[\left(\frac{r_{min}}{r_{ij}}\right)^{12} - 2\left(\frac{r_{min}}{r_{ij}}\right)^{6}\right], & \text{if } r_{ij} \le r_{\mathsf{cut}}; \\ 0, & \text{if } r_{ij} > r_{\mathsf{cut}}. \end{cases} \tag{6.7}$$

here r_{min} is the point at which the *force* is zero, ie. $-\nabla V_{LJ}(r_{ij}) = 0$. Note that $r_{min} = 2^{\frac{1}{6}}\sigma$.

Care should be exercised in the treatment of such potentials at their cutoff distance, r_{cut}; that is, the maximum distance at which the Lennard-Jones potential can apply. Where two interacting sites move from distance $r_{\mathsf{cut}} - \delta r$ to $r_{\mathsf{cut}} + \delta r$, the potential will be truncated in a discontinuous manner. This introduces problems with the conservation of energy in the simulation, and this is not the only issue: as $F_{\mathsf{LJ}} = -\nabla V_{\mathsf{LJ}}$, the discontinuity in the potential function at r_{cut} causes ill-specified F_{LJ} at that point. Shifted potential and force methods [45] may be used to alleviate such problems.

6.2.2 Intramolecular forces

The simplest, and most common representation for bonded atoms in a molecular modelling force field is that of the harmonic potential - effectively a Hookean spring with

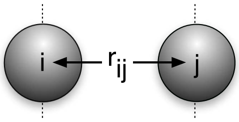

Figure 6.2: Illustration of the definition of a basic bond between sites i and j, with intrasite separation r_{ij}

separation r_{ij} (Fig. 6.2) between the bound sites:

$$V_{\text{bond}}(r_{ij}) = K_b(r_{ij} - r_0)^2 \quad . \tag{6.8}$$

By providing a reference bond length, r_0, and a spring constant K_b, it is possible to create a separation between two atoms of a defined resting distance and with tunable rigidity to suit.

The use of explicit hydrogen atoms introduces a further requirement for the description of bonding in the system. As it is wise to use an integration timestep, δt, which is capable of capturing the fastest motions in the system, the relatively high frequency vibrations of bound hydrogen would naturally produce a simulation of limited temporal scope. This problem may be alleviated somewhat by the introduction of rigid bonds; by suppressing any deviation from the resting bond length r_0, we may use a larger timestep without producing an unrealistic distribution of r_{ij}. The SHAKE algorithm [46] is one possible solution to this problem. By ensuring $r_{ij} \approx r_0$ at each step, the necessity for δt to reflect the high frequency motions of bound H is removed. This constraint is satisfied iteratively, by allowing unconstrained motion of the bound sites before retroactively applying a force to solve the constraint to a predefined tolerance.

Potentials may also be introduced to preserve a valence angle between three consecutive bound sites in a molecule by considering the angle, θ, formed between the two consecutive bonds (Fig. 6.3). As these angles are found experimentally to vary

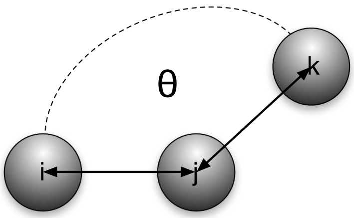

Figure 6.3: Illustration of a basic angle definition, θ, between sites i, j and k

around a single value, it is typically convenient to define such potentials as an harmonic with a known equilibrium angle θ_0:

$$V_{\mathsf{angle}}(\theta_{ijk}) = K_\theta(\theta_{ijk} - \theta_0)^2 \quad . \tag{6.9}$$

Dihedral angle potentials, sometimes referred to as torsion angle potentials, are used to constrain rotations around a certain bond. The relationship between the dihedral angle, ϕ (Fig. 6.4), and the energy may not be as straightforward as that of angle potentials, for example. To allow for more complicated functional forms, dihedral angle potentials are generally expressed as a truncated Fourier series, for example:

$$V_{\mathsf{dihedral}}(\phi) = \sum_{a=1}^{b} K_{\phi,a}(1 + \cos(n_a\phi) - \delta_a) \tag{6.10}$$

with b the number of contributions in the series, n_a the multiplicity and δ_a the phase shift for contribution a. Frequently, another four-body contribution to the force field exists in the form of an *improper dihedral potential*. Improper dihedrals are useful in the modelling of chiral centres, but they do not share the same properties as the regular dihedral potentials - specifically, they are generally expressed as a single harmonic in the form of the simple bond and angle potentials.

Typically, force fields are defined such that nonbonded contributions are ignored when considering sites which are present in the same bond or angle, as such intramolec-

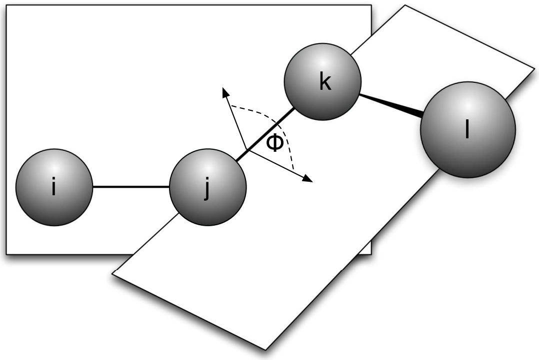

Figure 6.4: Illustration of a basic dihedral definition, ϕ, between sites i, j, k and l

ular potentials are implicitly assumed to include these effects in their definition. A special case may exist for the treatment of dihedral potentials; the i and l sites (see Fig. 6.4 - henceforth referred to as the "1-4" sites, from their positions in the dihedral specification) usually interact via a modified form of the nonbonded reactions. The electrostatic and van der Waals interactions can be scaled or fully redefined for these sites, and so the chosen force field may define dihedral 1-4 factors to describe how the standard nonbonded potentials should manifest themselves.

6.3 Integration

Given a suitable description of the force fields governing the interactions between elements in a given simulation, Eqn. (6.4c) may be used to numerically integrate the equations of motion for the system. As MD simulations typically involve a large number of interacting sites, we must consider the resultant many body problem which cannot be solved analytically; we therefore numerically integrate Eqn. (6.4c) with discretised units of time, and derive the site coordinates, velocities and accelerations. These quantities are related as follows:

$$\mathbf{v} = \dot{\mathbf{r}} = \frac{\partial}{\partial t}\mathbf{r} \tag{6.11a}$$

$$\mathbf{a} = \ddot{\mathbf{r}} = \frac{\partial}{\partial t}\dot{\mathbf{r}} \tag{6.11b}$$

Most numerical integration schemes are based on the Taylor expansion, a series expansion of a function around a specified point:

$$\begin{aligned} f(t+\delta t) = f(t) &+ \frac{1}{1!}\frac{\partial f(t)}{\partial t}(\delta t) \\ &+ \frac{1}{2!}\frac{\partial^2 f(t)}{\partial t^2}(\delta t^2) \\ &+ \frac{1}{3!}\frac{\partial^3 f(t)}{\partial t^3}(\delta t^3)\ \ldots \\ &+ \frac{1}{n!}\frac{\partial^n f(t)}{\partial t^n}(\delta t^n) \end{aligned} \tag{6.12}$$

A common approach to the integration of the equations of motion would involves a *symplectic* method which is stable over long times, conserving the total energy of the system while closely approximating the target phase space distribution; one such method is the “velocity Verlet” [47] algorithm:

$$\mathbf{r}(t+\delta t) = \mathbf{r}(t) + \mathbf{v}(t)\,\delta t + \frac{\mathbf{a}(t)}{2}(\delta t)^2 \tag{6.13a}$$

$$\mathbf{v}(t+\delta t) = \mathbf{v}(t) + \frac{\mathbf{a}(t) + \mathbf{a}(t+\delta t)}{2}\delta t \tag{6.13b}$$

where $\mathbf{r}(t)$, $\mathbf{v}(t)$ and $\mathbf{a}(t)$ are the position, velocity and acceleration vectors for the system components at the specified time. This algorithm proceeds in two stages, with the positions at time $t+\delta t$ computed as expected before the velocities are calculated at a mid step time of $t+\frac{1}{2}\delta t$:

$$\mathbf{v}\left(t+\frac{1}{2}\delta t\right) = \mathbf{v}(t) + \frac{\mathbf{a}(t)}{2}\delta t \quad . \tag{6.14}$$

The forces and accelerations at time $t + \delta t$ are now computed before the final velocity is determined:

$$\mathbf{v}\left(t + \delta t\right) = \mathbf{v}\left(t + \frac{1}{2}\delta t\right) + \frac{\mathbf{a}\left(t + \delta t\right)}{2}\delta t \tag{6.15}$$

6.4 Practicalities

Given the basic definition of the force field and the method of integrating the equations of motion, there are still certain practicalities which should be considered in a molecular dynamics simulation. The limited computational power available to the researcher inevitably leads to certain compromises regarding the scope of the system to be studied. It is possible to overcome some of these barriers using certain well-established techniques to extend the feasibility of large scale systems.

6.4.1 Periodic boundary conditions

A simple method to increase the apparent spacial scale of the simulation is to treat the volume containing the molecules as one of a series of identical, infinitely repeating volumes on one or more axes. As the typical MD model is three dimensional in nature, the MD "cell" repeats on the Cartesian x, y and z axes. This arrangement naturally lends itself to cubic or orthorhombic simulation cells, but prescriptions exist for a wide variety of cell geometries. In theory, the simulation volume is therefore infinite and so bulk properties can be determined from a relatively small simulation.

An important consideration regards the behaviour of sites which leave the cell; to conserve mass and energy, the site or sites leaving the cell are reintroduced in a controlled manner. For example, consider a square simulation cell in two dimensions; as

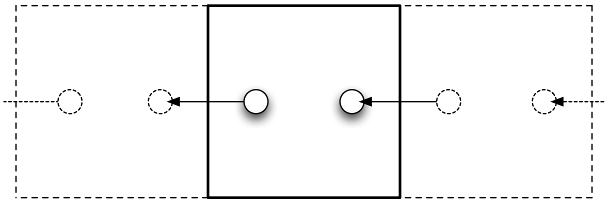

Figure 6.5: Periodic images of a two dimensional simulation cell. Only nearest neighbour cells on the lateral axis are depicted (dashed lines), with the actual simulation cell central and delineated with a solid line. Also shown is the treatment of the movement of sites into and out of the simulation cell

sites leave the central simulation cell, they are reintroduced via the neighbouring cells using the periodic boundary conditions as shown in Fig. 6.5. Also of importance is the treatment of the bonded and nonbonded interactions between sites; if a naïve site-to-site separation vector is used, the periodic boundaries will cause problems as sites leave the cell and are reintroduced elsewhere. To alleviate this issue, the use of the *minimum image convention* is commonplace; wherever the separation between bound or interacting sites i and j is larger than half of the simulation cell dimension on any axis, it is assumed that the interaction is actually effected on the site in the appropriate neighbouring cell as opposed to the site in the central simulation cell; the appropriate separation vector can be calculated as follows [45]:

$$\mathbf{r}_{ij}(a) = \mathbf{r}_{ij}(a) - \mathbf{cell}(a) \cdot \left[\frac{\mathbf{r}_{ij}(a)}{\mathbf{cell}(a)} \right], a \in \{x, y, z\} \tag{6.16}$$

here, $\mathbf{r}_{ij}$ is the separation vector, **cell** is the simulation cell dimension vector and the square brackets denote the standard rounding function. This is illustrated in Fig. 6.6, and leads to the condition that the nonbonded interaction cutoff must be less than half of the smallest dimension of the simulation cell. This also has the effect of preventing the interaction of a site with itself.

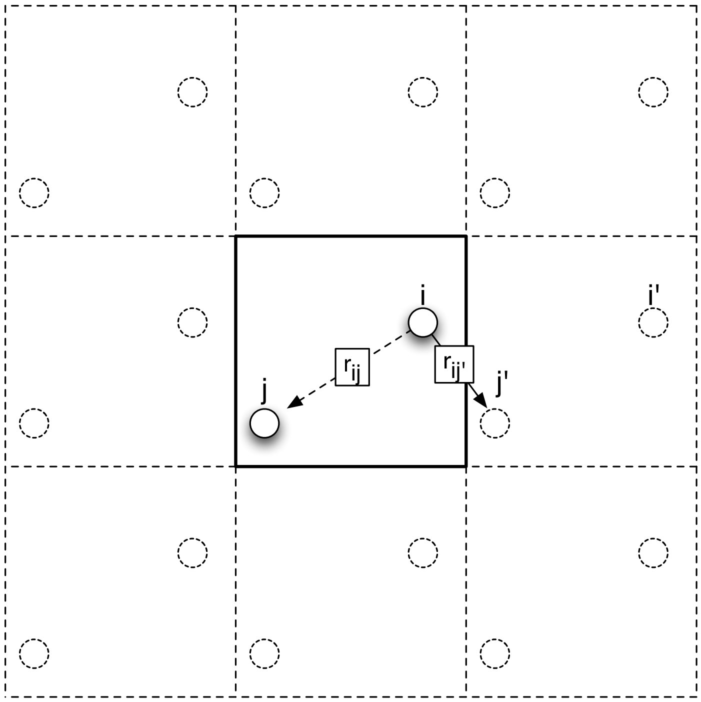

Figure 6.6: Periodic images of a two dimensional simulation cell. Only nearest neighbour cells are depicted (dashed lines), with the actual simulation cell central and delineated with a solid outline. Also shown is the minimum image convention separation between bound sites i and j, $r_{ij'}$ (solid line), and the non-minimum image convention separation r_{ij} (dotted line).

6.4.2 Treatment of the electrostatic potential

The electrostatic interaction via Coulomb's potential (Eqn. (6.5)) decays as $1/r_{ij}$, making it effective over relatively long ranges in terms of the molecular dynamics systems typically studied. Although early studies used a truncated cutoff range, r_c, for electrostatic interactions, this is not recommended due to the relatively abrupt changes in potential around the cutoff length for small r_c.

The basic concept of the Ewald sum [48] is to split the electrostatic potential into two contributions; a short ranged potential, which can be evaluated in a conventional manner, and a long ranged contribution which requires more elaborate treatment.

Consider the point charges present in a typical molecular simulation; with the addition of a screening potential of opposite sign, the influence of the point charges decays far more rapidly with distance. This is the first component of the Ewald sum, a set of (typically Gaussian) charge distributions of equal magnitude and opposite sign to the point charges in the system which renders the effects of the point charges short ranged (See Fig. 6.7).

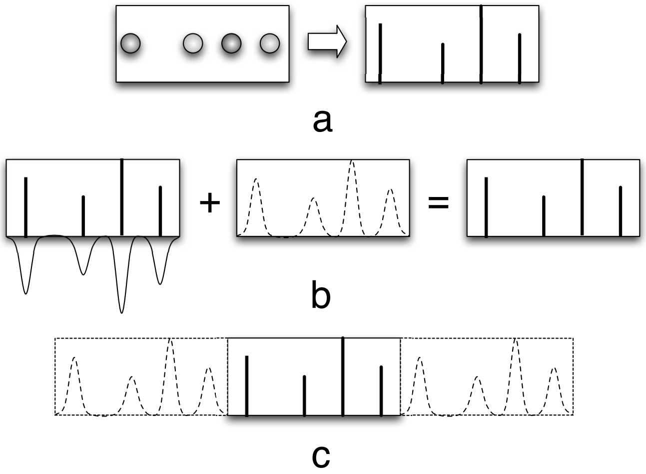

Figure 6.7: Illustration of the Gaussian charge contributions to the Ewald sum. **a**; representation of the interacting sites as point charges, **b**; addition of point charges, screening charge distributions and compensatory charge distributions recovers the original point charges, **c**; the reciprocal space contributions to the Ewald sum as shown in neighbouring periodic cells

The second component is a compensation for the newly introduced screening distributions; this compensation consists of a set of charge distributions of the same form and magnitude as the screening charge distributions, but of opposite sign. Due to the additive nature of the electrostatic potential, the sum of the point screening and compensatory charge distributions is zero (see Fig. 6.7). Importantly, the compensating charge distributions may be expressed as a Fourier series - and it is this transformation that allows a long ranged, periodic treatment of the charges in the system in manner analogous to the repeating set of simulation cells under periodic boundary conditions.

There are two final additions to the Ewald sum; the first recognises the point charges interacting with themselves in the form of the reciprocal space compensatory charge distributions. As these distributions are centred on the positions of the point charges themselves, this term is constant in simulation; if and when the point charges move, reciprocal space charge distributions remain centred on them - and hence the self-interaction term will be invariant. The final addition to the Ewald sum governs the dielectric effects of the medium surrounding the periodic cells. The full Ewald summation may therefore be expressed as

$$\begin{aligned} V_{\mathsf{Ewald}} = \frac{1}{2}\sum_{i=1}^{N}\sum_{j=1}^{N} & \left(\sum_{|\mathbf{n}|=0}^{\infty\prime} q_i q_j \frac{\operatorname{erfc}(K|\mathbf{r}_{ij}+\mathbf{n}|)}{|\mathbf{r}_{ij}+\mathbf{n}|} \right. \\ & \left. + \frac{1}{\pi L^3} \sum_{\mathbf{k}\neq\mathbf{0}} q_i q_j \frac{4\pi^2}{k^2} \exp\left(\frac{-k^2}{4K^2}\right) \cos\left(\mathbf{k}\cdot\mathbf{r}_{ij}\right) \right) \\ & - \frac{K}{\pi^{1/2}} \sum_{i=1}^{N} q_i^2 \\ & + \frac{2\pi}{3L^2} \left| \sum_{i=1}^{N} q_i \mathbf{r}_i \right|^2 \end{aligned} \tag{6.17}$$

where a prime denotes we omit $i = j$ for $|\mathbf{n}| = 0$, ie. the central simulation cell. The repetition of the central simulation cell on an infinite, regular lattice is represented by the cell offset **n** and K is an arbitrary parameter which controls the width of the Gaussian charge distributions; where K is sufficiently large, the only term which contributes to the real space part of the Ewald sum (the first term in Eqn. (6.17)) is that where $n = 0$, which is equivalent to the ordinary minimum image convention. The second term in Eqn. (6.17) controls the reciprocal space contribution; where K is large, the Gaussian charge distributions are rather sharp and require a relatively large number of k vectors to accurately reproduce. The final two terms represent the contributions from the correction to self interaction in reciprocal space, and the nature of the dielectric medium surrounding the simulated system. The prefactor of $1/4\pi\epsilon_0$ has been omitted from the terms for brevity.

6.4.3 Thermostat

Throughout this thesis, the simulations are performed in the *canonical ensemble*; that is, with constant number of interacting sites (as ensured by the periodic boundary condition), constant simulated volume (as the simulation cell dimensions do not change) and constant temperature - also referred to as the *NVT* ensemble. Although a simulation is typically initialised by assigning kinetic energies from the Maxwell-Boltzmann distribution for the appropriate temperature, it will rarely remain in this state for any significant length of time. It may be that an energetically unfavourable initial configuration of the sites will cause excess potential energy to be converted into kinetic energy, thus "heating up" the system. Therefore, it is essential to monitor and adjust the simulation to ensure the desired temperature setting is observed.

Arguably the simplest thermostat available is basic temperature rescaling; after a specified number of MD steps, the average kinetic energy of the system is determined from the velocities of the component sites:

$$\frac{n}{2}Nk_BT = \frac{1}{2}\sum_i m_i v_i^2 \tag{6.18}$$

where n is the number of degrees of freedom for the velocity (generally three), N the number of sites in the system, with m_i being the mass of site i and v_i its velocity. A systematic rescaling of all the velocities is then applied to ensure agreement between the instantaneous kinetic temperature and the desired temperature. A more sophisticated velocity rescaling scheme was suggested by Berendsen *et al* [49], using a scaling parameter λ to yield a softer coupling to the target temperature T_0 via the time parameter

τ:

$$\lambda = \left[1 + \frac{\delta t}{\tau}\left(\frac{T}{T_0} - 1\right)\right]^{1/2} \tag{6.19}$$

Unfortunately, this variety of thermostat does not recreate the desired canonical distribution of energies, although the deviations from this target may be small. To ensure sampling from the canonical ensemble is observed, a different method of controlling the temperature will be used.

An alternative to velocity rescaling was proposed by Andersen [50], who coupled the simulated system to an external heat bath via random "collisions" of the particles; whenever a collision occurs, the particle receives a new velocity drawn from the Maxwell-Boltzmann distribution for the specified temperature. This can also be considered as a Monte-Carlo move which introduces or removes energy from the system, but in the intervening MD steps the assumption is that the system evolves on a constant energy surface; thus, the collisions allow the sampling of these energy shells with the appropriate Boltzmann weighting [51], and ensure a canonical distribution of energy is experienced. The strength of the coupling to the heat bath is determined by the frequency of these stochastic collisions, but this should not be set without consideration - if the collisions are too frequent, the natural kinetic fluctuations in the system will be overshadowed by the thermostat effects. If the collisions are too rare, there will be slow sampling across energy shells with a resultant degradation of sampling efficiency [45].

A still different method to control temperature in MD simulations was proposed by Nosé [52], and reformulated by Hoover [53]. The Nosé-Hoover thermostat removes the stochastic element of Andersen's heat bath, and reduces it to a single degree of freedom which is included in the extended Hamiltonian of the system. The resultant system has equations of motion which differ from the standard expressions;

$$\ddot{\mathbf{r}}_i = \frac{\mathbf{F}_i}{m_i} - \gamma \mathbf{r}_i \tag{6.20a}$$

$$\dot{\gamma} = -\frac{1}{\tau}\left(\frac{g}{N_{df}}\frac{T_0}{T(t)} - 1\right) \quad , \tag{6.20b}$$

using an effective relaxation time τ:

$$\tau^2 = \frac{Q}{N_{df} k_B T_0} \tag{6.21a}$$

and N_{df} the degrees of freedom in the system, Q acting as the fictional "mass" of the heat bath - larger values of Q produce loose thermal coupling between the modelled system and the heat bath, and hence greater deviation may result from T_0, the desired temperature. The parameter g is linked to the degrees of freedom in the system; for sampling in real-time, $g = N_{df}$, with $g = N_{df} + 1$ for sampling in the scaled time introduced through the extended system.

6.5 Calculation of average properties

For the canonical ensemble (where the number of sites, volume and temperature are held constant), the ensemble average value of an observable A is defined as [51]

$$\langle A \rangle_{\mathsf{NVT}} = \frac{\int d\Gamma \ A(\Gamma) e^{-\beta \mathcal{H}(\Gamma)}}{\int d\Gamma \ e^{-\beta \mathcal{H}(\Gamma)}} \qquad = \frac{\int d\Gamma \ A(\Gamma) e^{-\beta \mathcal{H}(\Gamma)}}{Q} \tag{6.22}$$

where Γ is shorthand for the state vector encompassing the positions and momenta of the system, $\mathcal{H}(\Gamma)$ denotes the Hamiltonian of the system in state Γ and $\beta = 1/k_B T$ with k_B as Boltzmann's constant. Eqn. (6.22) may be interpreted as the sum over all states for the product of $A(\Gamma)$ and a weight function proportional to the probability of state Γ occurring; in the canonical ensemble this weight function is $e^{-\beta \mathcal{H}(\Gamma)}$, and these weights are normalised by the denominator of Eqn. (6.22) - which is Q, the canonical partition function.

The integrals in Eqn. (6.22) may present problems for direct calculation methods, as the enumeration over all conceivable arrangements of positions and momenta is not feasible for anything other than the most trivial systems. This does not, however, present an insurmountable barrier to evaluating an ensemble average; due to the form of the weight function, the large regions of phase space with relatively high energy will produce exponentially small contributions to $\langle A \rangle$. Thus, it is necessary only to visit "representative" regions of the total phase space (specifically, those regions with relatively low energy) to produce an increasingly accurate estimate of the true ensemble average. In a molecular dynamics simulation the assumption is made that the time average of the observable property, $\bar{A}$, will naturally converge onto $\langle A \rangle$ given a sufficiently long time [51], and hence that the correct equations of motion for a system naturally lead to representative sampling of phase space.

A special case of the ensemble average in Eqn. (6.22) involves the use of Dirac's delta function as the observable, to ensure the summation over only specific states - and in doing so, evaluate the probability of those states occurring. Dirac's delta function may be defined as

$$\int d\Gamma' \; \delta(\Gamma - \Gamma') f(\Gamma') = f(\Gamma) \tag{6.23}$$

leading to the ensemble average

$$\langle \delta(\Gamma - \Gamma') \rangle_{\mathsf{NVT}} = \frac{\int d\Gamma' \; \delta(\Gamma - \Gamma') e^{-\beta \mathcal{H}(\Gamma')}}{Q} \qquad = P(\Gamma) \quad . \tag{6.24}$$

The use of such a delta function in Eqn. (6.24) allows the effective exclusion of all states of the system where $\Gamma' \neq \Gamma$, naturally producing the probability of state Γ, $P(\Gamma)$, given the nature of the weight function used.

Calculation of excess free energy

The Helmholtz free energy, A, defined as

$$\begin{aligned} A &= -k_BT\ln(Q) \\ &= -k_BT\ln\left(\int d\Gamma'\ e^{-\beta\mathcal{H}(\Gamma')}\right) \end{aligned} \tag{6.25}$$

allows a simple definition of the free energy difference between two systems:

$$\begin{aligned} \Delta A &= A_1 - A_2 \\ &= -k_BT\ln\left(\frac{Q_1}{Q_2}\right) \\ &= -k_BT\ln\left(\frac{\int d\Gamma_1'\ e^{-\beta\mathcal{H}_1(\Gamma_1')}}{\int d\Gamma_2'\ e^{-\beta\mathcal{H}_2(\Gamma_2')}}\right) \quad . \end{aligned} \tag{6.26}$$

Using the delta function of Eqn. (6.24), we may calculate the excess Helmholtz free energy of a specific state with respect to the system at large, which may also be expressed as a function of the probability of that state:

$$\Delta A(\Gamma) = -k_BT\ln\left(\frac{\int d\Gamma'\ \delta(\Gamma-\Gamma')e^{-\beta\mathcal{H}(\Gamma')}}{\int d\Gamma'\ e^{-\beta\mathcal{H}(\Gamma')}}\right) \qquad = -k_BT\ln(P(\Gamma)) \tag{6.27}$$

If information pertaining to regions of phase space with relatively high energy is required, the nature of the canonical weighting function acts to prevent efficient sampling for the system. This may be overcome by extending the Hamiltonian of the system to include a biasing potential, which alters the energy in defined regions of phase space to improve the sampling process. Consider the excess free energy expression of Eqn. (6.26);

$$\Delta A = -k_BT\ln\left(\frac{\int d\Gamma'\ \delta(\Gamma-\Gamma')e^{-\beta\mathcal{H}(\Gamma')}}{\int d\Gamma'\ e^{-\beta\mathcal{H}(\Gamma')}}\right) \tag{6.28a}$$

$$= -k_BT\ln\left(\frac{\int d\Gamma'\ \delta(\Gamma-\Gamma')e^{-\beta[\mathcal{H}(\Gamma')+V(\Gamma)-V(\Gamma)]}}{\int d\Gamma'\ e^{-\beta\mathcal{H}(\Gamma')}}\right) \tag{6.28b}$$

$$= -k_BT\ln\left(\frac{\int d\Gamma'\ \delta(\Gamma-\Gamma')e^{\beta V(\Gamma)}e^{-\beta[\mathcal{H}(\Gamma')+V(\Gamma)]}}{\int d\Gamma'\ e^{-\beta\mathcal{H}(\Gamma')}}\right) \tag{6.28c}$$

the right hand sides of Eqns. (6.28a)-(6.28c) are mathematically equivalent, but the introduction (and subsequent removal) of the biasing potential $V(\Gamma)$ allows enhanced, targeted sampling in otherwise neglected regions of phase space. In the example of Eqn. (6.28c), Γ is used to denote a fully-specified microstate, but this may be substituted with one or more coordinates or a collection of microstates to suit. Combining and rearranging Eqns. (6.27) and (6.28c) gives the expression

$$\Delta A(\Gamma) = -k_B T \ln(P(\Gamma)_{\mathsf{bias}}) - V(\Gamma) + C \quad , \tag{6.29}$$

where C is an undetermined constant, and $P(\Gamma)_{\mathsf{bias}}$ denotes a probability calculated in the biased ensemble. By constructing a histogram describing the probability distribution for Γ during simulation, it becomes a simple exercise to reconstruct the relative excess free energies provided the biasing potential has a simple analytical form, amenable to removal via Eqn. (6.29). Although these biasing potentials must be chosen *a priori* in such a study, and hence there may be a certain amount of trial and error involved, one suitable basis may be a potential which is harmonic about some Γ in the region of interest.

6.5.1 Umbrella sampling and the Weighted Histogram Analysis Method (WHAM)

The use of Eqn. (6.29) relies on relatively small differences between the biased and unbiased systems. Where the difference is large, or the region of phase space to sample is extended such that a single biasing potential alone will not ensure adequate sampling, a series of separate simulations with differing biasing potentials may be constructed after the umbrella sampling method of Torrie and Valleau [54]. The biasing potentials should be chosen such that a significant overlap in the probability distributions of the separate simulations exists; this allows the individual free energy differences from the differing simulations to be related to one another and combined into a unified description of the region of interest. As the individual excess free energy distributions differ by some constant offset (which will vary between the separate simulations), there remains the problem of determining the C values in Eqn. (6.29) which best align the data (the general process is illustrated in Fig. 6.8).

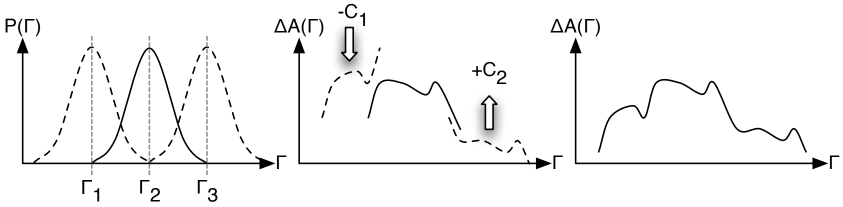

Figure 6.8: Illustration of the umbrella sampling technique. Left to right: overlapping probability histograms from independent simulations with harmonic biasing potentials; excess free energy fragments determined from Eqn. (6.29) and the process of alignment to create a unified description of excess free energy across all the simulations.

Although it can be possible to determine these offsets by eye, dependent on the quality of data from the simulations, the weighted histogram analysis method (WHAM) of Kumar et al [55] allows an automated determination of the individual C values via the iteration to self consistency of the following equations:

$$P(\Gamma) = \frac{\sum_i n_i(\Gamma)}{\sum_i N_i \exp\left(\beta(C_i - V_i(\Gamma))\right)} \tag{6.30}$$

$$C_i = -k_B T \ln\left(\sum_\Gamma P(\Gamma)\exp\left(-\beta V_i(\Gamma)\right)\right) \quad . \tag{6.31}$$

where C_i is the offset for simulation i, $n_i(\Gamma)$ is the number of samples in the histogram bin for Γ in simulation i, N_i is the total number of samples for simulation i, and $V_i(\Gamma)$ is the biasing potential value for Γ in simulation i. The WHAM technique has the benefits of allowing multiple overlapping distributions in any region of Γ, producing a statistically optimum free energy estimate, and automatically generating an error estimate which allows straightforward targeting of further simulations in order to improve the available data [55].

Chapter 7

Oxygen permeation in phospholipid monolayers

In this chapter, experimental electrochemistry with ultramicroelectrodes (UMEs) is used to investigate oxygen permeation at an air/water interface in the presence of phospholipid monolayers (DMPC and DSPC) under varying levels of compression. This experimental data is parmeterised with FEM simulations. The DSPC monolayer then serves as a model to determine the theoretical free energy barrier presented to the permeation of oxygen via molecular dynamics simulations with the "umbrella sampling" technique of Torrie and Valleau [54].

7.1 Introduction

The transport of gases and other molecules across membranes is of great biological importance, and has been the subject of extensive study in both model systems and living cells [56]. For example, in the human body the lungs act as a mechanism of transfer to allow atmospheric oxygen to enter the bloodstream and to enable the conjugate expulsion of carbon dioxide. The relative permeability of gases through naturally occurring barriers can therefore yield important information regarding the efficiency of gas transport mechanisms in a number of biologically relevant systems.

The use of monolayer systems is well established for the purposes of pharmacological research [57, 58], evaporation control [59], selective gas permeation [60, 61] and protein studies [62, 63]. The high reproducibility and precise control over aspects such as the surface pressure and area per lipid (APL) of monolayers formed in a "Langmuir trough" are of obvious attraction to the experimental scientist, and the diffusion of oxygen across monolayers of various compositions has previously been studied from the basis of experimental electrochemistry [2, 64, 65] using the scanning electrochemical microscopy (SECM) method 3.5. Phospholipids composed of a hydrophilic "head" group and one or more hydrophobic "tails" (Fig. 7.1) form the major structural component of biological membranes, and as such present an obvious model system for the experimental study of gas permeation in natural membranes. Experimental electrochemistry and molecular dynamics, when applied in tandem to an experimental system, allow the investigation of gas permeation on both the macroscopic and microscopic scales, and a more complete picture of gaseous transport becomes available.

7.2 Experimental materials and methods

7.2.1 Reagents

The aqueous subphase was a home made phosphate buffer of pH 7.2, comparable to biological pH, in Milli-Q reagent water (Millipore Corp.). DSPC, DPPC and DLPC spreading solutions (Avanti Polar Lipids, all >99%) were made to concentration 1 mg ml^{-1} in chloroform (HLPC grade, Fisher Scientific, UK) to allow easy distribution of

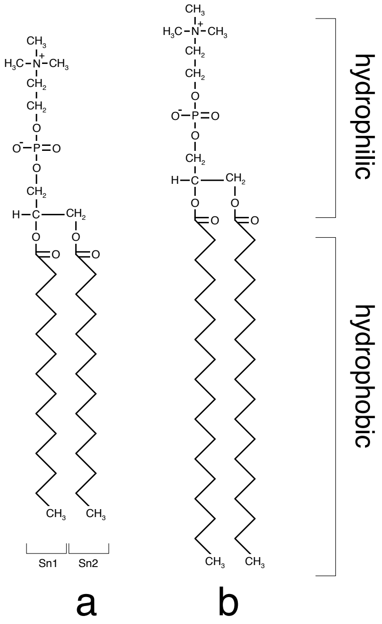

Figure 7.1: Structure of the phospholipids DMPC (a) and DSPC (b). Both surfactants feature an identical phosphatidylcholine head group, with 14 and 18 carbon groups in the acyl "tails" of DMPC and DSPC respectively.

the lipids across the surface of the water before the evaporation of the chloroform and subsequent formation of a monolayer.

7.2.2 Apparatus and methods

The PTFE Langmuir trough (Model 611, Nima Technology, Coventry, UK) was equipped with two PTFE paddles and surface pressure sensor allowed controlled compression of monolayers at the aqueous / atmospheric interface (Fig. 7.2). A 25 μm diameter Pt disk working submarine UME with RG value ≈ 10 (ratio of glass insulator radius to electrode radius) was mounted perpendicular to the interface as shown in 7.2; although the electrode support penetrates the monolayer, this takes place several cm away from the electrode tip and hence the effects of disturbing the monolayer in this manner is

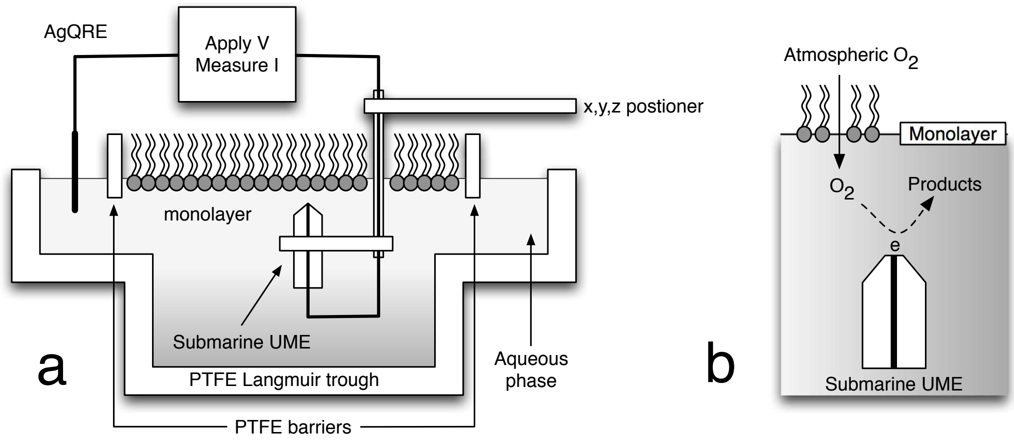

Figure 7.2: **a**: Schematic of experimental apparatus. A Langmuir trough allows the controlled formation of lipid monolayers at the air/water interface, while a submarine UME induces the reduction of the oxygen permeating into the aqueous phase. **b**: Detail of the transfer of oxygen through the monolayer, where it is reduced at the exposed Pt wire in the centre of the electrode tip. This reduction generates a measurable current, and hence the determination of rate constants for the permeation.

expected to be very localised, leaving the measurements unaffected. The Pt UME was positioned with a combination of x, y, z stages (M-462, Newport Corp., CA) and piezoelectric positioner and controller (P843.30 and E662, Physik Instrumente, Waldbronn, Germany) were used for coarse and fine positioning respectively. A triangular wave/pulse generator (Colburn Electronics, Coventry, U.K.) controlled the potential of the Pt working electrode, with current measured using a home-built current follower. All potentials were recorded with respect to the quasi-reference electrode formed by a piece of silver wire (AgQRE, 7.2) in a two-electrode arrangement. A Lab PC-1200 card (National Instruments, Austin, TX) was used for data recording, with surface tension measurements provided by a Wilhelmy paper plate and electrobalance (model PS4, Nima Technology, Coventry, UK) The surface of the aqueous subphase was cleaned by aspiration before an SECM approach curve for the reduction of oxygen was measured to the clean interface by holding the UME at a potential which ensured the diffusion limited reduction of oxygen and the gradual movement of the UME tip to the interface (circa 1 μm s^{-1}). This potential was determined to be between -0.6 and -0.65 V, and before any electrochemical measurements were taken the UME potential was pulsed for 1 s at 1 V, followed by 15 s at -0.6 V. All readings were taken at room temperature (298 $\pm$ 2K) in an air conditioned room, and were normalised by the steady-state bulk current for oxygen reduction (I_∞). The monolayers were formed by adding 50 μL of the spreading solution of lipid to the surface of the aqueous subphase via syringe, with 15 mins then allowed for solvent evaporation. The surface pressure of the monolayers was taken to be the difference between the surface tension of the clean aqueous/atmospheric interface and the measured surface tension in the presence of the monolayer. Isotherms were produced at a compression rate of 10 cm^2 min^{-1} from a surface area of 180 cm^2, before a fresh monolayer was produced and the surface pressure held at increments of 5 mN min^{-1} while the reduction approach curves were measured until the final collapse point of the monolayers were reached.

7.3 FEM simulation details

The transport of gaseous oxygen across an air/water interface can be described as follows:

$$O_2(\text{aq}) \underset{k_{aw}}{\overset{k_{wa}}{\rightleftharpoons}} O_2(\text{air}) \quad , \tag{7.1}$$

where k_{wa} and k_{wa} are the first-order rate constants for oxygen transfer at the interface. The flux of gaseous oxygen may therefore be simply expressed:

$$j_{O_2} = k_{aw} c_a - k_{wa} c_{w,i} \quad , \tag{7.2}$$

where c_a and $c_{w,i}$ are the concentrations of oxygen in the gaseous phase and aqueous phase adjacent to the interface, with k_{aw} and k_{wa} being the rate constants for oxygen transfer from air to water, and water to air respectively. The concentration of oxygen in the gaseous phase adjacent to the monolayer remains constant during experiment, due to the relatively fast mass transport, and so the air to water transfer may be replaced with a constant:

$$k' = k_{aw} c_a \quad . \tag{7.3}$$

At equilibrium the oxygen flux is zero, hence:

$$k' = k_{wa} c_* \quad , \tag{7.4}$$

where c_* denotes the concentration of oxygen in bulk solution. Therefore, the steady state oxygen flux through the monolayer may be described by:

$$\begin{aligned} j_{O_2} &= k'(1 - C) \\ C &= \frac{c_{w,i}}{c_*} \quad . \end{aligned} \tag{7.5}$$

Eqn. (7.5) is functionally identical to the expression for flux outlined in earlier SECM studies of dissolution [26]. The experimental rate constants are determined via the fitting of k' in an axisymmetrical finite element model (Fig. 7.3) to the recorded data, with the diffusion equation in cylindrical coordinates:

$$D\left(\frac{\partial^2 c}{\partial r^2} + \frac{1}{r}\frac{\partial c}{\partial r} + \frac{\partial^2 c}{\partial z^2}\right) = 0 \quad . \tag{7.6}$$

Bulk and Pt electrode boundary conditions (Fig. 7.3) were normalised to $C = 1$ and $C = 0$ respectively, with the flux at the monolayer described as Eqn. (7.5) and all length scales expressed in terms of the radius of the Pt electrode, as described previously [2, 26, 64, 65].

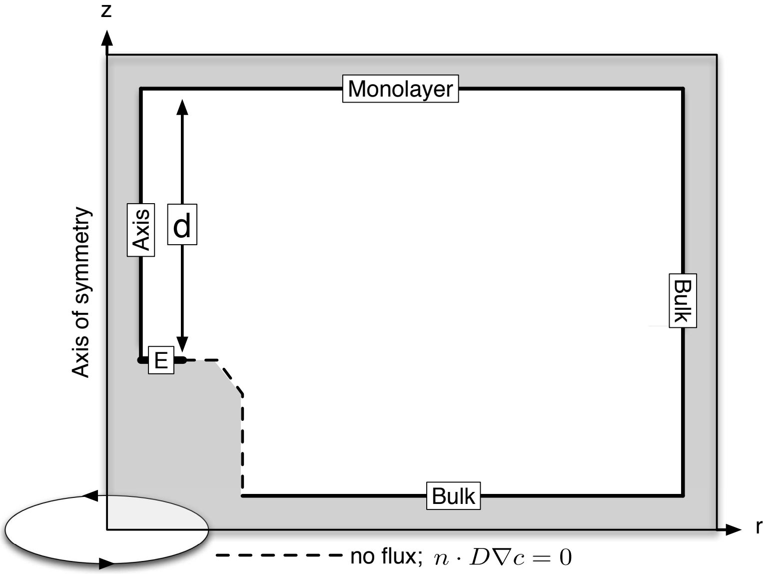

Figure 7.3: Axisymmetric FEM geometry used to determination experimental values for the k', the first order rate constant for oxygen transfer across the a monolayer, which is the only adjustable parameter in the model. The simulated distance between the electrode and the interface, d, is progressively reduced to model the approach of the submarine UME to the experimental Langmuir monolayer.

σ, $\mathring{A}$	ϵ/k_B, K	L, $\mathring{A}$	Q, Debye Ångstrom
3.1062	42.183	0.9699	-0.8081

Table 7.1: Oxygen molecule parameters for the MD simulation of permeation in DSPC monolayers, after Vrabec [67] and Galbraith [68]. Listed are the Lennard-Jones radius and well depth : σ and ϵ, the LJ site separation L and quadrupole moment Q.

7.4 MD simulation details

The DSPC monolayer was represented with the Charmm27 force field [66] as an all-atom structure with explicit hydrogens based on the topology of the Charmm27 DMPC molecule with the addition of four hydrocarbon groups. The solvent model was TIP3P water from the same source. All hydrogen atoms were constrained with the SHAKE algorithm [46] to a tolerance of $10^{-8}\mathring{A}$. The oxygen molecule consisted of four point charges to create a quadrupole moment, with van der Waals interactions modelled as two Lennard-Jones 12-6 potentials centred on the oxygen atoms [67, 68], see Table 7.1. Care was taken to ensure the point charges lie inside the steeply repulsive region of the LJ potential in the molecule interior, and the final structure was modelled as a rigid body to preserve linearity.

A single DSPC lipid was simulated for 10 ps in vacuum to relax the structure, and the resulting model lipid was used to form two monolayers of 36 lipids each by applying a random rotation around the major axis of the molecule, followed by a random offset of $\pm\ 5\mathring{A}$ along the same axis to break symmetry and minimise order. These initial monolayers, of area per lipid (APL) 60 $\mathring{A}^2$, were arranged around a TIP3P water box as in Fig. 7.4, with the ratio of water molecules to lipids circa 31:1 providing full solvation of the constituent lipid head groups [69]. At least 30 $\mathring{A}$ vacuum was placed beyond the terminal methyl groups of the lipids to model the atmospheric phase. No gaseous species were present; for this volume only circa 1 nitrogen and $<$ 1 oxygen would be present. The resultant system was allowed to relax over a 2 ns simulation. Monolayers of APL 57.5 $\AA^2$ and 55 $\AA^2$ were formed from the equilibrated APL 60 $\AA^2$ system by changing the simulation cell size and a further 1 ns of simulation time to relax the new systems. Integration timestep of 2 fs and a nonbonded interaction cutoff of 12 $\AA$ were used throughout, with Cartesian coordinate origin at the centre of mass of the system.

The umbrella sampling technique was used in conjunction with the DLPOLY [70] molecular dynamics package, modified to support a harmonic constraint between the centres of mass of the oxygen permeant molecule and the remaining system, with the constraint acting only along the reaction coordinate, defined as the z axis (perpendicular to the monolayer interfaces), to allow unconstrained rotation of the molecule and free diffusion on the x, y plane.

$$U = \frac{K}{2}(z_{\text{ox}} - z_{\text{rest}})^2 \tag{7.7}$$

where K is the harmonic bond strength, and z_{ox} and z_{ox} are the z coordinates of the centre of mass of the oxygen molecule, and the resting bond length relative to the centre of mass of the rest of the system.

Two oxygen molecules per simulation were inserted at symmetrical z (Fig. 7.4), with the initial positions on the x, y plane determined to be regions of low energy, except where the separation between oxygen molecules could lie in the nonbonded potential cutoff radius (12 $\AA$); in such cases ($-6.0\AA \leq z \leq 6.0\AA$), a single oxygen molecule was inserted to prevent direct interactions between the two oxygen molecules. After initial insertion, 20 ps simulation time was allowed to relax each system before 100 ps of simulation time was used for data collection. All simulations were performed in the NVT ensemble, using the Hoover thermostat [53] with relaxation constant 0.5 ps.

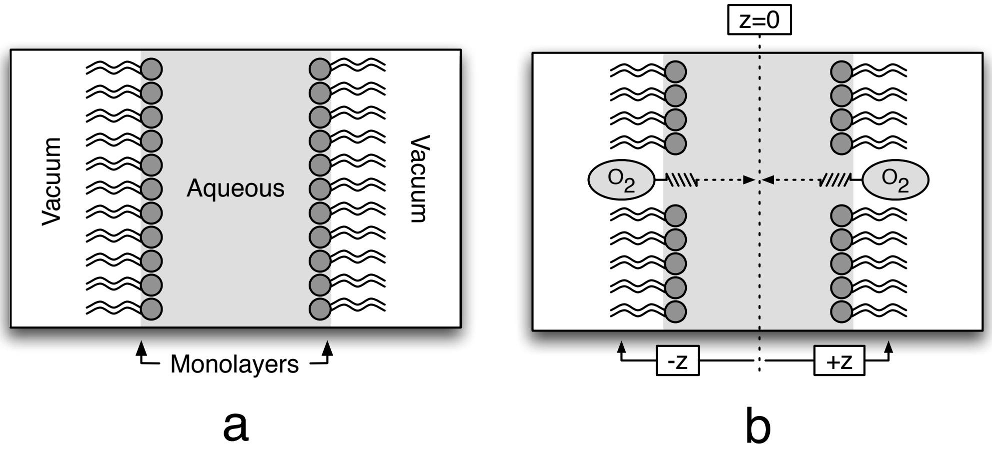

Figure 7.4: *a*: Schematic of symmetrical DSPC monolayers around a TIP3P water box as used in the simulations. *b*: Illustration of symmetrical insertion and harmonic restraining potentials for oxygen permeant molecules at reaction coordinate z. Restraints act on the centres of mass of the oxygen molecules and the remainder of the system, with the minimum energy of the restraint at centre of mass separation $z = z_0$

Initial MD test simulations were performed in the aqueous, interfacial and bulk acyl regions of the most condensed system (APL 55 $\AA^2$) to determine the appropriate harmonic bond strength (K) and spacing along the reaction coordinate (defined as the axis normal to the monolayer, z, with spacing δz) for the restraining potentials, and to examine the sensitivity of the results to the initial insertion coordinate on the x, y plane. Values of $K =$ 25kJ mol^{-1} and $\delta z = 1\AA$ appeared sufficient to ensure good overlap in the probability distributions, producing similar profiles for the aqueous and acyl regions for different x, y insertion coordinates, but were proven problematic in the vicinity of the interfacial region where poor agreement of the free energy profiles occurred. The relative error of the probability distributions [55] was therefore used to determine regions which would benefit from more detailed sampling, where $K =$ 50kJ mol^{-1} and $\delta z =$ 0.5 $\AA$ were used. The final free energy profiles were generated from the individual simulation results using Eqn. (6.31) to a tolerance of 4.184 J mol^{-1} [71].

7.5 Results

The approach curves for the DMPC and DSPC monolayers under varying levels of compression (Figs. 7.5 and Figs. 7.6) both display similar general features; the induced current remains low and relatively invariant for distances greater than $\approx 25\mu$m from the air/water interface, before a noticeable increase at distances closer than $\approx 10\mu$m. By a distance of ≈ 5 μm from the interface, the induced current is increasing rapidly, before an eventual plateau or discontinuity at a distance of several μm from the interface. The results show a diminution of the induced current as the imposed surface pressure of the monolayer increases, illustrating the increasing barrier to oxygen permeation as the monolayer is compressed.

The increasing current induced in the UME upon approaching the air/water interface demonstrates the increasing concentration of oxygen in the interfacial aqueous phase; at large distances, the concentration gradient of dissolved gaseous oxygen is small, as the system is relatively homogeneous in that respect - this is reflected in the relatively small and slowly increasing current. Upon approaching the interface, the current increases to reflect the greater concentration of oxygen in the locality of the interface. The behaviour of the induced current at very low distances of the UME tip from the interface ($< 2\mu$m) can be explained by the local deformation processes of the UME tip distending the monolayer surface [2].

The FEM rate constants demonstrating the best fit to selected experimental data are shown in Figs. 7.5 and 7.6, with a summary in Table 7.2. For each experimental system, the introduction of lipids to the air/water interface immediately reduces the permeation rate of oxygen as the accessible surface area for oxygen permeation is

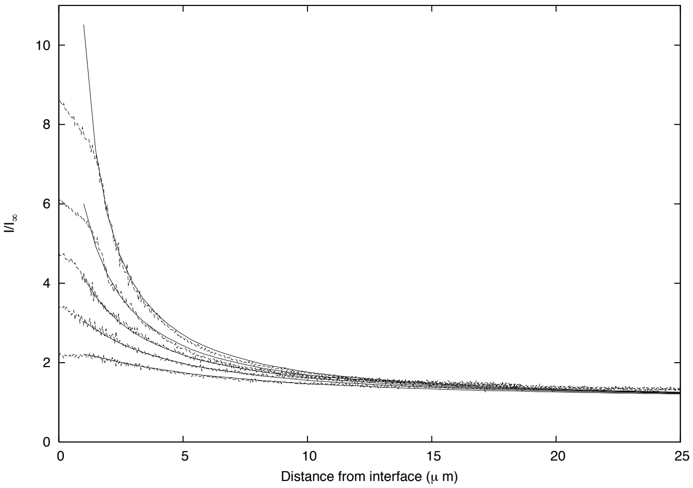

Figure 7.5: Selected normalized steady-state diffusion limited current vs. UME-interface separation for the reduction of oxygen at a DMPC monolayer. From top to bottom, the dashed curves correspond to the experimental approach to a clean interface and surface pressures of 0, 10, 20 and 35 mN m^{-1}. The solid lines represent a clean theoretical approach (no lipid barrier present), and $k'/10^{-8}$ = 6.76, 3.16, 1.9, and 1.18. The experimental results are readily reproducible to distances of circa 2 μm, at which point experimental deformation processes of the monolayer may vary dependent on the precise geometry of the UME tip.

reduced, even in the liquid expanded phase of the monolayer.

For both DMPC and DSPC there is a pronounced reduction in the permeation rate as the monolayer is compressed, in agreement with previous studies involving monolayers of various compositions [2, 64, 65]. This reduction is not the same for the two lipids, however. The Brewster angle microscopy (BAM) studies of Kubo *et al* [72] and Arnold *et al* [73] reveal the monolayer structures of both DMPC and DSPC to be heterogeneous at low pressures; neither lipid produces a uniform coverage of the interface, instead phase separating spontaneously into irregular domains on a scale of tens to hundreds of μ m which merge into a single phase under compression.

The BAM results for the DMPC monolayers display certain differences; Arnold *et al* show an effectively uniform structure for pressures of 5mN m^{-1} and up, with the Kubo

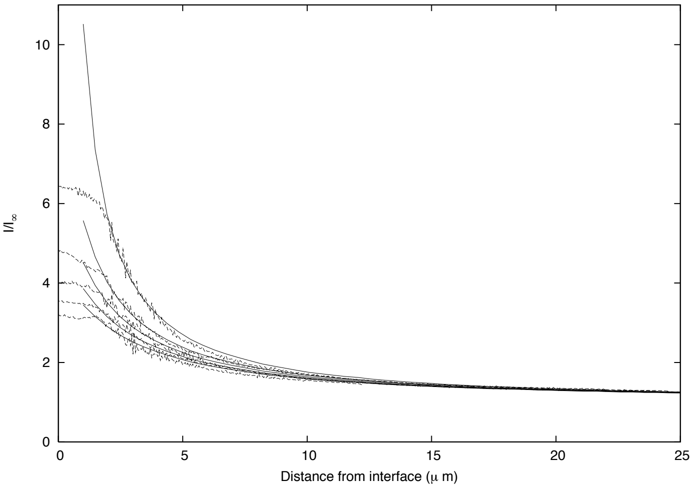

Figure 7.6: Selected normalized steady-state diffusion limited current vs. UME-interface separation for the reduction of oxygen at a DSPC monolayer. From top to bottom, the dashed curves correspond to the experimental approach to a clean interface and surface pressures of 0, 10, 20 and 35 mN m^{-1}. The solid lines represent a clean theoretical approach, and $k'/10^{-8} =$ 5.68, 3.7, 2.8, and 2.32.

	$k'/10^{-8}$ cm s^{-1}	
Π (mN m^{-1})	DMPC	DSPC
0	6.76	5.68
10	3.16	3.7
20	1.9	2.8
35	1.18	2.32

Table 7.2: First order rate constants for the transfer of oxygen across two phospholipid monolayers, as determined from finite element models as described in the text

study clearly illustrating solid domains in a liquid phase even up to 20 mN m^{-1}. Above this pressure, both studies agree that a condensed phase is achieved. There also exists some disagreement in these studies as to the exact nature of the density distribution in DSPC monolayers at surface pressures of around 20 mN m^{-1}, with Arnold *et al* recording an apparently uniform composition at both 15 and 20 mN m^{-1}, while Kubo *et al* note solid condensed domains at 20 mN m^{-1}, but this may be a result of Arnold *et al* collecting images in regions lacking the (possibly relatively small and localised) liquid phases. For surface pressures above 20 mN m^{-1}, the two BAM studies are in good agreement as to the essentially condensed phase of DSPC monolayer.

This is in broad agreement with the results of Table 7.2, where surface pressures in the highly condensed phases of 20 mN m^{-1} and above display smaller relative decreases in permeation rate compared to the differences at lower pressures, where we would encounter changes in phase from liquid expanded to more condensed states. It may be of interest to note the appearance of local fractures in the DSPC monolayer below the macroscopically observed collapse point of the Π-A isotherms [72]; it is possible these defects could lessen the barrier properties of monolayers at surface pressures which would otherwise suggest a low permeability, thus unexpectedly reducing the efficacy of compressed monolayers in the prevention of permeation.

A potential model for the oxygen permeation rate k relates the energy required to create a space in the monolayer for the oxygen molecule according to the surface pressure of the interface, Π, and the molecular radius of the permeant, r to a rate constant [2]:

$$k = Ce^{-\beta\pi r^2\Pi} \tag{7.8}$$

where the prefactor C is dependent on the monolayer studied. Plots of $\ln(k)$ *vs* Π for the experimental results can be seen in Fig. 7.7. Although we find an approximately linear

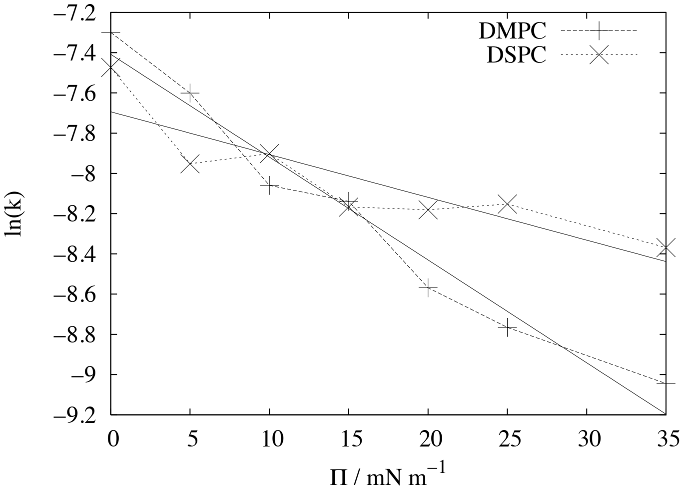

Figure 7.7: Surface pressure, Π vs experimental permeation rate constant k for DMPC and DSPC monolayers, with lines of best fit.

relationship between $\ln(k)$ and Π for the DMPC and DSPC monolayers, as predicted by Eqn. (7.8), the linear fits to the data are not parallel, suggesting that there should be a monolayer-dependent term in the exponent of Eqn. (7.8). Hence, the surface pressure model may not fully describe the permeation process, although it can serve as a broadly predictive model for the compression of monolayers with identical compositions. From the gradient of the linear fits of Π vs $ln(k)$, using Eqn. (7.8) the predicted radius of an oxygen molecule is 2.8 ± 0.8 $\AA$ (DMPC) and 1.7 ± 0.8 $\AA$ (DSPC), with the actual value thought to be around 1.5 $\AA$ [74–76].

Ideally, to compare the results of the MD simulations to experimental data, we might assume equivalence between the APL values of the monolayers in both simulation and experiment. However, slight differences in experimental concentrations could theoretically have a significant effect the surface pressure of lipids with longer acyl chains, such as DSPC, due to the steep nature of the Π/APL isotherms for such species; these differences can be encountered in the literature regarding the exact APL values at which changes in Π become evident under compression (cf. [77, 78]). The simulated monolayers also suffer from effects due to the dimensions of the simulation cell itself [79, 80]; for example, any capillary waves formed at the monolayer interface in an effort to reduce energy stored in the monolayer structure are inherently linked to the dimensions of the x, y plane for small simulations. Specifically, only capillary waves having a period which is commensurate with the size of the simulation cell on the x, y plane can form. This may restrict the natural curvature and oscillations of the monolayers, and so the experimental APL value may result from the projection of a surface containing "ripples" of many different wavelengths onto a two dimensional plane in a manner not achieved in simulation for the same apparent APL.

A more robust method for comparison would involve the surface pressures of the simulated and experimental systems. This would avoid the problems with experimental concentrations, and is to be preferred in the comparison of experimental results for the systems studied. However, the problem regarding the suppression of capillary waves in simulation remains, and care should be exercised in the direct comparison of the experimental data to the results of the simulated systems. The surface pressure, Π, can be defined in terms of the surface tension γ as follows [81]:

$$\gamma + \Pi = \gamma_{clean} \tag{7.9}$$

where γ_{clean} is the surface tension of the reference air/water interface in the absence of surfactants. The surface tension is determined from the microscopic pressure tensor, evaluated during simulation [82, 83] as

$$\gamma = \frac{1}{2} \int\limits_{-L_z/2}^{+L_z/2} \mathbf{d}z \; \left[P_N(z) - P_L(z)\right] = \frac{L_z}{2} \left[P_{zz} - \frac{1}{2}\left(P_{xx} + P_{yy}\right)\right] \tag{7.10}$$

with P_N and P_L denoting the normal and lateral pressures to the monolayer interfaces, which are averages from the system pressure tensor routinely calculated in simulation.

APL ($\mathring{A}^2$)	γ (mN m^{-1})	Π (mN m^{-1})
55	59.3 (12.9)	-7.5
57.5	70.9 (9.1)	-19.1
60	68.4 (8.4)	-16.6

Table 7.3: Mean surface tension, γ, standard deviation (bracketed) and surface pressure Π for the three simulated monolayer systems (see Eqn. (7.10)).

L_z is the length of the simulation cell normal to the monolayer interfaces and P_{xx}, P_{yy} and P_{zz} denoting the diagonal components of the pressure tensor. The prefactor of $\frac{1}{2}$ reflects the presence of 2 separate interfaces in the simulations.

The surface tensions of the three simulated DSPC systems (55, 57.5 and 60 $\mathring{A}^2$ per lipid) were calculated with Eqn. (7.10) from the individual umbrella sampling simulations. The surface tension of the clean vacuum/TIP3P interfaces were calculated from 1ns simulations of the same APL systems with the lipids removed - the resulting raw γ_{clean} values (51.8 ± 0.05 mN m^{-1}) were in agreement with the literature [84]. The mean and standard deviation of the surface tensions, and the resultant surface pressures for the simulated systems are listed in Table 7.3.

As suggested by the Π/APL isotherm for DSPC, the monolayers at these three APL values appear to be in the liquid expanded phase, with a negative surface pressure. This would not necessarily be measured in an experimental system, as the DSPC lipids would form nonuniform condensed and expanded phases [72, 73] in an attempt to create a tension-free interface. There appears to be an increase in the surface pressure for the simulated system at APL 55 $\mathring{A}^2$, but the size of the errors render this unclear. This is, however, approximately the point at which we would expect to detect an increase in Π experimentally.

By considering the angle formed between major axes of the lipid chains and the interfacial normal (see Fig. 7.8 a), it is possible to determine more subtle differences in

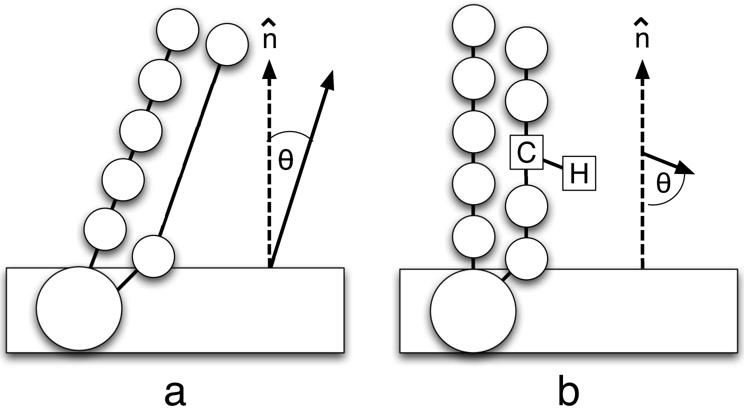

Figure 7.8: Illustration of the lipid tail major axis tilt angle (a) and S_{CD} order parameter angle (b). Interfacial normal is labelled n̂

the structure of the monolayers. The tilt angle formed between the interfacial normal and the major axis of the lipid tails is known to be dependent on the size of the lipid head group, and for lipids containing the PC head group in highly condensed phases this angle is around 30° [1, 81]. Fig. 7.9 shows the distribution of angles for the three simulated monolayers, and a clear change in both the mean and standard deviation of the tilt angles is visible for the monolayer located at $z > 0$ (Table 7.4). The same trend is not present in the monolayer at $z < 0$, demonstrating asymmetry in the system with regards to the tilting of the monolayer lipids, and neither monolayer strongly suggests a movement towards the expected tilt angle of 30° for a condensed phase featuring lipids with the PC headgroup.

Another measure of simulated structure which may be of interest is the order parameter, S_{CD}, concerning the angle θ formed between the interfacial normal and vectors describing the C-H bonds in the acyl region of the monolayer (Fig. 7.8 b). This has the advantage of being comparable to experimental data via quadrupole splitting

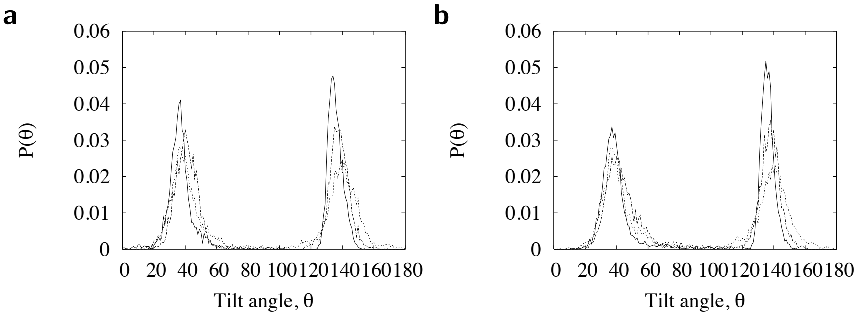

Figure 7.9: Tilt angle distributions of the lipid tail major axis and the interfacial normal $\hat{n} = (0, 0, -1)$ for simulated monolayers at APL 55 (solid line), 57.5 (dashed line) and 60 $\mathring{A}^2$ (dotted line). See also Table 7.4. **a**: Sn1 chain. **b**: Sn2 chain.

	Monolayer at $z < 0$		
APL ($\mathring{A}^2$)	Sn1, °	Sn2, °	Both, °
55	37.0 (8.0)	40.4 (12.3)	38.7 (10.5)
57.5	41.2 (6.9)	43.0 (9.2)	42.1 (8.2)
60	40.6 (10.6)	41.5 (11.5)	41.0 (11.1)
	Monolayer at $z > 0$		
	Sn1, °	Sn2, °	Both, °
55	136.1 (4.5)	136.6 (4.2)	136.4 (4.4)
57.5	136.7 (11.5)	136.4 (11.7)	136.6 (11.6)
60	139.4 (13.4)	138.7 (13.6)	139.1 (13.5)

Table 7.4: Mean and standard deviation (bracketed) of the angle formed between the major axis of the lipid acyl tails and the interfacial normal, $\hat{n} = (0, 0, -1)$, for the Sn1 and Sn2 chains of the simulated DSPC monolayers at $z < 0$ and $z > 0$. See Fig. 7.9

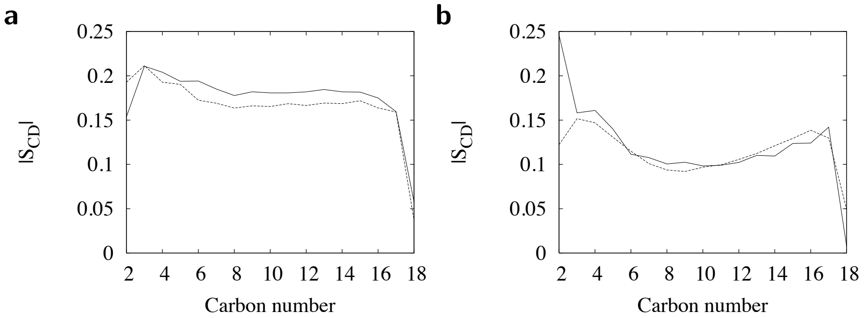

Figure 7.10: $|S_{CD}|$ order parameters for the simulated monolayers at APL 55 $\mathring{A}^2$. Solid lines denote the Sn1 chain, dotted lines the Sn2 chain. **a**: $z < 0$. **b**: $z > 0$

experiments using deuterated methylene groups [85], and is calculated in simulation as [86]:

$$S_{CD} = \left\langle \frac{3}{2}\cos^2(\theta) - \frac{1}{2} \right\rangle \tag{7.11}$$

Eqn. (7.11) predicts $|S_{CD}| = 0.5$ for C-H bonds aligned parallel to the interface (i.e. perfectly straight acyl chains with respect to the interfacial normal), and $|S_{CD}| = 0.0$ for bonds with no preferential orientation parallel to the interface [86]. The $|S_{CD}|$ values for the simulated lipid monolayers at $z < 0$ and $z > 0$ are shown in Figs. 7.10, 7.11 and 7.12. These values lie in the range we might expect for monolayers under low levels of compression, and are within the experimental values reported for monolayers and bilayers [81, 86]. The Sn1 chains (see Fig. 7.1) typically display greater order than the Sn2 chains close to the interface, in agreement with previous MD studies [81] of PC lipids.

For all simulated APL values, the $|S_{CD}|$ order decreases slightly in the intermediate methylene groups of the lipid tails, with this effect particularly prominent in the monolayer at $z > 0$ for APL 55 $\mathring{A}^2$ (Fig. 7.10b). This is in agreement with previous MD studies of PC monolayers [81], albeit the trend is somewhat more pronounced in

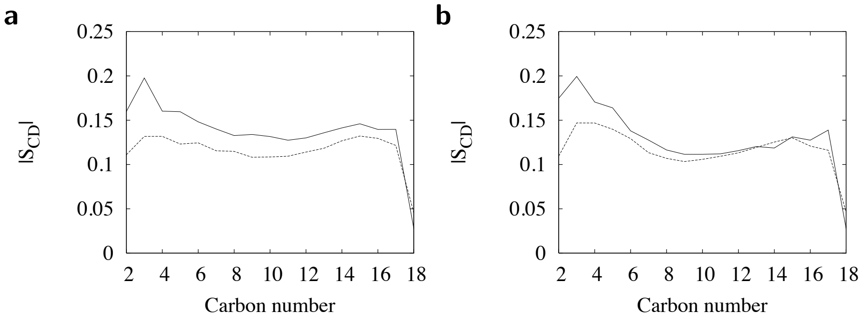

Figure 7.11: $|S_{CD}|$ order parameters for the simulated monolayers at APL 57.5 $\mathring{A}^2$. Solid lines denote the Sn1 chain, dotted lines the Sn2 chain. **a**: $z < 0$. **b**: $z > 0$

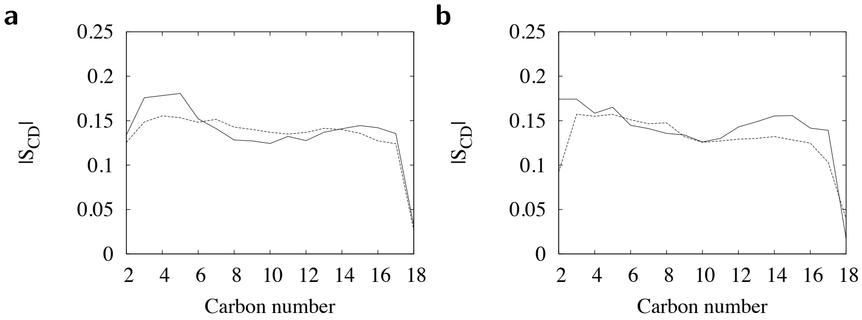

Figure 7.12: $|S_{CD}|$ order parameters for the simulated monolayers at APL 60 $\mathring{A}^2$. Solid lines denote the Sn1 chain, dotted lines the Sn2 chain. **a**: $z < 0$. **b**: $z > 0$

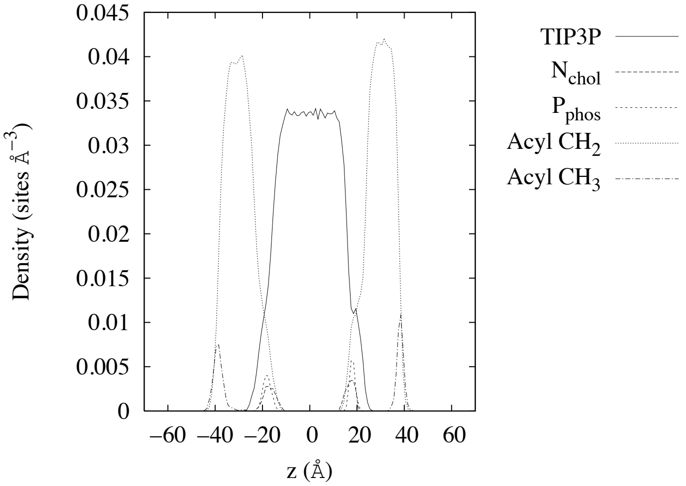

Figure 7.13: Density profile for the simulated monolayers of APL 55 $\mathring{A}^2$. Note pronounced "shoulders" in the density profiles of TIP3P and acyl CH$_2$ at $z \approx 20\mathring{A}$.

the results listed here. The predicted relationship between lipid density and S_{CD} order [87] across the three APL values is not immediately apparent, with the exception of the monolayer at $z < 0$ for APL 55 $\mathring{A}^2$, suggesting the change in lipid densities modelled here are not significant enough to unduly influence the S_{CD} order parameters.

The density profiles of the three simulated systems (Figs. 7.13, 7.14 and 7.15, bin width $\delta z = 1\mathring{A}$) are qualitatively similar, with the predictable slight increase in the density of the lipid regions under compression. There are, however, certain features which correlate with the discrepancies noted in the S_{CD} order profiles.

Immediately obvious is the "shoulder" in the density profiles for TIP3P and acyl CH$_2$ in the monolayer at $z > 0$ for APL 55 $\mathring{A}^2$ (Fig. 7.13). The solvent is apparently permeating further into the headgroup region in this monolayer, and this corresponds with an increase in the S_{CD} order for the methylene groups of the Sn1 chains closest to the interface in Fig. 7.10b. Similar features are visible in Fig. 7.14 for the monolayers at APL 57.5 $\mathring{A}^2$, and the S_{CD} order parameters for the Sn1 chains in both monolayers are

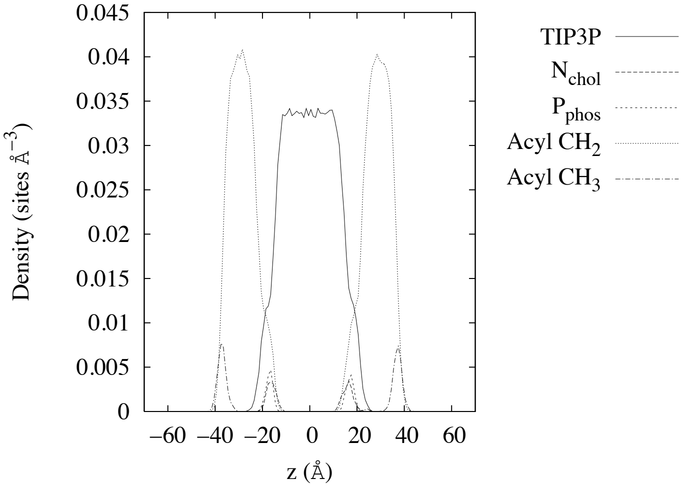

Figure 7.14: Density profile for the simulated monolayers of APL 57.5 $\mathring{A}^2$.

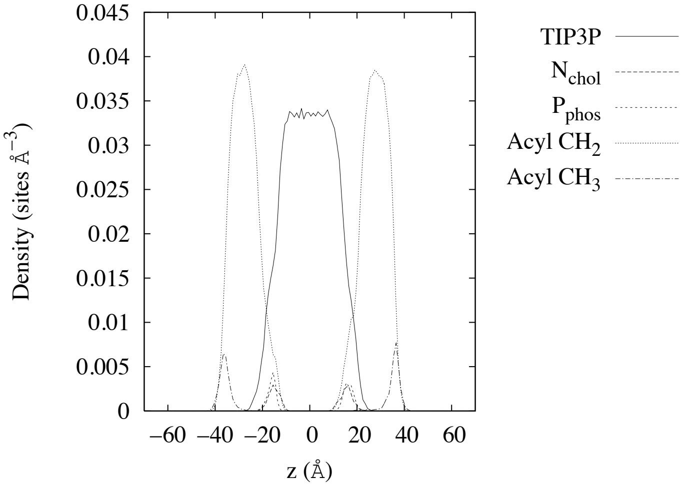

Figure 7.15: Density profile for the simulated monolayers of APL 60 $\mathring{A}^2$. Note slight "shoulder" in the density profile of acyl CH$_2$ at $z \approx 20\mathring{A}$.

higher closest to the interfacial region as shown in Fig 7.11a and b. The greater solvation of the headgroups may act as an effective "spacer", with greater solvent permeation into the further reaches of this region acting to impose greater order on the Sn1 acyl groups close to the interface. The effects on the monolayers at APL 60 $\AA^2$ are more subtle; the monolayer at $z > 0$ displays the increase in S_{CD} order towards the interface (Fig. 7.12b), but without an obvious shoulder in the TIP3P profile in the region $z \approx 20\AA$ (Fig. 7.15).

Thus, we must conclude that the monolayers at $z < 0$ and $z > 0$ are, in fact, structurally different in the case of the APL 55 $\AA^2$ simulation. These differences in structure, particularly at the interface, may affect the surface tension measurements noted earlier, and greater care should be exercised in the comparison of this set of simulations to experiment.

Given the asymmetry in the monolayers, it is interesting to now consider the excess free energy profile for oxygen permeation in the three simulated systems (Fig. 7.16), with the relative zero for each profile taken to be the minimum value in the vacuum region at $z < 0$. Separate profiles for the individual APL values are given in Figs. 7.17, 7.18 and 7.19 (note the differing scales). In these profiles, two different "peaks" may be seen; one in the interfacial region of the monolayer head groups and the TIP3P water (circa $15 \leq |z| \leq 25$, see Figs. 7.13, 7.14 and 7.15), and the other residing in the hydrocarbon-rich acyl domain of the monolayers (roughly, $25 \leq |z| \leq 40$). This suggests the presence of two separate local kinetic barriers to permeation, but in each of these cases the dominant barrier is to be found in the acyl region of the monolayers. Relative barrier heights and the ratio of the interfacial barrier to the acyl barrier (A_i/A_a) are listed in Table 7.5.

We find A_i/A_a to decrease under compression. This suggests that the relative

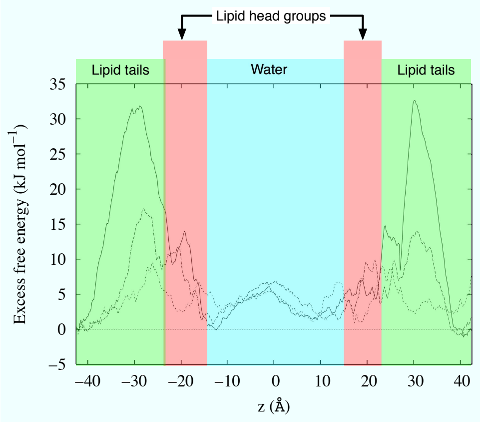

Figure 7.16: Excess free energy profiles for the 3 simulated monolayer systems; APL of 55 $\mathring{A}^2$ (solid line), 57.5 $\mathring{A}^2$ (dashed line) and 60 $\mathring{A}^2$ (dotted line). The heights of the free energy barriers at the apex of the curves in the acyl and interfacial regions (see Fig. 7.4 b, and Table 7.5) are relative to the free energy nadir in the vacuum region immediately beyond the monolayers.

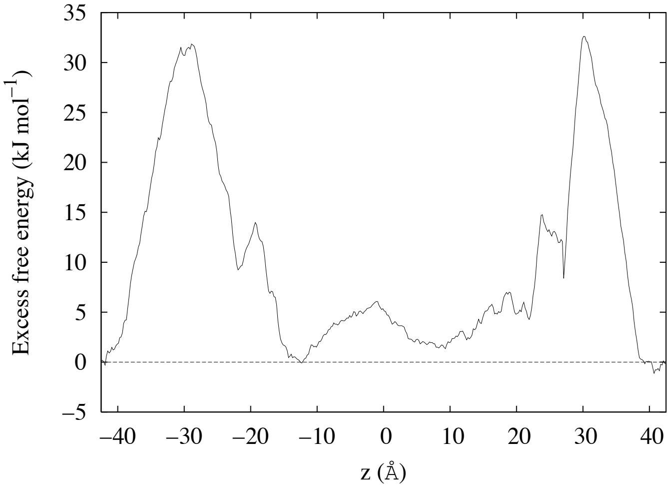

Figure 7.17: Excess free energy profile for the simulated monolayer system of APL of 55 $\mathring{A}^2$.

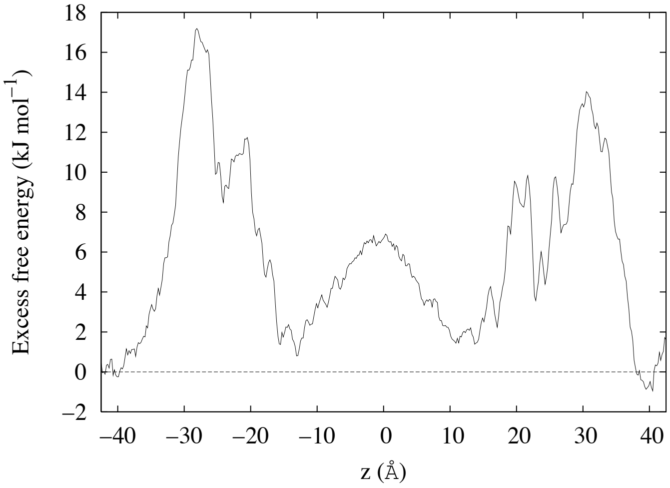

Figure 7.18: Excess free energy profile for the simulated monolayer system of APL of 57.5 $\mathring{A}^2$.

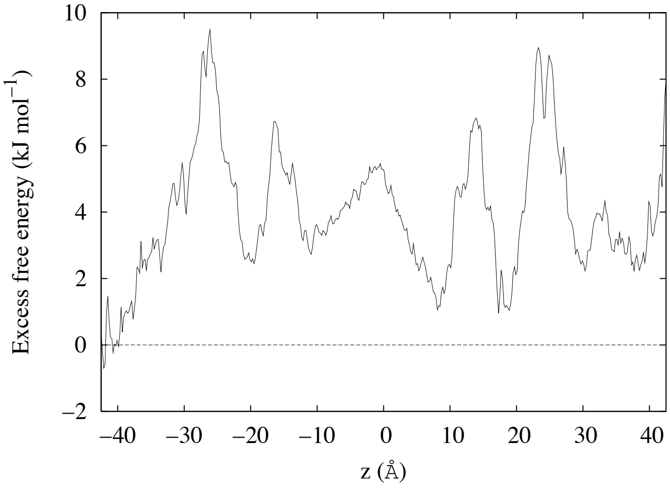

Figure 7.19: Excess free energy profile for the simulated monolayer system of APL of 60 $\mathring{A}^2$.

APL ($\mathring{A}^2$)	A_a (kJ mol^{-1})		A_i (kJ mol^{-1})		A_i/A_a	
	-z	+z	-z	+z	-z	+z
55	31.8	32.6	13.9	14.7	0.44	0.45
57.5	17.2	13.9	11.7	9.8	0.68	0.71
60	9.4	8.9	6.7	6.8	0.71	0.76

Table 7.5: Heights of the simulation free energy barriers for the acyl and interfacial regions (A_a, A_i), and the height of the interfacial free energy barrier normalised against the acyl region (A_i/A_a). Data listed under the headings "$-z$" and "$+z$" to denote the positions of the respective monolayers, see Fig. 7.4.

influence of the lipid headgroup on the excess free energy barriers decreases as the monolayers move from an expanded to a condensed phase.

The excess free energy profile for APL 55 $\mathring{A}^2$ shows both monolayers in agreement as to the interfacial free energy barrier being effectively an offshoot of the main acyl barrier, as if the main bodies of the two barriers were overlapping. There is good agreement for the heights of both barriers (see Fig. 7.17 and Table 7.5). While the acyl barrier peaks are both located at $|z| \approx 30\mathring{A}$, where the hydrocarbon density is highest, there is some disagreement between the monolayers regarding the precise location of the interfacial barrier. The monolayer at $z < 0$ places the peak of this barrier at $z \approx -20\mathring{A}$, just behind the locations of the P and N atoms in the lipid headgroups (Fig. 7.13). The monolayer at $z > 0$ places this peak at $z \approx 25\mathring{A}$, somewhat further away from the interface despite the essential equivalence in the density profiles for the location of the headgroups. This may be a result of the greater permeation of solvent into that particular monolayer.

The potentially ill-defined nature of the excess free energy profile in the interfacial region is further illustrated at APL 57.5 $\mathring{A}^2$, which has quite serious disagreement as to the nature of the interfacial barrier (Fig. 7.18). The monolayer at $z < 0$, as in the APL 55 $\mathring{A}^2$ systems, displays the interfacial barrier as an offshoot of the main acyl barrier. The monolayer at $z > 0$, however, depicts the interfacial barrier as an apparently separate feature, in common with both monolayers at APL 60 $\AA^2$ (Fig. 7.19). The relatively mobile and highly charged headgroups of the lipids, lacking the close packing and hence restricted movement of the acyl tails, no doubt thus present an influential but comparatively poorly localised effect on the polar oxygen molecule.

There exists reasonable agreement as to the maximum heights of the excess free energy barriers across both monolayers for each APL value (Figs. 7.17, 7.18, 7.19), if not their precise locations, suggesting that the ability of the oxygen to freely diffuse on the x, y plane acts to reduce the influence of localised differences in the system.

In addition to the simple surface pressure model of permeation (Eqn. (7.8)), we now consider treating the process as a reaction whose rate is related to an activation energy after Arrhenius:

$$k = Ce^{-\beta E_a} \tag{7.12}$$

here, C is a prefactor dependent on the reaction (analogous to the prefactor in Eqn. (7.8)) and E_a is the activation energy. In practice, we may substitute the activation energy for a free energy difference using a ratio of rates:

$$\begin{aligned}
\frac{k}{k_{\text{ref}}} &= \frac{Ce^{-\beta A}}{C_{\text{ref}}e^{-\beta A_{\text{ref}}}} &&= e^{-\beta \delta A} && (7.13)\\
\delta A &= A_a - A_{a,ref} &&= -k_B T \ln\left(\frac{k}{k_{\text{ref}}}\right) && (7.14)
\end{aligned}$$

where A_a and $A_{a,\text{ref}}$ are the heights of the excess free energy barriers in the rate limiting acyl region, with the implicit assumption that $C = C_{\text{ref}}$ due to the identical composition of the monolayers. Thus, given two rates of permeation it is simple to calculate a predicted free energy difference in the rate limiting region. Alternatively, given two excess free energy values we can predict the ratio of permeation rates.

From the experimental results for oxygen permeation in DSPC monolayers (Fig. 7.6, Table 7.2), and using as a reference rate the results for $\Pi = 0$ mN m^{-1}, Eqn.

Π (mN m^{-1})	δA (kJ mol^{-1})
0	0
10	1.07
20	1.76
35	2.23

Table 7.6: Predicted increases in the rate limiting excess free energy barriers for oxygen permeation, according to experimental rates from Table 7.2, for a DSPC monolayer under varying levels of compression.

APL ($\mathring{A}^2$)	k/k_{ref}		Predicted k	
	$z < 0$	$z > 0$	$z < 0$	$z > 0$
55	1.3×10^{-4}	7.4×10^{-5}	7.1×10^{-11}	4.2×10^{-12}
57.5	4.4×10^{-2}	1.3×10^{-1}	2.5×10^{-9}	7.7×10^{-9}
60	1	1	5.68×10^{-8}	5.68×10^{-8}

Table 7.7: Predicted rates of permeation given the simulated monolayer results and assuming APL 60 $\mathring{A}^2$ as the reference system.

(7.14) predicts an increase in the height of the rate limiting excess free energy barrier as detailed in Table 7.6.

To compare with simulation, we use the excess free energy profile for APL 60 $\mathring{A}^2$ as the reference interface (ie. we assume equivalence to $\Pi = 0$ mN m^{-1} and $k = 5.86 \times 10^{-8}$) and calculate the ratio of rates suggested by the dominant excess free energy barriers from the acyl regions of the simulations at APL 55 and 57.5 $\mathring{A}^2$, as given in Table 7.7. These rates are suspiciously small, as would be expected from the comparison of the predicted excess free energy barrier increases in Table 7.6 to those measured in simulation in Table 7.5; experimental rates for pressures up to 35 mN m^{-1} (Fig. 7.6, Table 7.2) are of the same order of magnitude, whereas the simulations predict rates of one to four orders of magnitude smaller than that of the reference interface due to the relatively large free energy barriers suggested by the MD simulations.

Assuming a valid mapping of simulated APL values to an experimental Π/APL isotherm, and that Eqn. (7.8) and 7.14 are applicable for this system, the experimental surface pressures required to produce rates which match those suggested by the MD simulations are ≈ 520 mN m^{-1} for APL 55 $\mathring{A}^2$ and ≈ 400 mN m^{-1} for APL 57.5 $\mathring{A}^2$, which are clearly unreasonable - the collapse point for an experimental DSPC monolayers is APL ≈ $\mathring{A}^2$ [77, 78].

It must therefore be concluded that the MD simulations performed were unable to capture the true experimental behaviours of the permeation of oxygen in DSPC monolayers. This may be due to lack of adequate equilibration time before data was collected from the simulations, or the inability of the simple NVT ensemble to impose the correct surface pressure to allow comparison to experimental results in this case.

7.6 Conclusion

The combined SECM/FEM method proved able to parameterise the first order rate constant for the permeation of gaseous oxygen through a Langmuir monolayer. The reduction in permeation due to compression in monolayers of DMPC and DSPC was modelled with a simple surface pressure description, which proved unable to consistently predict the radius of an oxygen molecule, hence suggesting the requirement of a monolayer-dependent factor in any such treatment. Molecular dynamics simulations of oxygen molecules in an all-atom DSPC monolayer failed to provide data which could accurately describe the experimental system, although the method did provide the correct qualitative trend.

Chapter 8

Weak acid permeation in lecithin bilayers

The aims of this chapter are to introduce a novel method of quantitatively measuring the permeation of weak acids in soybean lecithin bilayers using a combination of SECM, FEM and laser confocal scanning microscopy (LCSM) with fluorescein, a pH-sensitive fluorescent dye. Overton's rule is introduced, along with the formation of planar bilayer membranes (BLMs) and the principle of laser scanning confocal microscopy.

8.1 Introduction

In chapter 7, the permeation of oxygen through phospholipid monolayers formed at an air/water interface was considered. A more biologically relevant system involves the use of phospholipid bilayers, as found in cell membranes [88] and in certain subcellular organelles such as the mitochondria [89]. A simplified diagram of the bilayer structure may be seen in Fig. 8.1, but it is important to note that the composition of a bilayer is typically heterogeneous in biological systems; many different lipids are present (see

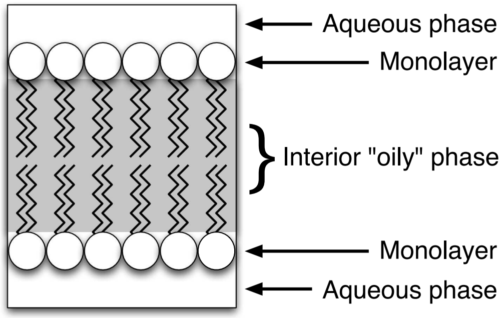

Figure 8.1: A basic bilayer structure; the acyl tails of two monolayers are arranged to minimise contact with water, creating two headgroup/aqueous interfaces on the bilayer exterior and a hydrocarbon-rich “oily” interior region.

Component	Liver	Erythrocyte	Mitochondria
Cholesterol	17	23	3
Sphingomyelin	19	18	0
PE lipid	7	18	25
PS lipid	4	7	2
PC lipid	24	17	39
Other lipid	29	17	31

Table 8.1: Lipid and lipid-type components of various human cell membranes by percentage [91].

Table 8.1, Fig. 8.2), along with cholesterol and a multitude of proteins. Even the levels of unsaturation in the lipid tails is somewhat dependent on diet [90].

The cell membrane is often described in terms of the fluid mosaic model, with the membrane lipids in a liquid phase in the range of temperatures the cell functions in. There are typically localised phase separations and inhomogeneities present in the membrane, with cholesterol and sphingolipids important to the formation and stability of these localised “rafts” [92]. Generally, van der Waals forces between neighbouring lipid tails are insufficient to ensure local phase separation but the long unsaturated tails of sphingomyelin are able to induce such a process; therefore, lipid rafts are typically rich

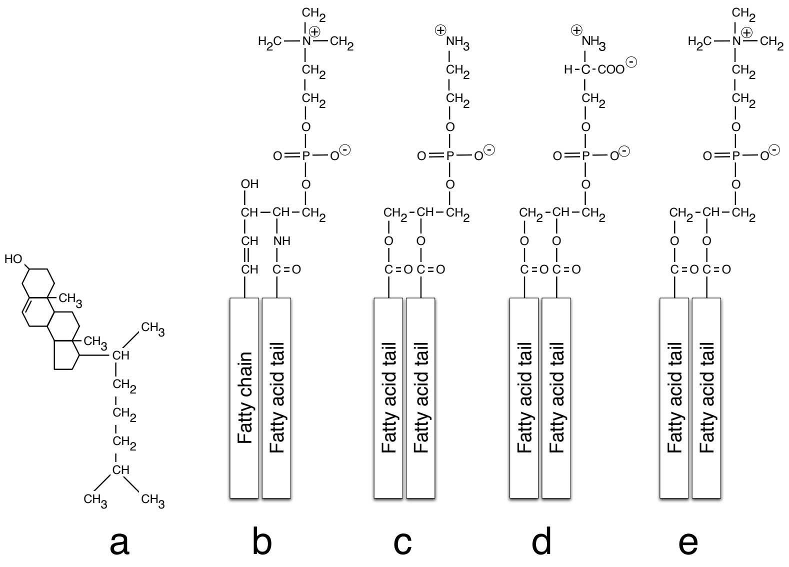

Figure 8.2: Structures of some common membrane components (see Table 8.1): **a**, cholesterol; **b**, sphingomyelin; **c**, phosphatidylethanoylamine based lipid; **d**, phosphatidylserine based lipid; **e**, phosphatidylcholine based lipid. Note the net negative charge on the phosphatidylserine head group.

in this particular phospholipid and the slightly increased membrane thickness of these localised rafts encourages the insertion and anchoring of certain proteins [88], particularly those featuring a relatively large area of of exposed hydrophobic amino acids which would otherwise be in contact with water in a thinner BLM. The large variation of components and complex phase behaviours of natural membranes has led to the extensive use of model bilayer systems. The use of single-component bilayers [93–95] or purified mixtures of particular types of lipid [6, 7, 96–107] is common, although care should be exercised in the choice of lipid used and the experimental temperature; shorter-chain and/or unsaturated lipids will remain in the fluid phase at room temperature, whereas lipids with longer saturated chains may not. This chapter describes the use of soy bean lecithin, a cholesterol and protein free mixture of phosphatidylcholine based lipids (see

Fatty acid type	Proportion, %	# acyl tail carbons	# double bonds
Palmitic	12	16	0
Stearic	4	18	0
Oleic	10	18	1
Linoleic	55	18	2

Table 8.2: Selected lipid components of soybean lecithin.

Table 8.1), as the basis of a model membrane to study the permeation of weak acids in cell membranes. Soy bean lecithin remains in a fluid phase at room temperatures [108], and can therefore be assumed to create bilayers in the biologically relevant fluid phase under experimental conditions. The function and effects of cholesterol on permeation will be further examined in Chapter 9, with the remainder of this chapter dedicated to the study of cholesterol-free bilayer membranes.

Cell membranes act as a semi-permeable barrier to control the contents of a cell with respect to the surrounding environment and maintain homeostasis [100]. Both active and passive transport are important for the regulation of a cell [109], with passive permeation operating for a wide range of neutral species [56, 110, 111]. Ionised species are very unlikely to permeate through a BLM due to changes in Born energy [112] as a result of the differing dielectric constants of the aqueous phase and the relatively uncharged membrane interior:

$$\Delta G_{\text{Born}} = -\frac{q^2}{8\pi\epsilon_0 a}\left(\frac{1}{\epsilon_m} - \frac{1}{\epsilon_w}\right) \tag{8.1}$$

where ΔG_{Born} is the difference in Born energy, q and a are the ion charge and radius, and the ϵ values concern the dielectric permittivities (ϵ_m and ϵ_w concerning the membrane interior and water respectively, with ϵ_0 the permittivity of free space). Example relative permittivities for water and alkane-style phases are circa 80 and < 5 respectively [113]. It is important to note that the presence of ion channels and other proteins can greatly increase the rate of ionic permeation, but as the lecithin bilayers discussed in this chapter are formed of purified lipid extract this is not a significant route for proton transport in the current discussions. Although the Born energy is not an absolute measure of the passive permeation behaviour for all ions [114] it serves as a useful general indication of the relative inability of charged species to travel through the cell membrane. One exception regards protons; even though protons permeate slowly through the cell membrane, they are in fact somewhat more mobile than might be expected (with orders of 10^{-6} as compared to 10^{-11} cm s^{-1} for other small ions such as sodium [114]). This is believed to be a result of the transient formation of "water wires", a series of adjacent water molecules forming a "path" through the membrane along which protons may be passed in a Grotthus-style mechanism [114].

Protons can also be passively transported by protonated weak acids carriers (*protonophores*) at a much faster rate than would otherwise occur in water wires. Weak acids form a significant class of drugs whose pharmacological action depends on reaching specific intracellular sites of action [115]. Weak acid protonophores may also exert detrimental effects on cellular processes such as oxidative phosphorylation, apoptosis [116] and photosynthesis [117]. The transport of weak acids across model cell membranes, and the determination of permeation rates, has consequently been the subject of considerable number of studies [6, 7, 94–96, 99, 106, 107, 118]. Investigations of membrane permeability have essentially utilised two configurations based on either planar BLMs [6, 7, 101, 106, 107] or liposomes [94–96, 118]. The former configuration has received most attention, with flux measurements made between adjacent stirred chambers of different composition separated by the BLM (Fig. 8.3). The flux has been determined by measuring changes in either the bulk pH [107] or the concentration of labelled tracer molecules [101] in the *trans* compartment as a function of time. Localised pH measurements close to the BLM have also been reported [97–99, 102, 103].

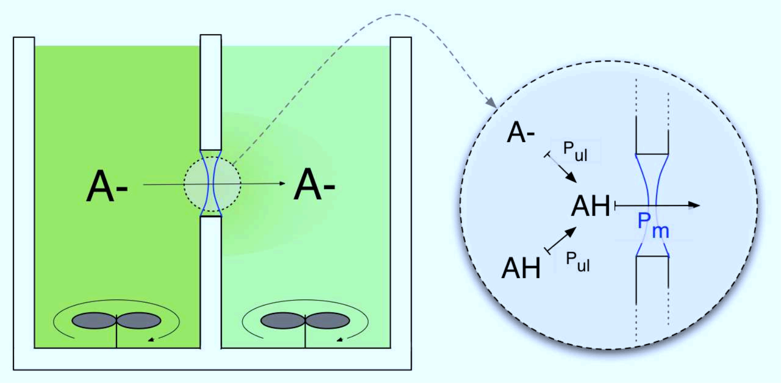

Figure 8.3: Schematic of standard BLM permeation apparatus; the permeating species is introduced to the *cis* chamber (left)and the concentration change in the *trans* chamber is examined. Mechanical stirring of the solutions in either chamber is used to reduce the width of the unstirred layer (USL). The combined permeative process is a serial combination of transport in the bulk solution and permeation through the membrane itself.

The permeation process involves mass transport of the permeant from bulk solution to the membrane surface in series with the membrane transport process (Fig. 8.3). Thus, stirring of the bulk region is essential to enhance mass transport to the BLM. Nonetheless, an "unstirred layer" (USL) generally extends for a distance on the order of several hundreds of microns on either side of the BLM in which transport of the permeant occurs predominantly by diffusion. This represents a significant resistance to the rate at which the permeant can be transported, restricting the permeation coefficients that can be measured by this technique. Moreover, neglecting to appropriately correct flux measurements for the unstirred layer necessarily leads to large errors in measured permeation coefficients [6, 101, 107].

We present here an original method to quantitatively measure the permeation of weak acids through membranes via microelectrochemistry, combined with laser confocal scanning microscopy (LCSM), and supported by finite element modelling (FEM). Dynamic electrochemistry in the form of scanning electrochemical microscopy (SECM)

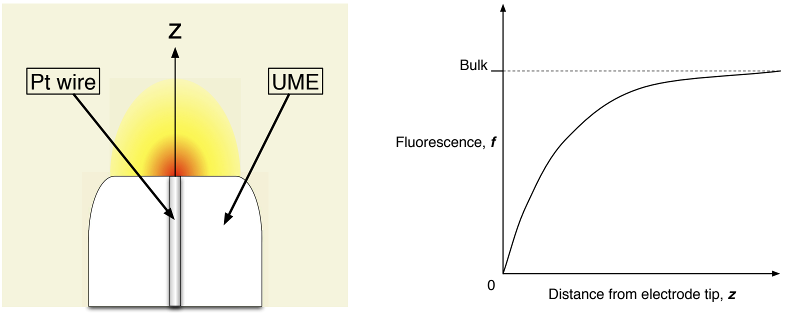

Figure 8.4: Illustration of the local pH perturbation induced by galvanostatic UME controlled oxidation of water. Protons are generated at the UME tip, generating a concentration profile along the axis marked z. This proton concentration profile is visualised via LCSM in the presence of a pH sensitive fluorescent dye, with higher pH giving a larger fluorescence signal (see Fig. 4.5)

has found some application in the study of membrane transport [24, 105, 119–122]. Our method uses an ultramicroelectrode (UME) placed close to one side of a BLM to deliver weak acids in a well defined manner by the electrogeneration of protons in the presence of weak acid anions and a trace quantity of the pH-sensitive fluorophore, fluorescein. The resulting pH distribution in the vicinity of the UME and on either side of the BLM is highly sensitive to the distribution of the weak acid and the BLM permeation coefficient, see Figs. 8.4 and 8.5. Our results provide new values for the permeation coefficients of a series of aliphatic weak acids, casting significant doubt on classical methods, while highlighting the need to reconsider the applicability of Overton's rule.

8.2 Weak acid permeation and Overton's Rule

The bilayer interior is similar in some ways to certain bulk oily phases due to a high concentration of hydrocarbon chains. It is this similarity which influenced the development of the classical Overton's Rule [123, 124], a relationship linking the partition coefficient

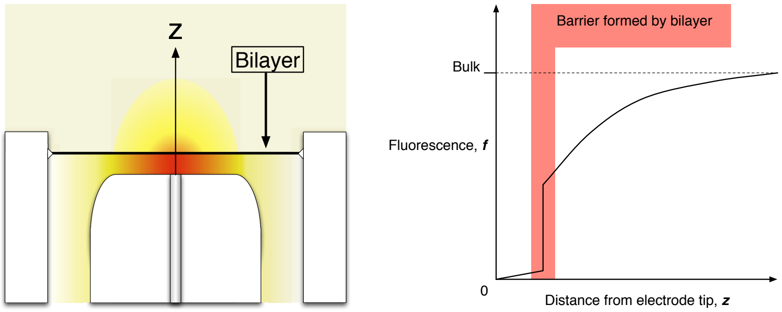

Figure 8.5: Illustration of the “step” introduced in a UME controlled proton concentration profile by the presence of a BLM; the BLM presents a barrier to the free diffusion of protons (see Fig. 8.4) which is easily identifiable in the presence of a pH sensitive fluorescent dye under LCSM visualisation. The BLM effectively prevents proton diffusion beyond the BLM, other than those carried through the BLM by a weak acid mediator.

of a species into oily and aqueous phases with the relative ability of the species to permeate through cell membranes:

$$P = \frac{KD}{l} \quad , \tag{8.2}$$

where P is the membrane permeation coefficient of the species, K is the oil/water partition coefficient and D is the diffusion coefficient of the species in the membrane with l the length over which the species diffuses (ie. the width of the membrane). While at first this may appear a reasonable formulation, the innate structure of the bilayer interior and twin interfacial regions could render such an expression of the problem unreliable; the prominent position given to the partition coefficient, K, implies that for species with reasonably similar diffusion coefficients the transport is effectively defined by the partition coefficient.

8.3 Experimental materials and Methods

8.3.1 Reagents

95% soy bean lecithin (Avanti Polar Lipids) was dissolved to a solution of 50 mg/ml in decane (99%, Alfa Aesar, Heysham, Lancs) for the experimental formation of bilayers. Aqueous carboxylic acid solutions (Fisher Scientific, UK) were made to a concentration of 1 mM with 0.1 M KCl supporting electrolyte, 5 μM of the sodium salt of fluorescein (Sigma-Aldrich) added. The pH of the weak acid solutions was adjusted with small amounts of dilute NaOH (1 mM) so that the weak acid conjugate anion was the dominant species in solution (ie. pH $\gg \mathrm{pK_a}$; see Table 8.3). The pH of the solution was checked regularly throughout the measurements using a freshly calibrated pH meter (UB-10, Denver Instruments, Arvada, Colorado), with care taken to ensure the ratio of surface area to solution volume was identical in both the experimental cell and the monitored solution to ensure accurate reflection of carbonic acid formation due to atmospheric CO_2.

8.3.2 Apparatus and methods

In order to investigate the permeation of weak acids through bilayer systems, a suitable structure is necessary to allow the formation and support of a bilayer in solution, provide control over the proton-generating UME and allow easy collection of data from a confocal microscope. The lenses of the confocal microscope are mounted such that the focal plane exists parallel to the ground, and as such remove much of the practicality of the dipping method of bilayer formation.

A custom two-piece experimental cell was constructed for the experiments in this work after Tsionsky et al [105], and is illustrated in Fig. 8.6. The dipping lens

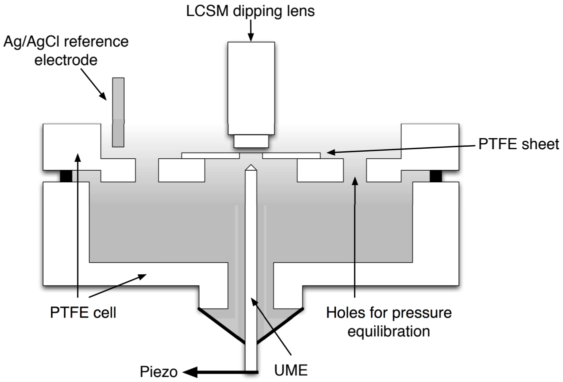

Figure 8.6: Schematic of the PTFE cell arrangement. Two PTFE sections form the upper and lower chambers, with holes for pressure equilibration [105]. The dipping lens of a LCSM is positioned at a working distance of circa 2 mm above the bilayer to inspect the formation of proton gradients.

of the confocal microscope is allowed access through the opening at the top of upper chamber the cell, and a rubber skirt attached to the lower chamber ensures a watertight seal to contain the solution despite the presence of the UME, which is thereby allowed limited movement on all three Cartesian axes to better position the reactive tip as required. A series of holes is present in the floor of the upper chamber to allow pressure equilibration in the experimental system, and the cell is mounted on the stage of the confocal microscope via an aluminium plate beneath the lower chamber. The complete cell was placed in the stage of the confocal microscope, and aqueous solution introduced via a syringe until both the lower and upper chambers were filled.

A dipping lens was positioned above the bilayer (typically at a distance of 2 mm) for the visualization (Zeiss LSM 510 laser scanning confocal microscope with Archoplan 20x/0.5W Ph2 lens). HeNe and Ar lasers at wavelengths of 543 nm and 488 nm were used for the observation of the bilayer formation and the fluorescence measurements, respectively. A two electrode galvanosatic arrangement was employed using a home built galvanostat with a AgCl-coated Ag wire reference electrode to apply a well-defined pH perturbation at the UME (25 μm diameter Pt disc, with a glass surround of 250 μm diameter) positioned beneath the bilayer. The location of the UME, fabricated as described previously [125], was controlled via micrometers with a piezoelectric positioner (E-660, Physik Instrumente) for optimum displacement.

Bilayers were formed using the paintbrush method of Mueller et al [9] supported on a circular hole of radius 0.5 mm punched into a square of PTFE sheet (0.025 mm thick, Goodfellow Cambridge Ltd) fixed as a diaphragm between the two chamber PTFE cell using wax. Although this method does not provide accurate data on the resultant BLM composition, it is a well used traditional technique and as such a good model for the production of BLMs to compare to previous studies. The membrane formation was monitored until a clear black bilayer formed, with excess lipid and solvent restricted to the periphery of the bilayer structure which was not investigated; the permeability in this region is expected to be low due to the relatively massive width of this region compared to the BLM, and the distance of this region from the UME ensuring relatively low concentration of the permeating protonated weak acid species.

After observation of the bilayer formation, the argon laser was activated and a current of 5 nA was generated at the UME with respect to the reference electrode. The system was allowed to reach a steady-state over at least 45 seconds, with a steady state visible from the fluorescence profile after circa 15 seconds, before a series of scan lines (8 signals averaged) recorded the fluorescence profile generated by the presence of fluorescein in a pH gradient. Previous work performed in the group demonstrated that immobilised fluorescein showed no degradation of signal even after repeated laser scans. Photobleaching is therefore not believed to present a problem in the system, particularly when some limited diffusion into the USL is present.

	$D_{\mathsf{HX}}(10^{-5}\ \mathrm{cm}^2\ \mathrm{s}^{-1})$	$\mathrm{pK_a}$	pH
Acetic	1.271	4.76	6.82
Butanoic	0.918	4.83	6.77
Valeric	0.817	4.83	7.10
Hexanoic	0.784	4.85	6.40

Table 8.3: Diffusion coefficients, $\mathrm{pK_a}$ values and bulk pH measurements for the FEM model. Taken from [75].

Multiple readings were taken from independent bilayers for each weak acid, with the bilayers typically forming in the same location with respect to the plane of the PTFE sheet, with a perpendicular difference of ± 3 microns. All measurements were taken at a temperature of 20 ± 2° C, and could be made repetitively within 5 minutes of forming a bilayer.

8.4 FEM simulation details

FEM simulations were performed using geometries determined from the LCSM experiments, and doubling the mesh resolution of the elements did not significantly alter the results. The galvanostatic oxidation of water at the UME quantitatively corresponds to [29]:

$$\mathrm{H_2O} - 2\mathrm{e}^- \rightarrow 2\mathrm{H}^+ + \frac{1}{2}\mathrm{O_2} \tag{8.3}$$

coupled with the following solution processes:

$$\mathrm{H}^+ + \mathrm{X}^- \rightleftharpoons \mathrm{HX} \tag{8.4}$$

$$\mathrm{OH}^- + \mathrm{H}^+ \rightleftharpoons \mathrm{H_20} \tag{8.5}$$

where X^- is an anion conjugate of a particular weak acid, HX, added to both compartments of the diffusion cell at a predefined concentration.

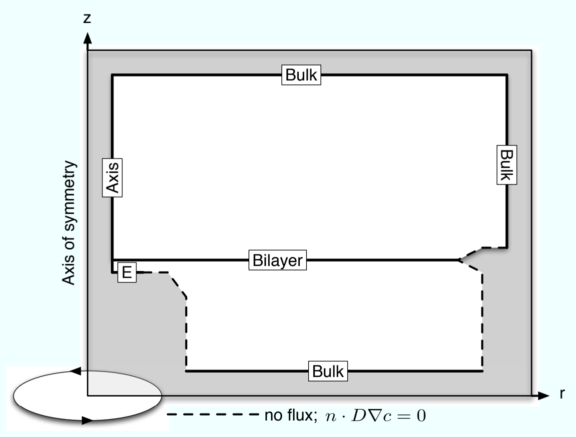

Figure 8.7: Schematic of the FEM geometry and boundaries (see text for conditions).

The influence of the protonation / deprotonation state of fluorescein was found to have no significant effect on the results due to the very low concentration of that species and was therefore ignored in the calculations. The rapidity of the solution processes on the experimental timescale meant they could be considered at an equilibrium governed by the local pH. The $\mathrm{pK_a}$ values of all species (Table 8.3) were corrected for ionic activity with the Davies equation [126] given the presence of 0.1 M KCl, and the geometry and boundary conditions were modeled with axisymmetric cylindrical geometry of the system (Fig. 8.7). A steady-state solution to Fick's second law was sought for the axisymmetric system, with diffusion coefficients, D_i, listed in Table 8.3:

$$D_i\left(\frac{\partial^2 c_i}{\partial r^2}+\frac{1}{r}\frac{\partial c_i}{\partial r}+\frac{\partial^2 c_i}{\partial z^2}\right)=0 \tag{8.6}$$

where c_i is the concentration of species i (H^+, X^- and HX), r and z are the radial and normal coordinates starting at the center of the microelectrode surface. The boundary conditions:

$$c_i = c_i^* \tag{8.7}$$

$$J_{\text{Bilayer}} = P(c_{\text{HX}}^b - c_{\text{HX}}^a) \tag{8.8}$$

$$J_{\text{Pt}} = \frac{i}{nFA} \tag{8.9}$$

with the bulk concentration, c_i^*, of a species determined from the composition of the solution, J_{Bilayer} denoting the radially dependent flux across the bilayer (with c_{HX}^b and c_{HX}^a the concentration of the protonated weak acid immediately below and above the bilayer, respectively)and J_{Pt} denoting the H^+ flux due to proton generation at the Pt electrode surface. The flux gradient on the axial boundary is $\frac{\partial c_i}{\partial r} = 0$. All PTFE and glass surfaces were modeled as no-flux boundaries, $n \cdot \nabla c_i = 0$, and unless otherwise specified other species had null fluxes on the electrode and at the BLM.

8.5 Results

To analyze experimental data, a Bezier curve [127] was fitted through the experimental fluorescence profile along the z axis, perpendicular to the bilayer with the origin at the UME tip center (Fig. 8.16). The effect of the Bezier curve-fit can be seen in Fig. 8.9, which shows a reduction in experimental noise, while preserving the essential shape and nature of the fluorescence profile. In Fig. 8.9(b) the Bezier fit was used to parameterize the FEM simulation results for the permeation coefficient of acetic acid; the best match for P from the FEM simulations was determined via minimising the RMS error between the experimental and simulated fluorescence curves. It can be seen that a value of $P = 22(\pm 4) \times 10^{-4}$ cm s^{-1} describes the data. In fitting the experimental profile to simulations, P values were also chosen to enclose the upper and lower bounds of two independent experimental fluorescence profiles on two different bilayers. The

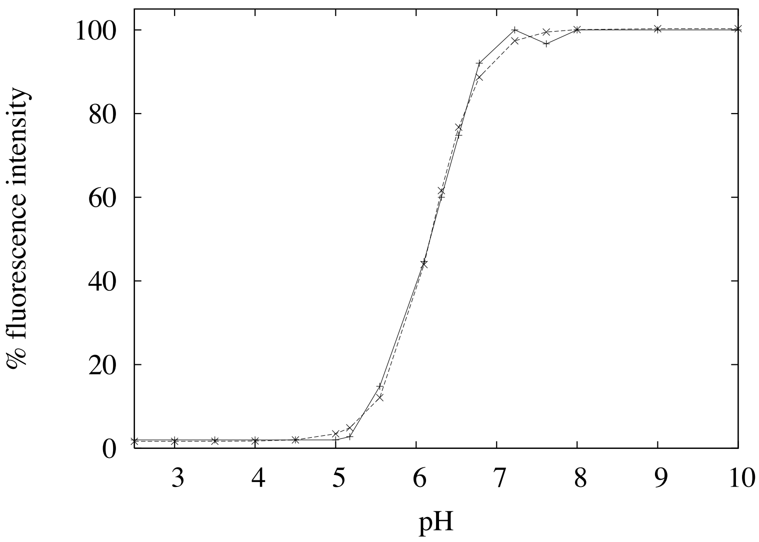

Figure 8.8: Illustration of Bezier curve fit to pH vs. fluorescence intensity of fluorescein. Solid line denotes the experimental data (see Fig. 4.5), dashed line the Bezier fit.

main region of interest lies just above the BLM, because at distances of a few hundred microns from the electrode natural convection may influence the process slightly [29]. Confidence in this assignment is further apparent by noting that the effective mass transport coefficient between the tip and BLM is $\sim D/d$, where d $(= 20\ \mu\text{m})$is the UME tip/BLM separation, $\sim$ 5 x 10^{-3} cm s^{-1}. This high mass transport coefficient allows the precise determination of P values of this order.

Fig. 8.10 shows the relative independence of the FEM analysis method with respect to the bulk pH for a freely diffusing propionic acid system (ie, no BLM, see Fig. 8.4) as detailed in 8.3.1. This figure is intended to demonstrate that slight inaccuracies in the measurement of experimental pH will not produce significantly different results for the purposes of our technique. All pH values shown in Fig. 8.10 used demonstrate excellent agreement with experiment from the UME tip to ≈ 150 μm; beyond this distance, we begin to see slight deviations from the experimentally measured fluorescence

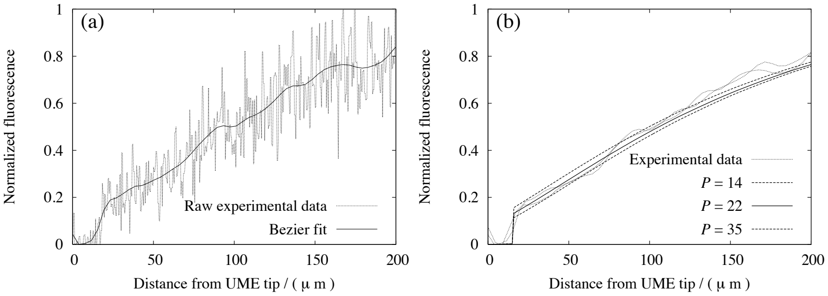

Figure 8.9: Fluorescence-distance plots normal to the center of the microelectrode: **(a)** Bezier fit to the experimental fluorescence profile of acetic acid, **(b)** fitted simulation data for P (units 10^{-4} cm s^{-1}) from FEM calculations of acetic acid under the experimental conditions and geometry.

values as convective currents begin to play a greater role. Convective currents act to mix the solution more effectively than simple models of diffusion can account for, and we would expect to see a slightly faster return to the bulk fluorescence value for experimental fluorescence profiles when compared to the FEM results. This is indeed what is shown in Fig. 8.10. As the pH perturbation applied by the generation of protons at the UME tip is in good agreement to a distance of ≈ 150 μm, we may consider the FEM results reliable before this distance.

Fig. 8.11 shows the relative independence of the FEM analysis method with respect to bulk pH in the presence of a BLM (see Fig. 8.5); for $P = 10^{-3}$ cm s^{-1}, the local pH (and hence fluorescence) at close ranges to the UME tip is effectively controlled purely by the applied current. Further away from the UME tip the bulk pH begins to manifest in terms of a greater difference in the three raw fluorescence profiles generated via FEM simulations. Upon normalising the signals at 300 μm however, the differences become much less significant; importantly, the step introduced in the fluorescence profile by the presence of the bilayer remains effectively unchanged for each of the three different bulk pH values. The same process is repeated for P values of 5×10^{-3} and 10^{-2} cm s^{-1}

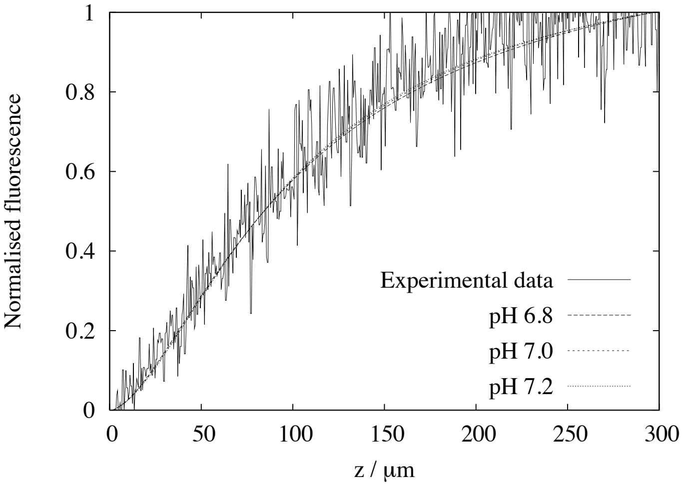

Figure 8.10: Experimental fluorescence profile for a propionic acid solution of pH 7.1, with diffusion unhindered by the presence of a BLM. Simulated fluorescence profiles for three separate bulk pH values (6.8, 7.0, 7.2) are also shown to illustrate the robust nature of the LCSM/FEM technique with respect to bulk pH.

in Figs. 8.12 and 8.13, with the same results; the step introduced in the fluorescence profile by the presence of the bilayer is not significantly affected by the bulk pH for pH ranges of 6.8 to 7.2. It is therefore concluded that experimental errors introduced in the measurement of the bulk pH are not significant with respect to this method of analysis.

Typical indicative results from the matching of experimental and simulated fluorescence profiles are shown in Fig. 8.14 for valeric and hexanoic acid. The composition of the solutions was similar to that already defined, with the bulk pH adjusted to the values in Table 8.3. As for the data in Fig. 8.9, it can be seen that the fluorescence (pH) is low on the *cis* side of the BLM, just above the UME surface. The magnitude of the fluorescence just adjacent to the *trans* side of the membrane is indicative of the extent of the permeation; the higher the permeation coefficient, the lower the fluorescence in this location, given that all the weak acids studied had similar $\mathrm{pK_a}$ values (Table 8.3).

Strikingly, on this basis, the permeation coefficient for acetic acid appears to

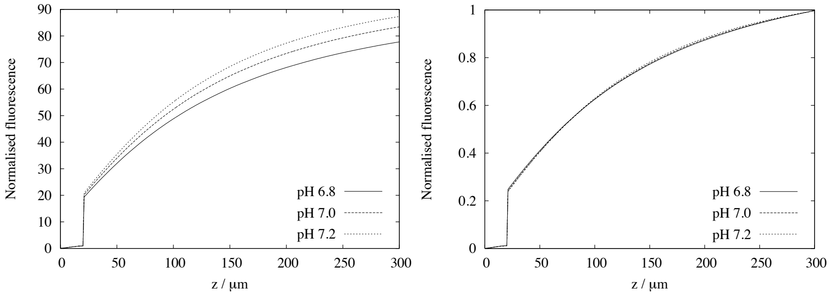

Figure 8.11: Fluorescence profiles for three separate bulk pH values, with $P = 10^{-3}$ cm s^{-1}. Left; raw profiles, right; profiles normalised at 300 μm, illustrating the relative insensitivity of the system to the bulk pH.

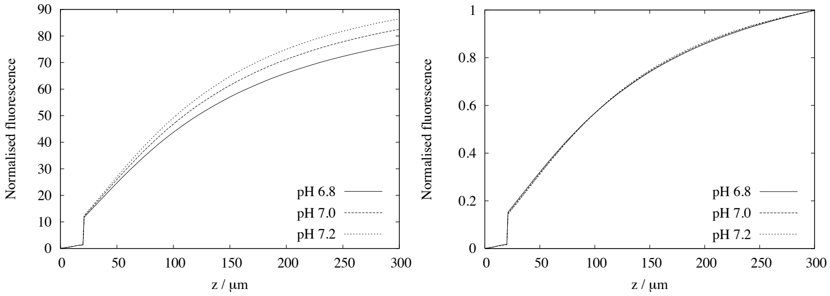

Figure 8.12: Fluorescence profiles for three separate bulk pH values, with $P = 5 \times 10^{-3}$ cm s^{-1}. Left; raw profiles, right; profiles normalised at 300 μm, illustrating the relative insensitivity of the system to the bulk pH.

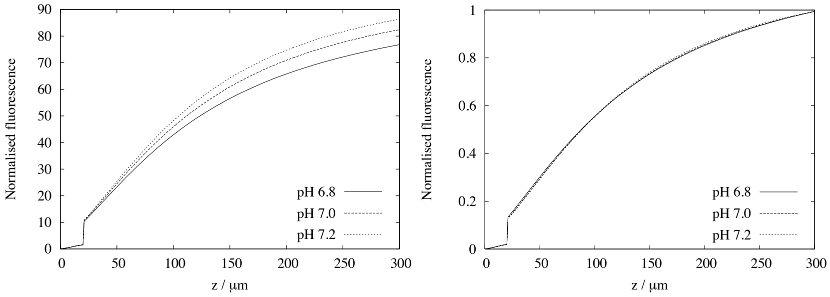

Figure 8.13: Fluorescence profiles for three separate bulk pH values, with $P = 10^{-2}$ cm s^{-1}. Left; raw profiles, right; profiles normalised at 300 μm, illustrating the relative insensitivity of the system to the bulk pH.

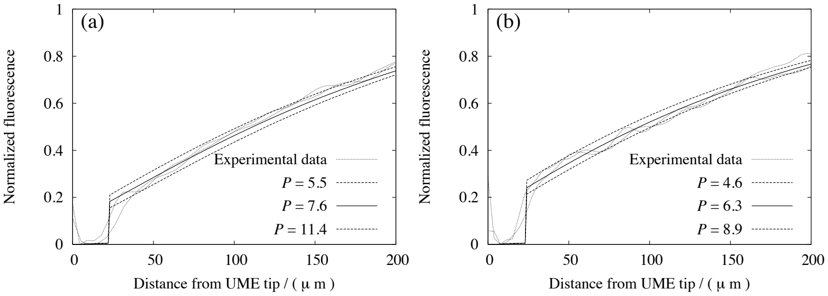

Figure 8.14: Fluorescence-distance plots normal to the center of the microelectrode: **(a)** valeric acid, **(b)** hexanoic acid. Units of P are 10^{-4} cm s^{-1}.

Reference	[107]	[96]	[101]	[6]	[95]	This study
Acetic	2.38	5		66	3.9,65	22.0
Butanoic	11.5		640	950		8.9
Valeric	18.0					7.6
Hexanoic				11000		6.33
Temp,° C	25	7	25±2	22±2	20,26	20±2

Table 8.4: Permeation coefficients from various weak acid permeation studies (units of 10^{-4} cm s^{-1}). All studies used egg PC, except DMPC in [95] and soybean PC in this study. The results from [95] represent two values if P, measured in the gel phase (20 ° C) and the liquid phase (26 ° C).

be much higher than for butanoic acid, which itself is slightly higher than that of hexanoic acid. Indeed, in contrast to previous results (Table 8.4), the homologous series of weak acids was found to follow a trend of monotonically decreasing permeation coefficient with acyl length (Fig. 8.15(a)). The trend in Fig. 8.15(a) diametrically opposes the proportionality between P and K which is generally assumed to be a product of Overton's rule.

A phosphatidylcholine BLM of the type used in this study is heterogeneous in structure and this would be expected to have some influence on the permeation process [128]. Hence, to analyze the trend in permeation coefficient with K, we have considered the partition coefficients between water and octanol, and water and olive oil

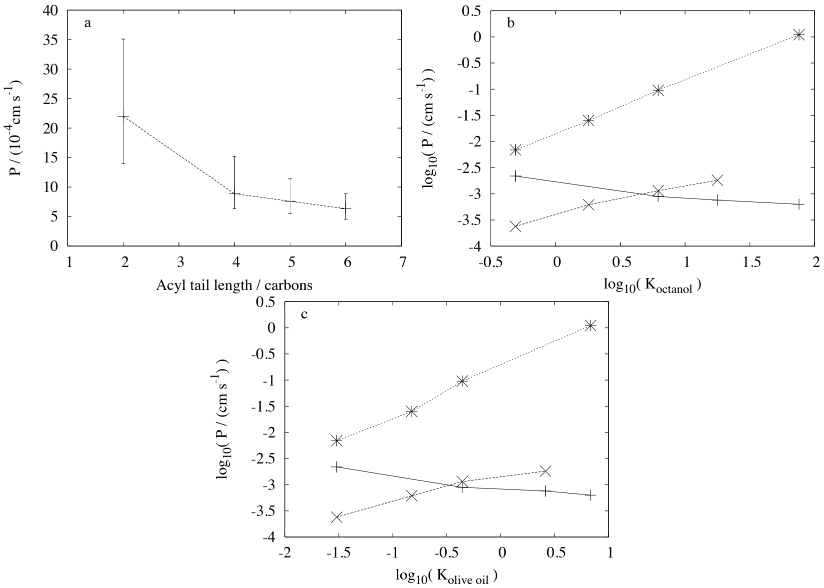

Figure 8.15: **(a)** P vs acyl length; **(b)** P vs water/octanol partition coefficient, K ($\log_{10}$ scale); **(c)** P vs water/olive oil partition coefficient, K ($\log_{10}$ scale). Key for **b**, **c**: solid line denotes data from this study, dotted line from [107] and dashed line [6]). All K values taken from [107] and [6]. Note that partition coefficient data was not available for the same weak acids in the two studies cited.

in an attempt to reflect both the innate structural order in bilayers (via octanol, and the enhanced order at the interface due to the polar -OH group), and the heterogeneous chain lengths of lecithin (via olive oil, another oily plant extract). The trend of increasing K values for the homologous weak acid series is present for both octanol and olive oil, and indeed this trend is reproduced in other oily phases [7, 107].

The results of this analysis on our data, and those of others, are summarized in Fig. 8.15(b). The difference in behavior that we observe compared to others, both in trend and magnitude, is clear and we briefly consider the reasons below. We note, however, that the trend is not entirely without precedent; gel phase DPPC studies of Xiang et al [94, 95, 118] also found a decreasing permeation coefficient from acetic to propionic acid, but for larger acids P increased again [118]. DPPC is a fully saturated lipid, thus P values are orders of magnitude smaller in the gel phase [118] and so easier to measure accurately. In constrast, soy lecithin remains in the fluid phase from 3° C to 80° C, due to the high proportion of unsaturated lipids [108].

Previous studies of permeation in BLMs have to account for USLs which limit mass transport to the BLM. When the coefficient defining mass transport from bulk solution to the BLM surface is significantly smaller than the BLM permeation coefficient, it clearly becomes increasingly difficult to measure the permeation coefficient precisely and diffusion in the USL becomes the rate limiting step of the overall BLM permeation process. Stirring of the aqueous phase and buffering at low pH in an attempt to ensure a plentiful supply of protonated weak acid can enhance mass transport, but the size of the unstirred layer and its ill-defined nature necessarily places restriction on the magnitude of membrane permeabilities that can be extracted from such measurements with confidence. In contrast, the galvanostatic generation of protons close to the *cis* surface of the BLM, and the measurement of their transport in the immediate vicinity of the

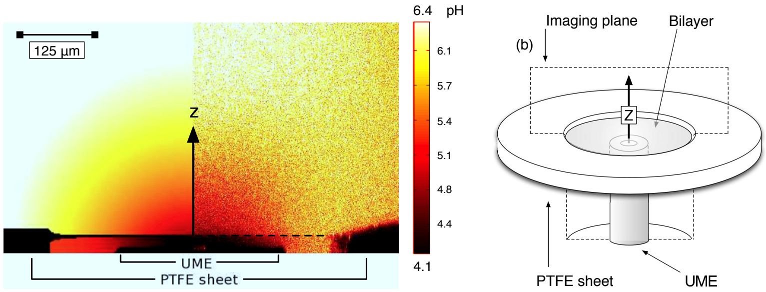

Figure 8.16: **(a)** Simulated pH profile (left) and experimental pH profile (right) for the permeation of hexanoic acid. Bilayer position is marked with a solid line in the simulated profile, and a dashed line in the experimental profile. **(b)** Illustration of the LCSM scan plane with respect to the experimental bilayer (see also Fig. 8.6).

opposing *trans* surface, should ensure that diffusion is extremely well defined and that high mass transport rates can be generated. This method is also rapid, with profiles generated in seconds as opposed to the hours which may be required for proton titration or tracer molecule measurements. Furthermore, the profiles we obtain can be valuable in their own right as indicators of USL properties, though they are not explicitly used for this purpose in the current study; for example, the distance required for the fluorescence intensity to returns to the bulk value gives an indication of the USL width for a given system.

8.6 Conclusion

Contrary to Overton's rule, we have found that the permeation coefficient of a homologous series of weak acids does not correlate with the partition coefficient. Rather, a trend of decreasing permeation coefficient with increasing acyl tail length for the transport of weak acids across model planar BLMs has been observed to correlate most closely with molecular size (and therefore diffusion coefficient). Strikingly, this violates Overton's rule and the applicability of the rule requires reassessment. The novel method described uses microelectrode generated pH gradients, coupled to LCSM visualization and FEM simulations, and is highly controlled, with the value of P as the only unknown variable used to analyse experimental data.

The method could be extended to living cells with relative ease, due to the non-toxic nature and biologically relevant pH range of the fluorescence of fluorescein or other fluorophores. More complex multi-species kinetics and equilibria could also be treated readily. The technique is of value due to the common use of weak acids and bases in pharmaceutical treatments, both of which can induce changes in pH and hence are amenable to investigation in this manner. Previous studies of protonophore transport have often relied on setting up asymmetrical bulk pH values across a membrane, the use of various buffer effects and major assumptions about the USL to infer information on permeation through membranes; such considerations are unnecessary with the method we have presented. The technique is non-invasive and allows not only the measurement of permeation through cell membranes but also the direct visualization of concentration gradients on both sides of a BLM.

Chapter 9

Weak acid permeation in POPC bilayers

Further to Chapter 8, the combined LCSM/FEM method of weak acid permeation study is applied to single component POPC bilayers, and combined POPC/cholesterol bilayers. The effects of cholesterol on the experimental permeation of weak acids is examined, and molecular dynamics simulations are employed to examine the free energy barriers presented for weak acid permeation in single component POPC bilayers.

9.1 Introduction

Chapter 8 employed soybean lecithin bilayers to study the permeation of weak acids in a biologically relevant system. Although lecithin consists of purified phosphatidylcholine based lipids, the precise structure and composition of such bilayers may be somewhat ill-defined. This chapter employs 1-palmitoyl-2-oleoyl-sn-glycero-3-phosphatidylcholine bilayers (POPC, see Fig. 9.1) to produce a more controlled experimental system for the study of weak acid permeation in the presence and absence of cholesterol, a natural

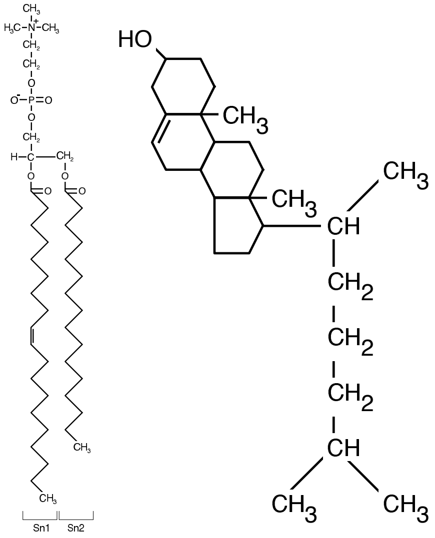

Figure 9.1: Structures of POPC (left) and cholesterol (right).

membrane component. Model bilayers formed purely of POPC have the secondary benefit of providing a more suitable experimental basis to compare to simple molecular dynamics studies of weak acid permeation in bilayers.

POPC has been used in model bilayers for the study of membrane proteins [129–133], membrane domain formation [134–137] and permeation of various substances [94, 135, 138, 139]. Like the lecithin bilayers studied in Chapter 8, POPC is comprised of lipids displaying the phosphatidylcholine headgroup, but the hydrocarbon chains are limited to a saturated Sn-2 chain of length 16 methyl and methylene groups, and an Sn-1 chain of 18 methyl and methylene groups (with a single carbon to carbon double bond between groups 8 and 9, see Fig. 9.1).

Cholesterol is a naturally occurring lipid common to the cell membranes of animal tissues and found in trace amounts in plant membranes. Cholesterol inserts just behind the lipid head groups in the head group / water interfacial region of bilayer mem-

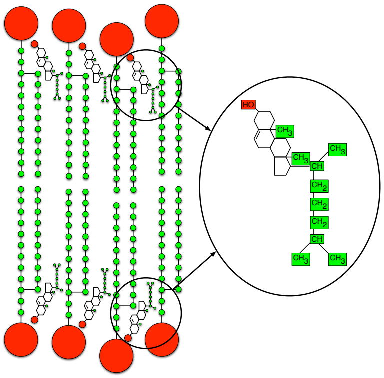

Figure 9.2: Illustration of the location of cholesterol in a typical lipid bilayer. Hydrophilic groups are shown in red, and hydrophobic groups in green. Note - cholesterol is not shown to scale with respect to the lipid molecules, and as such this diagram is purely illustrative.

branes [88] (see Fig. 9.4) and acts to regulate membrane fluidity [140–142] alongside being implicated in the formation and stability of localised lipid rafts [135, 143, 144]. The ability of cholesterol to decrease membrane fluidity in the liquid phase would be expected to reduce the passive permeation of protonated weak acid molecules due to the more densely packed and relatively static lipid molecules presenting a more rigid barrier to penetration. Using the novel experimental technique outlined in Chapter 8, the permeative behaviour of weak acids was studied for both pure POPC BLMs, and BLMs composed of a mixture of POPC and cholesterol. A series of umbrella sampling molecular dynamics simulations of a pure POPC bilayers were performed in an attempt to gain more detailed insight into the location and relative magnitudes of free energy barriers to permeation in the bilayer itself, information which would otherwise be difficult to determine experimentally.

9.2 Experimental materials and Methods

9.2.1 Reagents

$>$ 99% pure POPC (Avanti Polar Lipids) was dissolved to 25 mg/ml in decane (99% purity, Alfa Aesar, Heysham, Lancs) for the experimental formation of bilayers. POPC/cholesterol bilayers were formed with cholesterol ($>$ 98% purity, Avanti Polar Lipids) to a mole fraction of 0.4 after Xiang et al [94, 95]. Aqueous carboxylic acid solutions (Fisher Scientific, UK) were made to a concentration of 1 mM with 0.1 M KCl supporting electrolyte, 5 μM of the sodium salt of fluorescein (Sigma-Aldrich) added. The pH of the weak acid solutions was adjusted with small amounts of dilute NaOH (1 mM) so that the weak acid conjugate anion was the dominant species in solution (ie. pH $\gg \mathrm{pK_a}$; see Table 9.1). The pH of the solution was checked regularly throughout the measurements using a freshly calibrated pH meter (UB-10, Denver Instruments, Arvada, Colorado), with care taken to ensure the ratio of surface area to solution volume was identical in both the experimental cell and the monitored solution to ensure accurate reflection of carbonic acid formation due to atmospheric CO_2.

9.2.2 Apparatus and methods

The apparatus and methods of Chapter 8 were followed. Briefly, a POPC bilayer was formed with the paintbrush method, supported by a hole of radius 0.5mm punched in a PTFE sheet of thickness 0.25mm. The dipping lens of a LCSM was placed into the custom cell (approx. 2mm above the bilayer), with limited movement on all three Cartesian axes via coarse movement with micrometers and fine control with piezoelectric positioners. The formation of the bilayer was monitored with the LCSM, and a two electrode galvanosatic arrangement was employed to generate a well-defined pH peturbation at an UME.

After observation of the bilayer formation, the argon laser was activated and a current of 3 nA (as opposed to the 5nA used previously, see Chapter 8) was generated at the UME with respect to the reference electrode; this comparatively decreased current was hoped to produce a somewhat stronger fluorescence signal in the immediate *trans* side of the bilayer to assist in accurate P determination. The system was allowed to reach a steady-state over at least 45 seconds, and a series of scan lines (8 signals averaged) recorded the fluorescence profile generated by the presence of fluorescein in a pH gradient. Multiple readings were taken from independent bilayers for each weak acid. All measurements were taken at a temperature of 20 $\pm$ 2° C, and could be made repetitively within 5 minutes of forming a bilayer.

9.3 FEM simulation details

FEM simulations were performed identically to those described in Chapter 8, with appropriate changes to the FEM geometry (for example, the distance between the bilayer and the UME tip, as determined via the confocal images) and the bulk pH (as determined by the monitoring of the pH of a parallel solution with identical ratio of solution volume to surface area, to ensure the same rate of carbonic acid formation). The FEM results were parameterised from a minimum of two independently formed experimental BLMs. The diffusion coefficients, pK$_a$ values and bulk pH readings for the weak acid solutions are shown in Table 9.1.

	$D_{\mathsf{HX}}(10^{-5}\ \mathrm{cm}^2\ \mathrm{s}^{-1})$	$\mathrm{pK_a}$	pH_P	pH_{Pc}
Acetic	1.271	4.76	6.9	
Propionic	1.009	4.87	6.8	7.4
Butanoic	0.918	4.83	6.8	7.1
Valeric	0.817	4.83	7.1	7.2
Hexanoic	0.784	4.85		7.3

Table 9.1: Diffusion coefficients, $\mathrm{pK_a}$ values and bulk pH measurements for the POPC FEM simulations. pH_P denotes the measured bulk pH for the pure POPC experimental bilayers, pH_{Pc} denotes the bulk pH for the mixed POPC/cholesterol bilayer experiments. P_{Pc} for acetic acid is missing due to later analysis revealing that the BLM was in contact with the UME tip at the time of measurement, and hence the data was ignored.

9.4 MD simulation details

A bilayer patch of 104 POPC lipids (52 per monolayer) was generated using the VMD [145] membrane creation plugin, with area per lipid 64 $\mathring{A}^2$, as the Charmm force field is known to underestimate the lipid APL [146–148], the experimental values of circa 65 $\mathring{A}^2$ per lipid [133, 149, 150] were reduced slightly. After the addition of 3120 TIP3P solvent molecules at the appropriate density (giving a ratio of 30 waters per lipid, slightly less than the 32 believed to provide full solvation [69]), 8.4 ns of simulation was performed at 300 K in the NVT ensemble with timestep 2 fs to equilibrate the bilayer, with the final 4 ns used to determine an average surface tension (see Eqn. (7.10)) of 1.90 ± 3.60 mN m^{-1} using block averages of 400 ps. Protonated weak acid parameters for acetic, butanoic and hexanoic acid (structures as in Fig. 9.3) were taken from the Charmm27 force field, and relaxed structures for the weak acid insertant molecules were produced from 10 ps simulations in vacuum.

Two weak acid molecules were inserted along the reaction coordinate (z axis, defined as normal to the POPC bilayer interface) with spacings of 1 $\mathring{A}$, using a harmonic restraining potential with $k = 25$ kJ mol^{-1}. The insertion point on the x, y plane was chosen according to the identification of regions of low energy in a defined window in

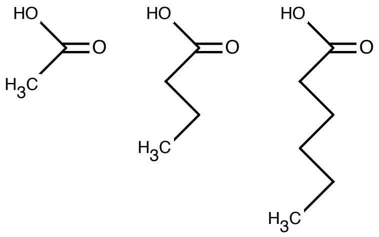

Figure 9.3: Structures of protonated weak acids used in the MD simulation of permeation in a POPC bilayer. Left to right; acetic, butanoic and hexanoic acid.

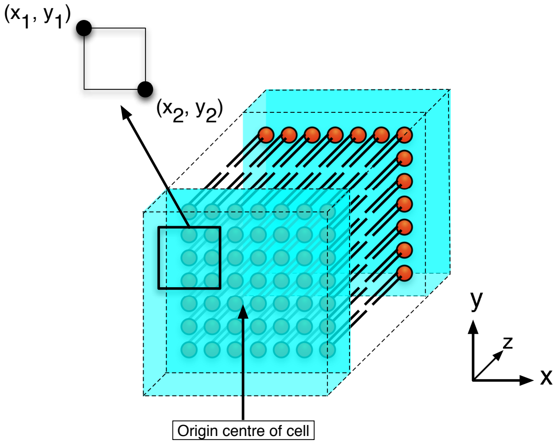

Figure 9.4: Illustration of the location of the weak acid insertion windows as detailed in Table 9.3.

that plane (Fig. 9.4). After 1 ps of simulation with capped forces (250 kT $\AA^{-1}$) to allow relaxation of unfavourable contacts, and a further 20 ps of equilibration was performed with no force capping before the main 100 ps data collection phase. All simulations were performed with the Nose-Hoover thermostat at 300 K, with a 2 fs timestep in the NVT ensemble with bound hydrogen constrained with the SHAKE algorithm [46].

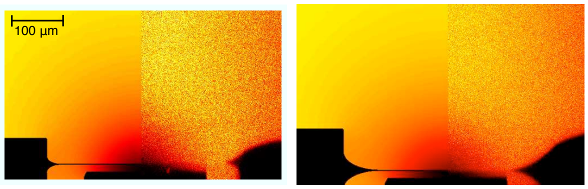

Figure 9.5: Illustration of typical experimental geometries for the POPC and POPC/cholesterol BLMs. Left; pure POPC BLM in propionic acid solution. Right; POPC/cholesterol BLM formed in propionic acid solution. Note that the differing pH values measured in each system make comparisons by eye difficult.

9.5 Results

As in Chapter 8, a Bezier curve was fitted through the experimental fluorescence profile normal to the UME tip centre to reduce the experimental noise. The same process of analysis was applied, and the results are listed in Figs. 9.6 to 9.12, and Table 9.2. Figure 9.5 illustrates typical experimental geometries, in this case for two bilayers (without cholesterol and with cholesterol) formed in a solution of propionic acid. Note that the differences between the pure POPC BLM and the POPC/cholesterol BLM in Fig. 9.5 are subtle when presented in this manner; the noisy experimental profile data has not been bezier fitted in either case, and the application of colour to the normalised images is not an exact procedure.

In figure 9.6, the fluorescence profiles of both the experimental and simulated systems are shown to 300 μm distance from the UME tip. The region of particular interest is that immediately beyond the bilayer, as this gives the clearest indication as to the permeation coefficient of the weak acid molecules; as the model does not include convective fluxes, we expect greater deviation from the experimental profile as we move over large distances towards the bulk solution in simulation. By excluding all but the immediate vicinity beyond the BLM, we better parameterise the true value of P without

Species	Length (carbons)	P_l	P_P	P_{Pc}
Acetic	2	22.0	26.7	
Propionic	3		23.3	15.6
Butanoic	4	8.9	18.9	10.0
Valeric	5	7.6	8.9	8.5
Hexanoic	6	6.33		8.0

Table 9.2: Comparison of P values, determined via the combined LCSM/FEM method, for a homologous series of weak acids in planar bilayers formed from soybean lecithin (P_l), POPC (P_P) and a POPC/cholesterol mixture (P_{Pc}). Units are 10^{-4} cm s^{-1}.

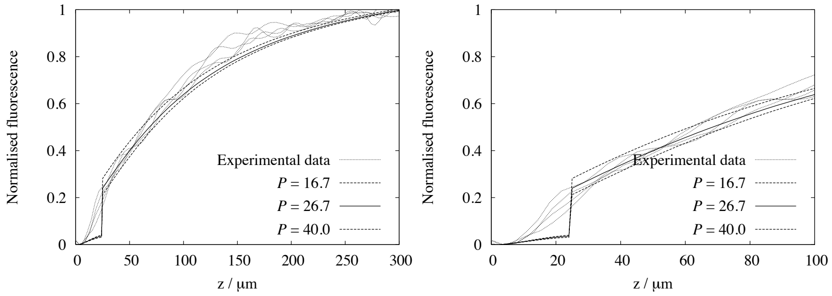

Figure 9.6: Fluorescence profiles for acetic acid in a pure POPC bilayer. Left; profile to 300 μm, right; profile to 100 μm.

undue influences from convective effects.

Once again, the trend of decreasing P with increasing acyl tail length is observed, adding further weight to the findings of Chapter 8.

A comparison of the determined P values to those of the same weak acids in the soybean lecithin bilayers of Chapter 8 is listed in Table 9.2. The results suggest that the weak acids studied are somewhat more permeable in bilayers formed of pure POPC compared to soybean lecithin. This may be on account of the saturated lipid components of soybean lecithin, and the (on average) slightly longer acyl tails of the lecithin lipids (see Table 8.1).

Previous studies have shown that the addition of cholesterol to a BLM decreases the permeation of a host of substances (see, for example, [94, 95]). Therefore, we expect

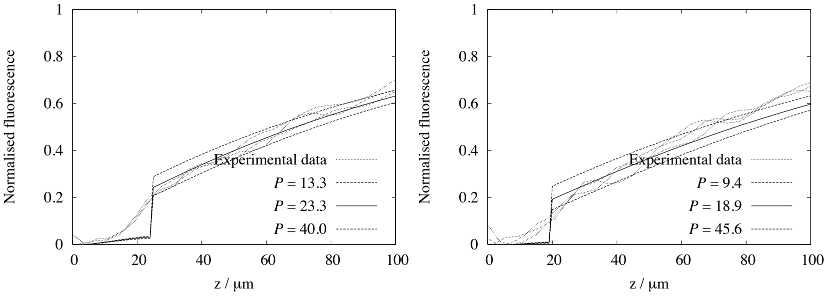

Figure 9.7: Fluorescence profiles for propionic acid (left) and butanoic acid (right) in a pure POPC bilayer.

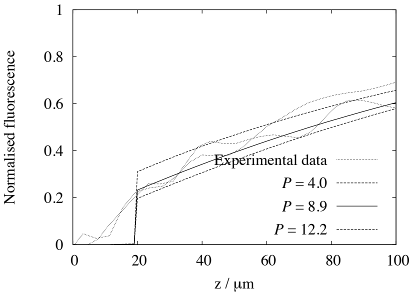

Figure 9.8: Fluorescence profiles for valeric acid in a pure POPC bilayer.

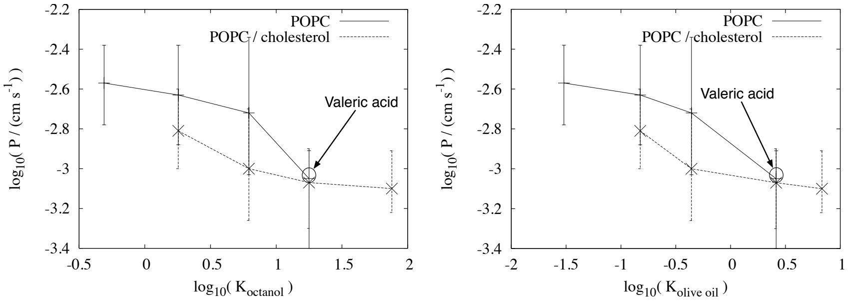

Figure 9.9: P vs water / octanol partition coefficient, $K_{octanol}$ (left) and P vs water / olive oil partition coefficient, $K_{oliveoil}$ (both log10 scale). Valeric acid P for pure POPC bilayer is highlighted. See Table 9.2.

the addition of a 0.4 mole fraction of cholesterol to the POPC bilayers to significantly hinder the permeation of the weak acids studied, and indeed this is the case for propionic and butanoic acid. Table 9.2 lists the P values determined using the LCSM/FEM method, and a notable result concerns the permeation coefficient of valeric acid in the pure POPC BLM compared to the POPC/cholesterol BLM; the two experimental bilayers studied for the cholesterol-free BLM permeation of valeric acid are in somewhat poor agreement compared to the other experimental systems studied (Figs. 9.8, 9.9). Despite this, the trend of decreasing P with increasing weak acid size (Fig. 9.9) remains present in both the pure POPC and the POPC/cholesterol BLMs.

Another possible explanation for the unexpectedly slight difference between the P values of valeric acid in the pure POPC and POPC/cholesterol BLMs regards the phase of the BLM itself. It has been shown that the addition of cholesterol to a BLM can result in enhanced isothermal permeation, provided a change in phase takes place; Xiang and Anderson [95] found that acetic acid permeation in a DPPC unilamellar vesicle at 30 °C increased from 2.7×10^{-5} to 2.5×10^{-4} cm s^{-1} as the BLM moved from the gel to liquid phase. DPPC is a fully saturated lipid, and hence BLMs formed from this

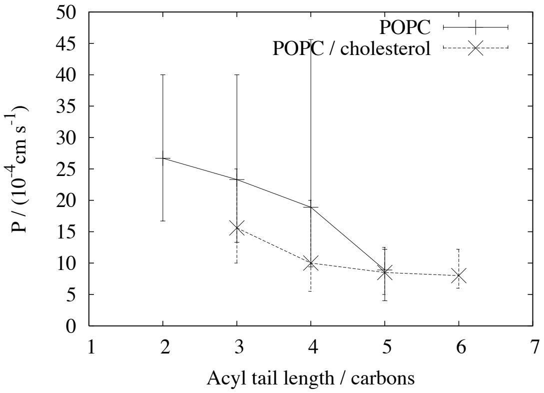

Figure 9.10: Acyl tail length vs P for the weak acid permeants in pure POPC and mixed POPC/cholesterol bilayers. See Table 9.2.

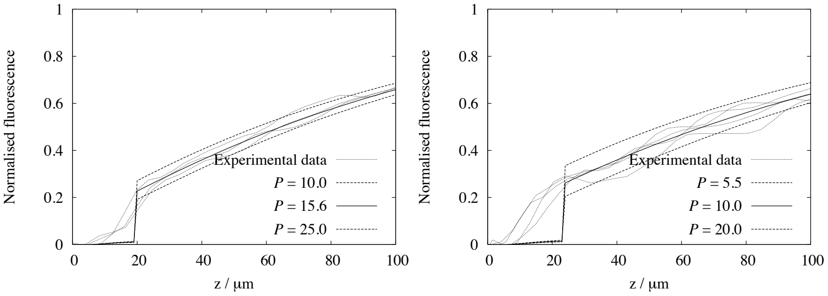

Figure 9.11: Fluorescence profiles for propionic acid (left) and butanoic acid (right) in a POPC / cholesterol bilayer.

surfactant would be expected to remain in the gel phase for a range of temperatures higher than that of BLMs formed from the unsaturated POPC. It is therefore unlikely that a comparable phase change from gel to liquid occurs in the POPC BLMs studied in this work, as POPC/cholesterol mixtures of the appropriate ratio have been observed to remain in the liquid phase at room temperature [151].

Umbrella sampling MD simulations of a POPC bilayer and three weak acid molecules were performed in an attempt to discover a molecular basis for the experimental results. Two separate insertion windows were used for each weak acid, producing

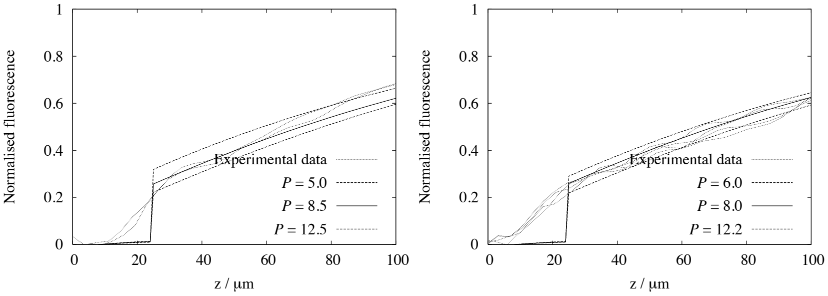

Figure 9.12: Fluorescence profiles for valeric acid (left) and hexanoic acid (right) in a POPC / cholesterol bilayer.

two sets of simulations (and hence two excess free energy profiles) per weak acid. The details for each set of simulations are listed in Table 9.3. The density profiles and S$_{CD}$ parameters for the last 4 ns of the equilibration run are shown in Figs. 9.13 and 9.14; the density profiles are in agreement with the literature ([148], simulated at 310 K as opposed to 300 K as in this study). The surface tension is somewhat at odds with prior studies; Gullingsrud and Schulten [148] calculated the surface tension of an APL 64 $\mathring{A}^2$ POPC bilayer with 128 lipid molecules at 310 K to be 37.2 mN m^{-1} over 2.4 ns, albeit using a numerical quadrature over a local pressure profile with less detailed electrostatics (post-processing the coordinates, saved every 500 fs, with a real-space cutoff of 18 $\mathring{A}$). The S$_{CD}$ order parameters are in agreement with the same study by Gullingsrud and Schulten, but with marginally less order present in the initial methyl groups immediately behind the lipid head groups.

As can be seen from Table 9.3, the insertion of the weak acid molecules has a very pronounced effect on the surface tension of the POPC bilayers; the equilibration simulations of the POPC bilayer alone produced a surface tension of 1.90 mN m^{-1}, showing the bilayer to be in a slightly expanded state compared to an idealised tension-free bilayer. The umbrella sampling simulations show the insertion of the weak acids

Simulation set	Insertion window ($\AA$)		γ (mN m^{-1})	σ
Acetic 1	-20,-20	: -10,-10	-77.5	10.1
Acetic 2	10,10	: 20,20	-76.4	8.1
Butanoic 1	-20,-20	: -10,-10	-73.1	9.4
Butanoic 2	10,10	: 20,20	-75.9	8.5
Hexanoic 1	-20,-20	: -10,-10	-77.0	9.9
Hexanoic 2	10,10	: 20,20	-77.2	9.3

Table 9.3: Details of the POPC/weak acid MD simulations performed with $\delta z = 1.0\AA$ and $k = 25$ kJ mol^{-1}. *Insertion window* refers to the region on the x, y plane in which a low energy insertion point was sought for the weak acid, see Fig. 9.4. The surface tension, γ, was evaluated according to Eqn. (7.10) for all the individual simulations in a particular set, with standard deviation, σ, as listed.

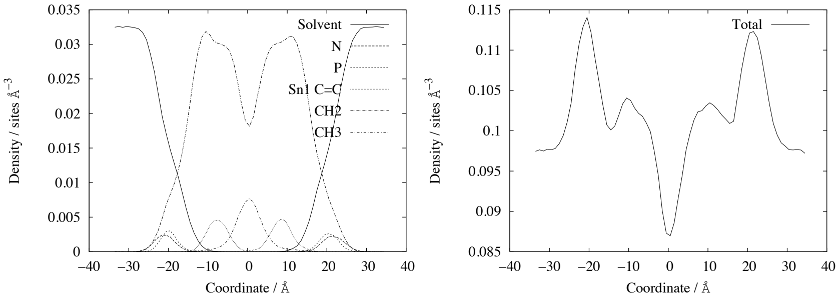

Figure 9.13: MD density profiles for selected groups (left) and the total density profile (right) for the latter 4 ns of the POPC bilayer simulation equilibrations.

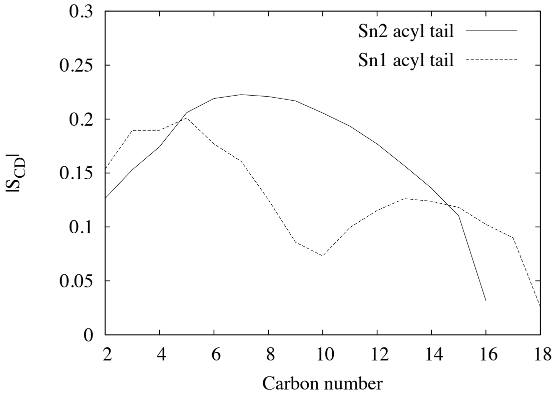

Figure 9.14: MD S_{CD} order parameter for the latter 4 ns of the POPC bilayer equilibration.

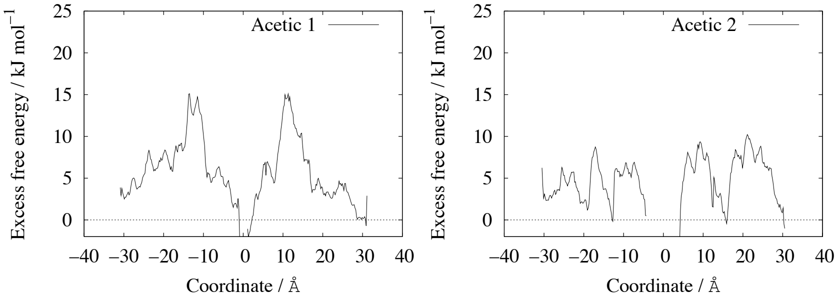

Figure 9.15: Excess free energy profiles for a protonated acetic acid molecule in a POPC bilayer. Left; Acetic 1. Right; Acetic 2 (see Table 9.3).

changes the surface tension dramatically, to ≈ -75 mN m^{-1}; this indication that the POPC membrane develops relatively heavy lateral compression due to the insertion of the weak acid molecules is a further indication of the poorly suited nature of the simple NVT ensemble to these simulations; surface tension is the derivative of free energy with respect to surface area, and so in nature one would expect the BLM to attempt to minimise the excess free energy by changing the surface area to reduce surface tension. Such movements are restricted in a fixed volume simulation with periodic boundary conditions.

The resultant excess free energy profiles for the POPC/weak acid simulations are shown in Figures 9.15 to 9.17. Very poor agreement is visible between the two profiles for each weak acid, and even between the individual monolayers at $z < 0$ and $z > 0$ in the same profile (see, for example, Fig. 9.17). Any gaps in the excess free energy profiles and related data are a result of the simulations being abandoned when it became apparent that the data was of poor quality, in an attempt to conserve limited CPU resources.

An attempt was made to gather better data using closer staggering of the insertion points on the reaction coordinate ($\delta z = 0.5\mathring{A}$) with a stronger restraining potential

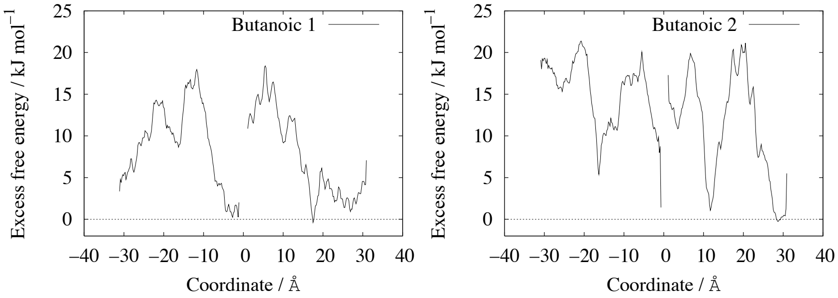

Figure 9.16: Excess free energy profiles for a protonated butanoic acid molecule in a POPC bilayer. Left; Butanoic 1. Right; Butanoic 2 (see Table 9.3).

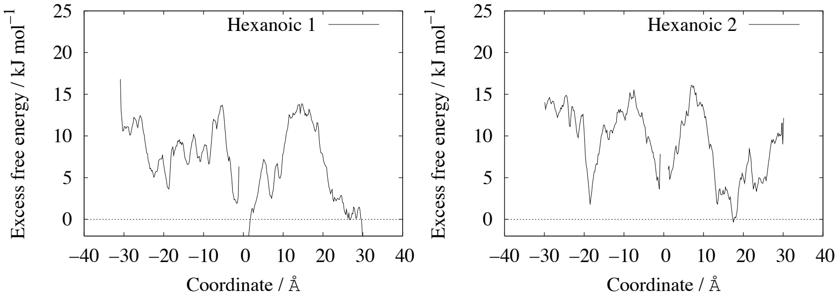

Figure 9.17: Excess free energy profiles for a protonated hexanoic acid molecule in a POPC bilayer. Left; Hexanoic 1. Right; Hexanoic 2 (see Table 9.3).

Simulation set	Insertion window ($\AA$)	γ (mN m^{-1})	σ
Acetic 3	-20,-20 : -10,-10	-74.6	8.1
Butanoic 3	-20,-20 : -10,-10	-74.8	9.3
Hexanoic 3	-20,-20 : -10,-10	-78.4	10.0

Table 9.4: Details of the POPC/weak acid MD simulations performed with $\delta z = 0.5\AA$ and $k = 50$ kJ mol^{-1}. *Insertion window* refers to the region on the x, y plane in which a low energy insertion point was sought for the weak acid, see Fig. 9.4. The surface tension, γ, was evaluated according to Eqn. (7.10) for all the individual simulations in a particular set, with standard deviation, σ, as listed.

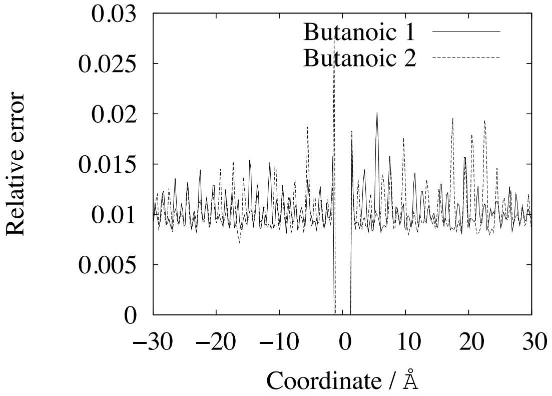

Figure 9.18: Relative errors for the Butanoic 1 and Butanoic 2 simulation sets (see Table 9.4).

($k = 50$ kJ mol^{-1}). The relative errors [55] of the initial simulations suggested many regions of the profiles which would benefit from more data (eg. Fig. 9.18), and so entire excess free energy profiles were produced (Table 9.4). This provided no improvement in the quality of the excess free energy profiles (Fig. 9.20).

The dramatic changes to the surface tension in the POPC bilayer as a result of the insertion of the weak acid molecules renders the simulated data difficult to compare to any experimental measurements. In any case, the profiles might be expected to display greater symmetry around $z = 0$, and greater agreement between the two profiles for each weak acid type. This disagreement and asymmetry might be examined in terms of the spacial range sampled by the weak acid molecules. Fig. 9.19 details the RMS

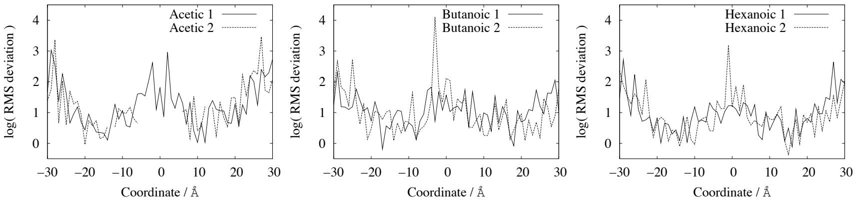

Figure 9.19: RMS deviation from the initial insertion position on the x, y plane for the MD simulations detailed in Table 9.19.

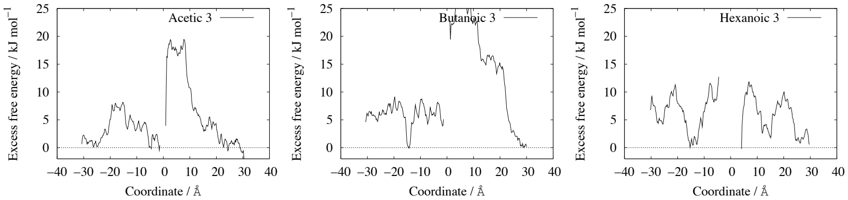

Figure 9.20: Excess free energy profiles for protonated acetic (left), butanoic (middle) and hexanoic (right) acids using a staggering of 0.5 $\mathring{A}$ on the z coordinate and a restraining potential with $k = 50$ kJ mol^{-1}, see Table 9.4.

deviation from the initial insertion points for each of the simulation sets. Whereas Figs. 9.15 - 9.17 might suggest significant differences in the spacial sampling between the two sets of simulations for each weak acid (and also between the monolayers at $z < 0$ and $z > 0$ in each weak acid set), the RMS deviations show this not to be the case. The general features in Fig. 9.19 are in agreement; the RMS deviations are relatively large in the aqueous regions, and in the central region between the monolayer leaflets, and relatively low in the region just behind the lipid head groups.

No conclusions can be drawn from the MD data with regards to the experimental systems due to their overall poor quality, and the lack of agreement between the profiles. Even were the results to have significant agreement, the unphysical surface tensions introduced by the insertion of the weak acid molecules into the simulated bilayers compared to what might be expected in the experimental systems renders any comparison to the LCSM/FEM data inappropriate.

9.6 Conclusion

As was found in Chapter 8, the overall trend in the BLM permeation coefficients of a homologous series of weak acid molecules is that of a decreasing P as the weak acid molecules increase in size. This trend persists when a 0.4 mole fraction of cholesterol is introduced to the BLMs, and the P values in the POPC/cholesterol BLMs are lower than those of the pure POPC BLMs, in general agreement with the previous understanding of the effects of cholesterol in BLMs and with previous studies of permeation in such systems. This further weakens the idea that the permeative ability of such weak acids in a BLM is essentially predicted by their partition coefficients between aqueous and oily phases.

The use of a simple NVT ensemble in the MD study of weak acid excess free energy profiles was shown to be problematic, with poor agreement between profiles for the same weak acid species in differing regions of a POPC BLM. This suggests that the simple z-axis reaction coordinate is an insufficient model for the simulation timescales used here. The significant changes in surface tension render such simulations problematic to compare to experimental systems without appropriate modifications to the simulation techniques detailed in this chapter.

Chapter 10

Mass transport in the unstirred layer

Chapters 8 and 9 introduced a combined LCSM/FEM method for the study of experimental mass transport and the permeation of weak acids through model BLMs. The application of this method to soybean lecithin, pure POPC and POPC/cholesterol bilayers was found to produce a trend of decreasing permeation coefficient, P, with increasing weak acid size in contrast to prior results [6, 7, 107]. The current chapter details a theoretical model of mass transport in the unstirred layer adjacent to a BLM in an attempt to gain a more detailed understanding of the behaviour of experimental systems, and examine any weaknesses and limitations of the traditional experimental designs for the study of permeation in BLMs.

10.1 Introduction

The experimental measurement of BLM permeation coefficients has traditionally proven problematic. Such permeation is effectively a serial combination of two or more pro-

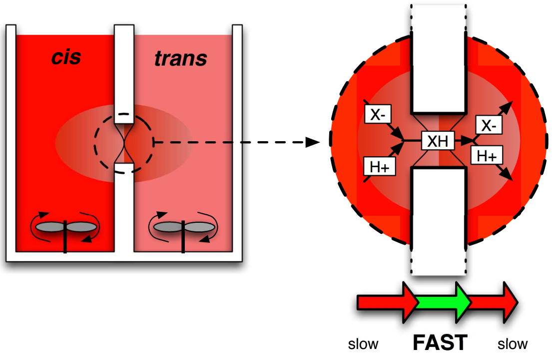

Figure 10.1: Illustration of the traditional permeation study, with two stirred chambers separated by a BLM; the permeant species is added to the *cis* chamber, and the change in concentrations in the *trans* chamber is measured. Where permeation through the BLM is fast, the rate limiting step may be the mass transport of protons, along with both the charged and neutral species, through the bulk solution and USL.

cesses; where mass transport through the membrane is fast compared to the bulk solvent, the rate limiting step lies not in the permeation across the BLM but instead in the provision of sufficient permeant molecules to the BLM via mass transport in the bulk solution. The maximum P values which can be directly measured in traditional experiments therefore become limited by the characteristics of the permeant in bulk solution and the USL.

The problem of mass transport the USL has been approached in a variety of ways; vigorous stirring of the mixtures in the *cis* and *trans* chambers [6, 101–103] (see Fig. 10.1) has been used in an attempt to reduce the USL via enhanced convective mixing. This can engender poor definition of the USL and may be difficult to reproduce accurately. In addition, too vigorous a stirring regime may be able to render the bilayers unstable due to pressure differences and stress. As only the neutral form of a weak acid is significant in BLM permeation [112], protons are transported from the *cis* chamber to the *trans* chamber as protonated weak acid molecules permeate. A subsequent lack of protons in the *cis* USL may be avoided with buffering at a suitable pH (with respect to the pK_a of the weak acid permeant), thus ensuring a relatively large quantity of the neutral species adjacent to the BLM in the *cis* chamber. This can certainly enhance the effective flux [5], but the details of the buffer and reactions in the USL become significant [5, 112] and potential buffer exhaustion in the USL introduces a further complication during analysis of the system.

It is therefore difficult to directly measure P values for weak acids without artifacts from the experimental design. The combined LCSM/FEM method of Chapters 8 and 9 is a significant improvement due to well-defined USL geometry and good control over mass transport due to the generation of a local pH perturbation in the USL itself, clearly measured to a micron scale via LCSM. The use of a UME to constantly generate protons in the direct vicinity of the BLM in the *cis* chamber ensures no exhaustion of the permeating neutral species, and the measurement of the fluorescence profile produced in the *trans* chamber gives explicit information regarding the USL itself, and it is against this information that we parameterise the permeation of the weak acids. The use of a fluorescence technique allows the measurement of such information without disturbing the local *trans* environment with electrodes [99, 103, 105] or other experimental equipment, and the innate ability to examine the geometry of the bilayer itself helps prevent errors in the estimation of the BLM surface area available for permeation which can affect flux estimation.

The conventional experimental systems will be examined using FEM simulations of mass transport and permeation, parameterised by USL width (δ), permeation coefficient (P) and buffer strength. This allows a “global” view of the parameter space, clarifying limits in the traditional experimental methods of P measurement.

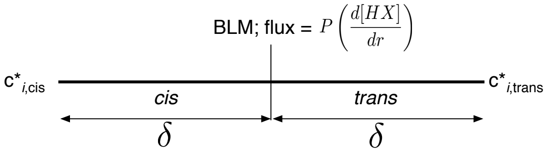

Figure 10.2: The 1-D FEM geometry used in the simulations. The boundary conditions at the exterior of the *cis* and *trans* chambers are the bulk concentrations for each species i, $c^*_{i,\text{cis}}$ and $c^*_{i,\text{trans}}$. Flux across the central bilayer is determined as shown, with r the special coordinate.

	Cis chamber					*Trans* chamber	
System	pH	NaSal	Sal	NaCl	NaCit	pH	NaPhos
1	3.9	35.7	4.3	150		7.4	150
2	4.9	39.5	0.5	150		7.4	150
3	4.9	39.5	0.5		150	7.4	150

Table 10.1: Compositions by concentration (mM) of the simulated systems, from [5]. Species are labelled as follows: NaSal, sodium salicylate; Sal, salicylic acid; NaCit, trisodium citrate; NaPhos, trisodium phosphate.

10.2 FEM simulation details

The simulations are based on the experimental systems studies by Gutknecht and Tosteson [5]. A model weak acid, based on salicylic acid, was used for the permeating species. The *trans* chamber was held at a pH of 7.4, far in excess of the pK$_a$ value of the weak acid (Table 10.3), using a phosphate buffer of concentration 150 mM. This ensures deprotonation after permeation, preventing the backflux of protonated weak acids and hence approximating the "true" one-way flux of the permeant molecules. The *cis* chamber was subjected to varying pH and buffer strength at a constant ionic strength, as detailed in Table 10.1. The diffusion coefficients and equilibria for the various species are listed in Tables 10.2 and 10.3. The self-ionization of water was not found to have significant effects on the system, and hence was ignored in the calculations.

The geometry of the FEM consisted of a 1-D model with *cis* and *trans* com-

Species	D (10^{-5} cm^2 s^{-1})
HX	0.959
H^+	7.6
X^-	0.959
CitHHH	0.623
CitHH$^-$	0.623
CitH^{2-}	0.623
Cit^{3-}	0.623
PhosHHH	0.824
PhosHH$^-$	0.824
PhosH^{2-}	0.824
Phos^{3-}	0.824

Table 10.2: Modelled species and respective diffusion coefficients for the FEM simulations of the USL. All D values are taken from [75]. *Cit* refers to constituents of the citrate buffer used in the *cis* chamber, and *Phos* relates to the components of the phosphate buffer in the *trans* chamber. Note that the same D values are used for all buffer species of the same family; this is not expected to significantly affect the findings.

partments separated by a model bilayer (Figure 10.2). Only the protonated weak acid was allowed to permeate this bilayer, as permeation of charged species is an extremely rare event [112] and will not affect the results of the calculations. The width of the *cis* and *trans* USL was identical in each individual simulation, although this parameter was varied across simulations to examine the dependency of flux on δ. Although δ is not constant for the different species in such systems [103], as smaller molecules with a larger D apparently experience larger USL widths, the apparent relationship of δ to the third root of the ratio of the D values suggests that δ will be very similar for all species except H^+. The simulations are therefore providing a larger supply of H^+ than might be expected in experimental systems of this type on account of the smaller USL width, effectively enhancing the supply of protons to the USL. The simulations are therefore considered to be a best-case scenario for systems which are potentially mass transport limited with respect to the permeation of protonated carrier molecules.

The boundary conditions for the bulk regime beyond the USL regions were held

Equilibria	pK_a
$HX \rightleftharpoons X^- + H^+$	3.0
$CitHHH \rightleftharpoons CitHH^- + H^+$	3.13
$CitHH \rightleftharpoons CitH^{2-} + H^+$	4.76
$CitH \rightleftharpoons Cit^{3-} + H^+$	6.40
$PhosHHH \rightleftharpoons PhosHH^- + H^+$	2.16
$PhosHH \rightleftharpoons PhosH^{2-} + H^+$	7.21
$PhosH \rightleftharpoons Phos^{3-} + H^+$	12.32

Table 10.3: Equilibria and pK_a values used in the FEM simulations of the USL. All pK_a values are taken from [75], and are activity corrected using the Davies formulation [126]. *Cit* refers to constituents of the citrate buffer used in the *cis* chamber, and *Phos* relates to the components of the phosphate buffer in the *trans* chamber.

at the equilibrium bulk concentrations of the constituent species of each chamber, determined via solving the linear equations governing the equilibria (Table 10.3), with appropriate activity corrections via the Davies equation [126]. All simulations were repeated with $\delta \pm 10\%$ to simulate "experimental uncertainty" in this parameter, and the results of these simulations were used to produce any error bars found in this chapter.

10.3 Results

For each of the systems studied, P was varied from 0 to 600×10^{-4} cm s^{-1} and δ from 50 to 600 μm. Surface plots of the flux in unbuffered *cis* USLs display the same characteristic shape (Figs. 10.3 and 10.4); for small values of δ, the flux can be seen to be dependent on P, and relatively large P values can be determined from measuring an experimental flux. The simulations with bulk *cis* pH of 3.9 show fluxes approximately ten times higher than those present in the same systems with bulk *cis* pH of 4.9; this is to be expected, as the bulk concentrations of H^+ are approximately ten times larger in the former systems compared to the latter. For $\delta > \approx 100$ μm, the flux quickly becomes limited, and reaches a plateau for $P > \approx 50 \times 10^{-4}$ cm s^{-1} as the local provision of

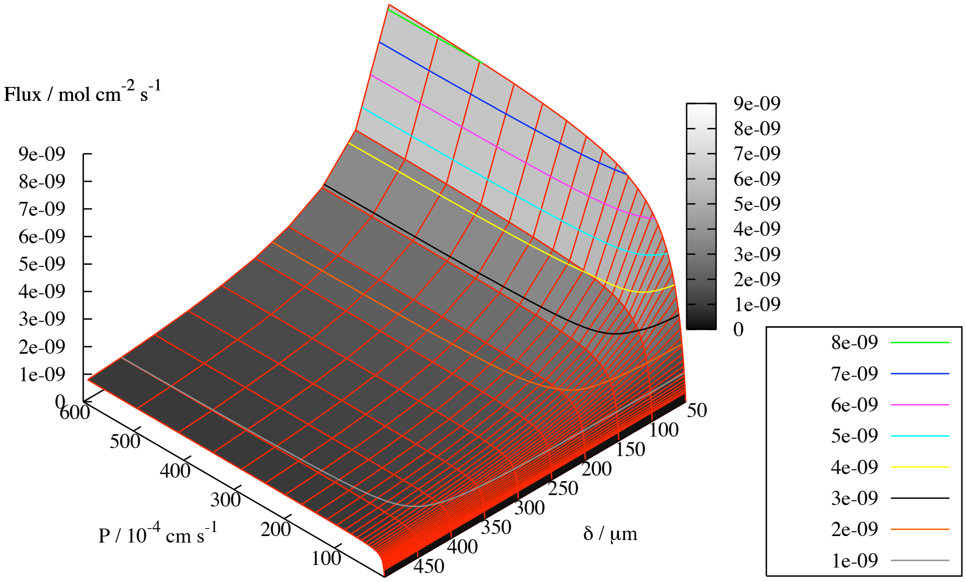

Figure 10.3: Surface plot for flux in the unbuffered *cis* system of pH 3.9. Flux contours are shown as coloured lines as in the boxed key.

permeating weak acid molecules becomes insufficient to produce fluxes larger than this mass transport limited value.

Figs. 10.5 and 10.6 show P vs flux for a selection of three USL widths. Where $\delta = 50$ μm, a limiting flux is not attained, but the graphs indicate that this situation would occur shortly after the maximum P value tested, $P = 600 \times 10^{-4}$ cm s^{-1}. For δ values of 250 and 500 μm, the limiting flux can be clearly seen to manifest beyond $\approx 50 \times 10^{-4}$ cm s^{-1}.

These findings follow an intuitive understanding of the problems of the USL; for sufficiently large P, the measured flux becomes limited by the exhaustion of the permeating species at the *cis* side of the BLM. In such cases the maximum flux has an upper limit, regardless of P for the permeating species. This upper limit is dependent on the transfer of suitable permeant molecules from the bulk solution across the USL

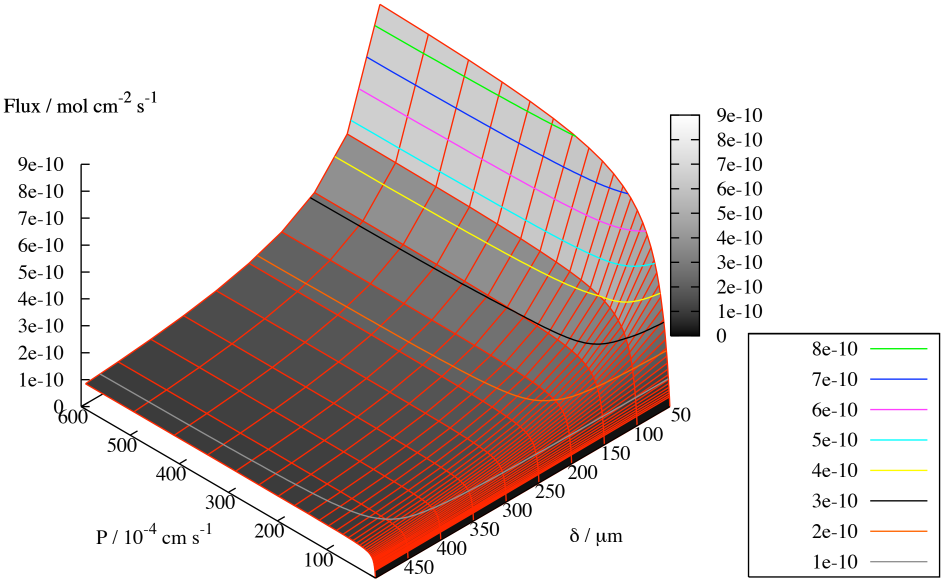

Figure 10.4: Surface plot for flux in the unbuffered *cis* system of pH 4.9. Flux contours are shown as coloured lines as in the boxed key.

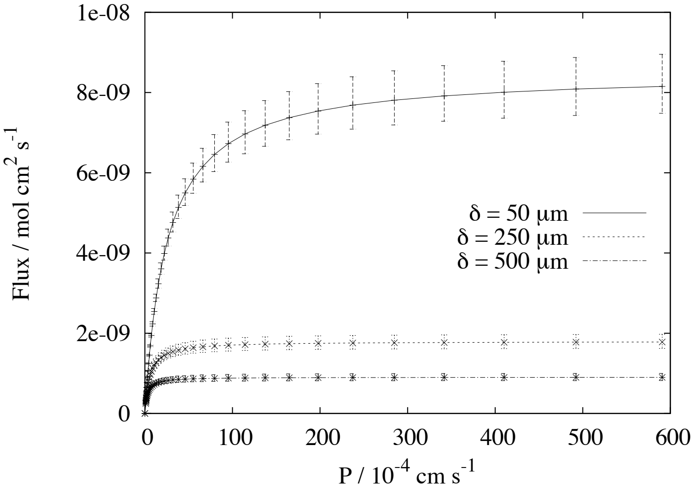

Figure 10.5: P vs flux in the unbuffered *cis* system of pH 3.9 for three USL widths, see Fig. 10.3. Error bars are generated from USL width ± 10%.

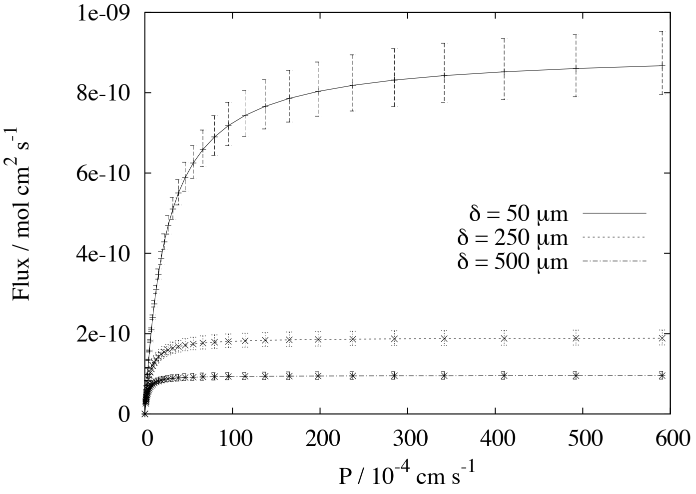

Figure 10.6: P vs flux in the unbuffered *cis* system of pH 4.9 for three USL widths, see Fig. 10.4. Error bars are generated from USL width ± 10%.

to the BLM. The presence of a plateau in the flux ensures that ranges of P above some limiting value are effectively indistinguishable in experiment, and hence there is a maximum P which can be accurately determined from direct experimental measurement in the presence of an USL.

As typical USL widths are thought to be on the order of hundreds of microns [100, 102, 103, 112], the problems for experimental P determination in unbuffered systems are severe. The combined LCSM/FEM method detailed in Chapters 8 and 9 significantly reduces these problems, however, as the distance between the electrode tip (effectively a “bulk” value, due to the predictable and well-defined electrogeneration of protons) and the bilayer can easily be set to less than 50 μm, and the constant production of protonated weak acid molecules ensures a low pH along with large and well-defined mass transport of permeants to the bilayer; therefore, we may expect to measure far larger P values using this technique compared to experiments utilising the the more conventional techniques. Mass transport from the bulk solution, and the presence of the USL, no longer prevent the determination of large P values in experiment. For sufficiently small P the fluxes for δ at 50, 250 and 500 μm coincide (Figs. 10.5 and 10.6), showing the USL width is irrelevant as mass transport from the bulk across the USL is fast enough to replace the permeating species.

The final system consists of a heavily buffered *cis* chamber at pH 4.9 (see Table 10.1). The flux characteristics of this system are shown in Figs. 10.7 and 10.8, with the behaviour of this system clearly different to the two unbuffered systems discussed previously; although the maximum flux measured for very small δ is somewhat lower than the maximum in the unbuffered system of pH 3.9 (as expected, due to the abundance of protons by comparison), the flux remains high as δ is increased. As with the unbuffered systems, for sufficiently small P, the fluxes in a buffered system for δ at 50, 250 and 500 μm coincide (Fig. 10.8). This shows that sufficient protonated weak acid molecules are made available to replace the permeating species for a wide range of USL widths, provided P is small. The magnitudes of P for which these graphs coincide are found to be somewhat larger than in the unbuffered systems (Figs. 10.5 and 10.6), showing that the buffered USL allows fluxes which are independent of δ over a wider range, as expected. It is also interesting to note the relatively small error bars for $\delta = 50$ μm in Fig. 10.8 compared to Figs. 10.5 and 10.6; the buffering acts to smooth out the fast changes in flux with varying USL width that we observe in the unbuffered systems, and hence bounds of ± 10% of the target USL width produces smaller error bars than in the unbuffered systems for $\delta = 50$ μm.

Local pH profiles for the three systems studied at the maximum measured flux are presented in Fig. 10.9. Note that in certain cases, such as in the buffered system and where $\delta = 50$ μm in the unbuffered systems, this is not the theoretical maximum flux but simply the maximum attained in these simulations. The pH reported in these

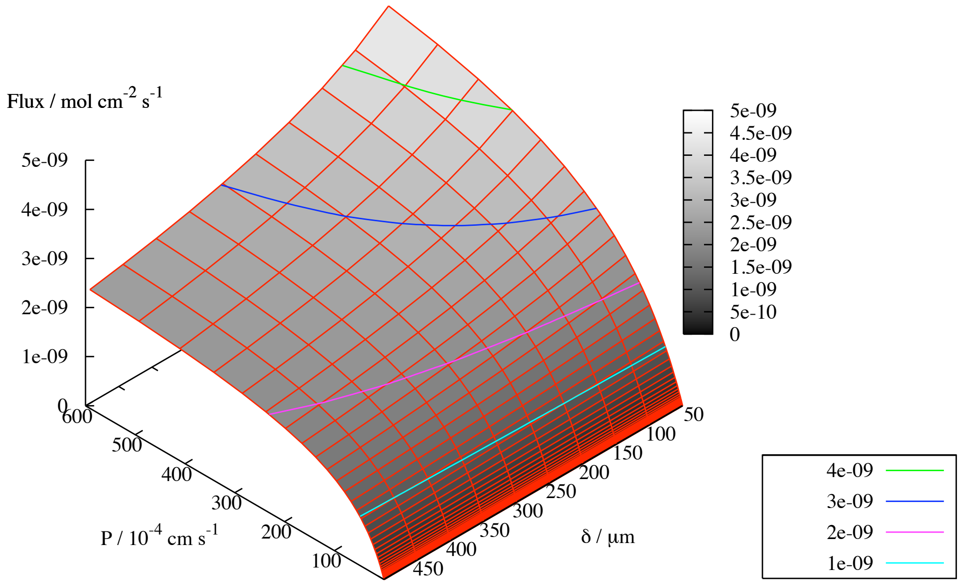

Figure 10.7: Surface plot for flux in the buffered *cis* system of pH 4.9. Flux contours are shown as coloured lines as in the boxed key.

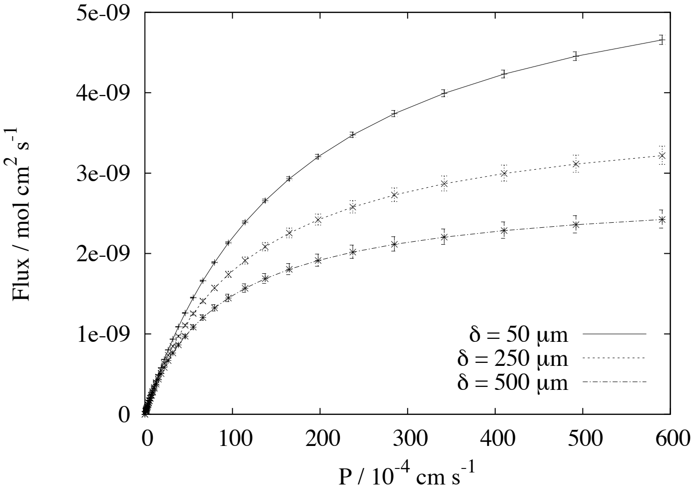

Figure 10.8: P vs flux in the buffered *cis* system of pH 4.9 for three USL widths, see Fig. 10.7. Error bars are generated from USL width ± 10%.

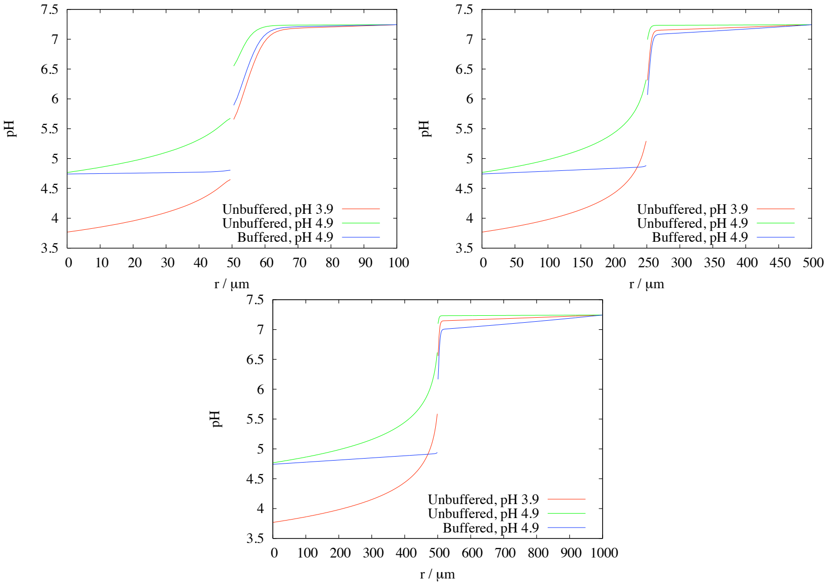

Figure 10.9: USL location vs pH for the systems in Table 10.1. Clockwise from top left; $\delta = 50$ μm, $\delta = 250$ μm and $\delta = 500$ μm. The graphs are discontinuous at the location of the BLM in the centre of the simulations.

graphs is from the *actual* [H$^+$], corrected for the ionic environment in the experimental measurements. As the concentration of a changed species in an ionic environment is higher than a simple measurement of its activity would suggest, the "true" pH shown here is slightly lower than would be reported by pH measurements in experiment.

For the three values of δ used in Fig. 10.9, the buffered system maintains a more regular local pH compared to the unbuffered systems. Low proton concentrations (and so high pH values) in unbuffered *cis* USLs lead to a shortage of protonated carriers (see pK$_a$ values in Table 10.3), which are the primary permeating species [112], and hence the flux is hindered without sufficient diffusion of protons and protonated weak acids into the USL from the bulk solution. A suitably buffered system provides a pH level which ensures a relatively plentiful supply of protonated weak acid molecules in the USL, and hence the flux is limited only for values of P and δ which are sufficiently high so as to overwhelm both mass transport from the bulk and the buffering capacity of the USL.

Fig. 10.10 shows the concentration profiles of the protonated weak acid molecules in the *cis* USLs of the systems listed in Table 10.1, using the three δ values discussed previously, under two conditions; first, at the maximum flux achieved in each simulation in an attempt to examine potentially mass transport limited permeation - again it is worth emphasising that the maximum flux measured in certain simulations is not the theoretical maximum flux. The second condition is at *half* of the maximum simulated flux, a situation designed to examine the concentration profiles where the permeation process is *not* mass transport limited. For the systems where a flux plateau is reached in simulation (unbuffered systems with δ of 250 and 500 μm), the concentration of protonated weak acids in the immediate *cis* vicinity of the BLM can be seen to be minimal. For the simulations which are not yet at the flux plateau and therefore not attaining the theoretical maximum flux (all buffered systems, and unbuffered systems where $\delta = 50$ μm - see Figs. 10.5, 10.6 and 10.8) the concentration of the protonated weak acid is larger in this region, as expected. Fig. 10.11 shows the same graphs for the weak acid anion, and demonstrates the greater interconversion of the anionic form of the permeant into the neutral species due to the buffer maintaining a low pH in the *cis* USL.

In light of these results, the flux measurements reported by Gutknecht and Tosteson [5] (Table 10.4) for the unbuffered systems are not entirely unreasonable, provided the USL width is $\approx$ 50μm or less. Although the flux can be highly dependent on δ, these results fall close to those determined by the FEM simulations described here for suitable choices of δ. It has been noted, however, that such small USL widths are unlikely in an experimental system, even in the presence of vigorous stirring regimes;

System	Flux (10^{-9} mol cm^2 s^{-1})
1	7.9 ± 0.3
2	0.9 ± 0.1
3	39 ± 4

Table 10.4: Fluxes measured experimentally by Gutknecht and Tosteson [5] for the systems simulated in this chapter.

Weak acid	P (10^{-4} cm s^{-1})
Acetic	66
Butanoic	950
Hexanoic	11000

Table 10.5: P values for a range of weak acids as measured experimentally by Walter and Gutknecht [6].

Gutknecht and Tosteson determined their USL width to be 130 μm. The flux for the buffered *cis* system (system 3 from Table 10.1) is not compatible with the results of the simulations presented here; it is too large to be explained by any of the USL widths used in the simulations.

The study of unbuffered weak acid permeation by Walter and Gutknecht [6] (Table 10.5) is in similar disagreement with the FEM results - even a heavily buffered system with δ as determined in their study (200 μm) is unable to accurately determine a P value of the magnitude suggested for butanoic and hexanoic acids. The systems used in [6] were much more weakly buffered than the simulations performed here (10 mM, as compared to 150 mM) with pH at 6.4 and 7.4, casting further doubt on the reliability of those values. Although no flux plateau is reached in the modelled system with a buffered *cis* region, it is apparent from Fig. 10.8 that values of $P \gg 600 \times 10^{-4}$ cm s^{-1} will not be distinguishable, and hence any such P values from unbuffered systems with $\delta \approx 200$ μm as in [6] should be treated with a certain caution.

Orbach and Finkelstein [101] measured the P value for butanoic acid to be 640×10^{-4} cm s^{-1}, in an unbuffered system of pH ≈ 5.6 with δ determined to be 100

μm; this result is also incompatible with the results of the FEM simulations presented here (see the onset of the flux plateau in Fig. 10.6 - this occurs at $P \approx 100 \times 10^{-4}$ cm s^{-1}, considerably before Orbach and Finkelstein's value, even with a lower bulk pH in the simulated system).

The recognition of the importance of the unstirred layer led Gutknecht and Tosteson [5] to suggested the following treatment of the experimental fluxes to determine P:

$$\frac{1}{J} = \frac{1}{P_{\mathsf{X}^-}^{\mathsf{USL}}[\mathsf{X}^-] + P_{\mathsf{HX}}^{\mathsf{USL}}[\mathsf{HX}]} + \frac{1}{P_{\mathsf{HX}}^{\mathsf{M}}[\mathsf{HX}]} \tag{10.1}$$

where $P_{\mathsf{XH}}^{\mathsf{USL}}$ and $P_{\mathsf{X}^-}^{\mathsf{USL}}$ are the permeation coefficients in the USL of the neutral and anionic weak acid species respectively, and $P_{\mathsf{HX}}^{\mathsf{USL}}$ is the permeation coefficient of the neutral weak acid in the BLM. The permeaion coefficients in the USL values are determined using

$$P_i^{\mathsf{USL}} = \frac{D_i}{\delta} \quad . \tag{10.2}$$

Equation 10.1 has been used in a number of studies (for example, [5–7]) to adjust for the presence of a USL in experimental systems. Using the models in Table 10.1, it is possible to test the predictions made by this formula using the results of the FEM simulations; Table 10.6 details the maximum fluxes measured in the FEM systems for the three selected values of δ, and the values of P which produce them. Also listed are the values of approximately half the maximum measured flux for each system and the values of P which produce them, as used in Figs. 10.10 and 10.11. This is intended to illustrate once again the differences between mass transport limited systems and those which are not mass transport limited.

Using Eqn. 10.1, and the known values of δ, P, D, flux and concentrations in the FEM simulations, it is possible to examine the reliability of the data produced by Eqn.

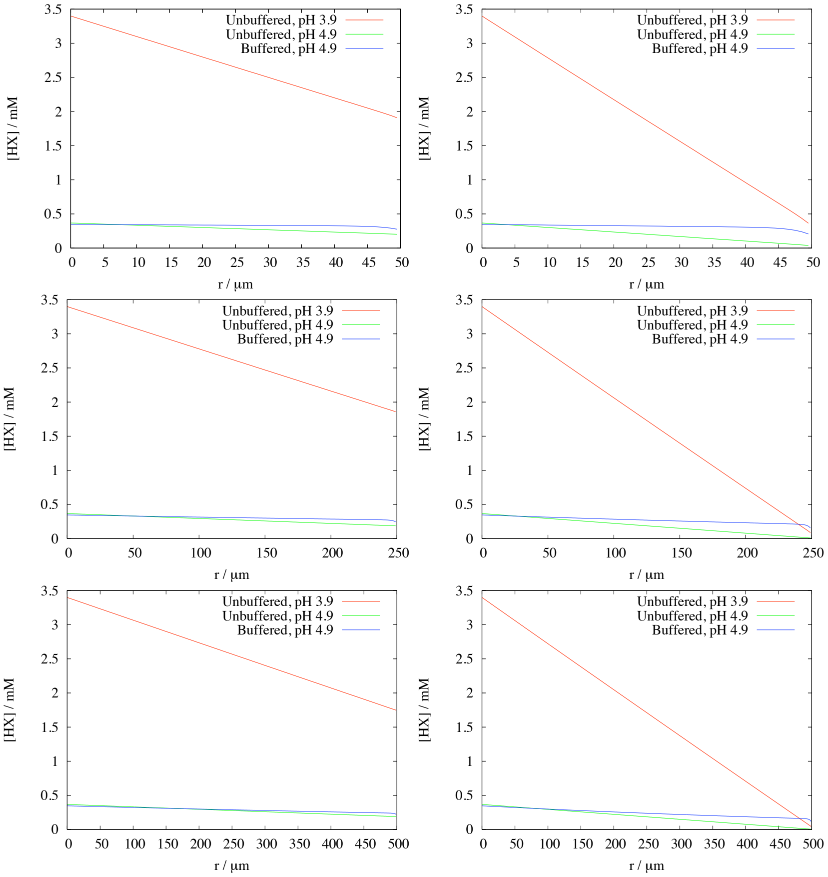

Figure 10.10: Left column; concentration profiles for the protonated weak acid carrier, HX, when P is set such that the BLM flux is half of the maximum flux achieved in the simulations. Right column; concentration profiles for protonated weak acid carrier where the largest simulated flux was attained. Rows from top to bottom; $\delta = 50$ μm, 250 μm and 500 μm.

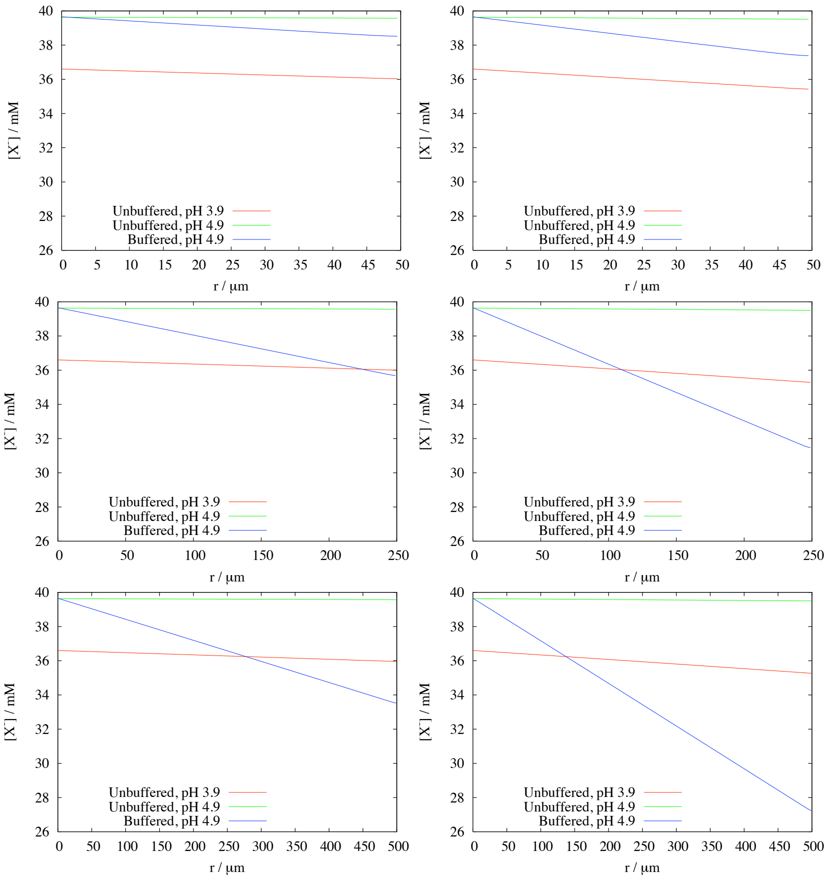

Figure 10.11: Left column; concentration profiles for the weak acid anion, [X$^-$], when P is set such that the BLM flux is half of the maximum flux achieved in the simulations. Right column; concentration profiles for protonated weak acid carrier where the largest simulated flux was attained. Rows from top to bottom; $\delta = 50$ μm, 250 μm and 500 μm.

		J$_{\text{max}}$		$\approx$ J$_{\text{max}}$/2	
System	δ / μm	Flux	$P \times 10^{-4}$	Flux	$P \times 10^{-4}$
1	50	8.2×10^{-9}	600	4.0×10^{-9}	22.0
	250	1.8×10^{-9}	600	8.9×10^{-10}	5.2
	500	9.0×10^{-10}	600	4.4×10^{-10}	2.5
2	50	8.7×10^{-10}	600	4.3×10^{-10}	22.0
	250	1.9×10^{-10}	600	9.5×10^{-11}	5.2
	500	9.5×10^{-11}	600	4.7×10^{-11}	2.5
3	50	4.7×10^{-9}	600	2.4×10^{-9}	114.5
	250	3.2×10^{-9}	600	1.6×10^{-9}	79.5
	500	2.4×10^{-9}	600	1.2×10^{-9}	66.2

Table 10.6: Maximum flux values (J$_{\text{max}}$) measured in the simulated systems (see Table 10.1), and the P values which produced them, along with approximately half the maximum measured flux values ($\approx$ J$_{\text{max}}$/2) and the P values which produced them. Data is given for the three values of δ discussed in this chapter. Units of flux are mol cm^{-2} s^{-1}, and units of P are cm s^{-1}.

10.1. The results are listed in Table 10.7. As can be seen, for systems which are mass transport limited (or approaching that state, in the case of the buffered *cis* systems) the predicted fluxes and permeation coefficients are incorrect, and quite strikingly so. This is due to the lack of a unique value for the flux for large P. In the systems where the flux is half of the maximum measured in simulation, and hence where the flux is *not* limited by mass transport in the bulk and USL, the predicted fluxes and P values are in good agreement with those measured in the FEM simulations.

10.4 Conclusion

Unbuffered experimental systems based on flux measurement between BLM-separated chambers were shown to be unreliable for anything other than small P values for experimentally relevant USL widths. Buffered systems provide quantitatively different behaviour, in terms of the variations of flux with P and δ, but still the flux will plateau for sufficiently large values of those parameters.

For the ranges of P and δ where such a plateau exists it becomes impossible

		$\mathsf{J}_{\mathsf{max}}$		$\approx \mathsf{J}_{\mathsf{max}}/2$	
System	δ / μm	Flux	$P \times 10^{-4}$	Flux	$P \times 10^{-4}$
1	50	1.7×10^{-8}	253	4.0×10^{-9}	22.1
	250	3.9×10^{-9}	233	7.9×10^{-10}	5.1
	500	2.0×10^{-9}	232	4.2×10^{-10}	2.7
2	50	2.2×10^{-9}	229	4.6×10^{-10}	21.4
	250	5.3×10^{-10}	209	9.6×10^{-11}	5.1
	500	2.7×10^{-10}	208	4.7×10^{-11}	2.5
3	50	1.1×10^{-8}	243	3.0×10^{-9}	93.7
	250	5.8×10^{-9}	258	1.7×10^{-9}	72.2
	500	3.7×10^{-9}	297	1.2×10^{-9}	65.0

Table 10.7: Values of flux and P predicted by Eqn. (10.1) for the data listed in Table 10.6. The predicted fluxes are generated from the known δ, D, P and concentrations in the simulated systems. The predicted P values follow a similar method, but instead use the fluxes as determined by the simulations. Units of flux are mol cm^{-2} s^{-1}, and units of P are cm s^{-1}.

to distinguish between values of P, and hence sufficiently large permeation coefficients (as suggested in previous studies [5, 6, 101]) simply cannot be measured directly. The LCSM/FEM method introduced in this thesis is one method to overcome such experimental limitations without relying on assumptions of USL width or buffering effects. One traditional formula to aid in the determination of P values from experimental fluxes (adjusting for the permeation in the USL) was shown to be unreliable for mass transport limited permeation processes, but to provide a good estimate in other cases - the major experimental problem remaining the identification of such systems where the formula is applicable.

Chapter 11

Conclusions and further work

This thesis has detailed the application of a variety of experimental and theoretical methods to the study of passive permeation in models of biological membranes. Chapter 7 applied a FEM to the parameterisation of oxygen permeation in a variety of monolayers, and the excellent agreement between the experimental and simulated approach curves demonstrated the reliability of this approach to determining first order rate constants for the process. The MD studies were less successful; the excess free energy barriers suggested are not compatible with the experimental data. Simulations under a different ensemble, such as a constant surface tension prescription, and longer simulation times may help to alleviate these discrepancies.

The most important aspects of the thesis are detailed in Chapters 8 and 9, specifically a novel LCSM/FEM method to determine the permeation coefficients of protonophores, and the results illustrate a trend which is quite opposed to the conventional wisdom, casting the long-established Overton's rule [123, 124] into doubt. The trend of decreasing P with increasing size in a series of homologous weak acids was shown in three separate BLM systems, contradicting a number of earlier studies

[6, 7, 107] and overcoming many limitations in traditional experiments. This method has potentially important applications in pharmacology, as many pharmaceutically important compounds are weak acids or bases, but could be fruitfully applied to many systems where the presence of a specific molecule can be detected using fluorescent dyes. One potential weakness remains in the method - the structure of the BLMs used. Although the confocal microscope allows easy verification of the presence of a BLM, and the lack of bubbles etc therein, the stability of the BLM may cause experimental problems which could be solved with the capillary BLM formation of Henry White and co-workers [152], with the added benefit of the ability to study permeation through ion channels, although even with more advanced methods the question of controlling the surface tension (and hence the lateral and normal pressures) in the BLM remain.

MD studies of excess free energy in the POPC bilayer systems proved difficult to achieve; the simulation techniques used in this study should produce more positive results with a more intelligent choice of ensemble and greater simulation times.

Chapter 10 regards the theoretical limits of previous experimental studies intended to measure P values. Through the use of a series of FEM simulations, it was shown that only a limited range of relatively small P values can be discerned from flux measurements; for experimentally relevant widths of the USL, weakly buffered systems can quickly become limited by mass transport in the bulk and USL itself, and hence an experimentally measured flux cannot adequately imply the correct P due to the lack of a unique flux over a wide range of P. One common formula for adjusting for the presence of a USL in experimental studies [5] was demonstrated to be unreliable in mass transport limited systems, despite its apparent success in other cases. This casts doubt on the ability of traditional experimental methods to determine P for a wide range of substances - a weakness which is not as prevalent in the novel LCSM/FEM method we introduce here, due to the very small and well-defined USL widths.

Bibliography

[1] Vladimir M. Kaganer, Helmuth Mohwald, and Pulak Dutta. Structure and Phase Transitions in Langmuir Monolayers. *Reviews of Modern Physics*, 71:779–814, 1999.

[2] Ilenia Ciani, David P. Burt, Salvatore Danielli, and Patrick R. Unwin. Effect of Surface Pressure on Oxygen Transfer Across Molecular Monolayers at the Air/Water Interface: Scanning Electrochemical Microscopy Investigations using a Mercury Hemispherical Microelectrode Probe. *Journal of Physical Chemistry B*, 108:3801–3809, 2004.

[3] L. Stryer. *Biochemistry*. W. H. Freeman and Company, New York, 1995.

[4] H. T. Tien. *Bilayer Lipid Membranes (BLMs): Theory and Practise*. Marcel Dekker, 1974.

[5] John Gutknecht and D. C. Tosteson. Diffusion of Weak Acids Across Lipid Bilayer Membranes: Effects of Chemical Reactions in the Unstirred Layers. *Science*, 182: 1258–1261, 1973.

[6] Anne Walter and John Gutknecht. Monocarboxylic Acid Permeation through Lipid Bilayer Membranes. *Journal of Membrane Biology*, 77:255–264, 1984.

[7] Anne Walter and John Gutknecht. Permeability of Small Nonelectrolytes through Lipid Bilayer Membranes. *Journal of Membrane Biology*, 90:207–217, 1986.

[8] Benjamin. A. Suarez-Isla, Kee Wan, Jon Lindstrom, and Mauricio Montal. Single-Channel Recordings from Purified Acetylcholine Receptors Reconstituted in Bilayers Formed at the Tip of Patch Pipets. 22:2319–2323, 1983.

[9] Paul Mueller, Donald O. Rudin, H. Ti Tien, and William C. Wescott. Methods for the Formation of Single Bimolecular Lipid Membranes in Aqueous Solution. *Journal of Physical Chemistry*, 67:534–535, 1963.

[10] William Gilbert, Paul Fleury Mottelay, and Edward Wright. *De Magnete*. Courier Dover Publications, 1958.

[11] Charles Francois de Cisternay Du Fey. A Discourse Concerning Electricity. *Philosophical Transactions of the Royal Society of London*, 38:258–266, 1733.

[12] Joseph Priesley. *The History and Present State of Electricity, with Original Experiments*. J. Dodsley and J. Johnson and J. Payne and T. Cadell, 1767.

[13] C. A. Coulomb. *Collection de Memoires Relatifs a la Physique Vol I*. Societe Francaise de Physique, Paris, 1884.

[14] Alessandro Giuseppe Antonio Anastasio Volta. Mmoire Sur Lélectricité Excitée Par Le Contact Mutuel Des Conducteurs Même Les Plus Parfaits. *Philosophical Transactions of the Royal Society of London*, 90:403–431, 1800.

[15] A. J. Bard and L. R. Faulkner. *Electrochemical Methods: Fundamentals and Applications*. John Wiley and Sons, Inc, 2001.

[16] Eleni Bitziou, Nicola C. Rudd, MArtin A. Edwards, and Patrick R. Unwin. Visualization and Modeling of the Hydrodynamics of an Impinging Microjet. *Analytical Chemistry*, 78:1435–1443, 2006.

[17] A. C. Fisher. *Electrode Dynamics*. Oxford University Press, 2003.

[18] M. A. Edwards, S. Martin, A. L. Whitworth, J. V. Macpherson, and P. R. Unwin. Scanning Electrochemical Microscopy: Principles and Applications to Biophysical Systems. *Physiological Measurements*, 27:R63–R108, 2006.

[19] H. Y. Liu, F.-R. Fan, W. C. Lin, and A. J. Bard. Scanning Electrochemical and Tunneling Ultramicroelectrode Microscope for High-Resolution Examination of Electrode Surfaces in Solution. *Journal of the American Chemical Society*, 108: 3838–3839, 1986.

[20] C. Kranz, M. Ludwig, H. E. Gaub, and W. Schuhmann. Lateral Deposition of Polypyrrole Lines by the Scanning Electrochemical Microscope. *Advanced Materials*, 7:38–40, 1995.

[21] P. Hliva, I. Kapui, and L. Czako. Amperometric Bacterial Electrode for the Selective Determination of Ammonium Ion Concentration. *Magyar Kemiai Folyoirat*, 104:224–231, 1998.

[22] R. D. Martin and P. R. Unwin. Scanning Electrochemical Microscopy: Theory and Experiment for the Positive Feedback Mode with Unequal Diffusion Coefficients of the Redox Mediator Couple. *Journal of Electroanalytical Chemistry*, 439:123–136, 1997.

[23] R. D. Martin and P. R. Unwin. Theory and Experiment for the Substrate Generation/Tip Collection Mode of the Scanning Electrochemical Microscope: Appli-

cation as an Approach for Measuring the Diffusion Coefficient Ratio of a Redox Couple. *Analytical Chemistry*, 70:276–284, 1998.

[24] Janine Mauzeroll and Allen J. Bard. Scanning Electrochemical Microscopy of Menadione-Glutathione Conjugate Export from Yeast Cells. *Proceedings of the National Academy of Sciences of the United States of America*, 101:7862–7867, 2004.

[25] Christopher J. Slevin, J. V. Macpherson, and P. R. Unwin. Measurement of Local Reactivity at Liquid/Solid, Liquid/Liquid and Liquid/Gas Interfaces with the Scanning Electrochemical Microscope: Principles, Theory and Applications of the Double Potential Step Chronoamperometric Mode. *Journal of Physical Chemistry B*, 101:10851–10859, 1997.

[26] J. V. Macpherson and Patrick R. Unwin. Scanning Electrochemical Microscope Induced Dissolution: Rate Law and Reaction Rate Imaging for Dissolution of the (010) Face of Potassium Ferrocyanide Trihydrate in Nonstoichiometric Aqueous Solutions of the Lattice Ions. *Journal of Physical Chemistry*, 99:3338–3351, 1995.

[27] G. Cox. Biological Confocal Microscopy. *Materials Today*, 5:34–41, 2002.

[28] Marvin Minsky. Memoir on Inventing the Confocal Scanning Microscope. *Scanning*, 10:128–138, 1988.

[29] Nicola C. Rudd, Susan Cannan, Eleni Bitziou, Ilenia Ciani, Anna L. Whitworth, and Patrick R. Unwin. Fluorescence Confocal Laser Scanning Microscopy as a Probe of pH Gradients in Electrode Reactions and Surface Activity. *Analytical Chemistry*, 77:6205–6217, 2005.

[30] Rajesh Sekar and Ammasi Periasamy. Fluorescence Resonance Energy Transfer (FRET) Microscopy Imaging of Live Cell Localizations. *Journal of Cell Biology*, 160:629–633, 2003.

[31] James Newton Butler and David R. Cogley. *Ionic Equilibrium: Solubility and pH Calculations*. Wiley-Interscience, 1998.

[32] Harvey Diehl and Richard Markuszewski. Studies on Fluorescein II: the Solubility and Acid Dissociation Constants of Fluorescein in Water Solution. *Talanta*, 32: 159–165, 1985.

[33] Colin Sheppard and D. Shotton. *Confocal Laser Scanning Microscopy*. Garland Publishing, 1997.

[34] K. V. Chau and J. J. Gaffney. A Finite-Difference Model for Heat and Mass Transfer in Products with Internal Heat Generation and Transpiration. *Journal of Food Science*, 55:484–487, 1990.

[35] V. M. Soundalgekar and S. B.Hiremath. Finite-Difference Analysis of Mass Transfer Effects on Flow Past an Impulsively Started Infinite Isothermal Vertical Plate in Dissipative Fluid. *Astrophysics and Space Science*, 95:163–173, 1983.

[36] R. Voituriez, M. Moreau, and G. Oshanin. Reversible Diffusion-Limited Reactions: "Chemical Equilibrium" State and the Law of Mass Action Revisited. *Europhysics Letters*, 69:177–183, 2005.

[37] N. Sanaie and charles A. Haynes. A Multiple Chemical Equilibria Approach to Modeling and Interpreting the Separation of Amino Acid Enantiomers by Chiral Ligand-Exchange Chromatography. *Journal of Chromatography A*, 1132:39–50, 2006.

[38] William B. J. Zimmerman. *Process Modelling and Simulation with Finite Element Methods*. W. H. Freeman and Company, New York, 2004.

[39] O. K. Rice. On the Statistical Mechanics of Liquids, and the Gas of Hard Spheres. *Journal of Chemical Physics*, 12:1–18, 1943.

[40] J. D. Bernal. The Bakerian Lecture, 1962. *The Proceedings of the Royal Society of London Series A*, 1962.

[41] Nicholas Metropolis, Arianna W. Rosenbluth, Marshall N. Rosenbluth, Augusta H. Teller, and Edward Teller. Equation of State Calculations by Fast Computing Machines. *Journal of Chemical Physics*, 21:1087–1092, 1953.

[42] Bernard R. Brooks, Robert E. Bruccoleri, Barry D. Olafson, David J. States, S. Swaminathan, and Martin Karplus. CHARMM: a Program for Macromolecular Energy, Minimization, and Dynamics Calculations. *Journal of Computational Chemistry*, 4:187–217, 1983.

[43] Herbert Goldstein. *Classical Mechanics*. Addison-Wesley, 1964.

[44] J. E. Lennard-Jones. Cohesion. *The Proceedings of the Physical Society*, 43: 461–482, 1931.

[45] M. P. Allen and D. J. Tildesley. *Computer Simulation of Liquids*. Oxford University Press, 1987.

[46] Jean-Paul Ryckaert, Giovanni Ciccotti, and Herman J. C. Berendsen. Numerical Integration of the Cartesian Equations of Motion of a System with Constraints: Molecular Dynamics of N-Alkanes. *Journal of Computational Physics*, 23:327–341, 1977.

[47] W. C. Swope, H. C. Andersen, P. H. Berens, and K. R. Wilson. A Computer Simulation Method for the Calculation of Equilibrium Constants for the Formation of Physical Clusters of Molecules: Application to Small Water Clusters. *Journal of Chemical Physics*, 76:637–649, 1982.

[48] P. Ewald. Die Berechnung Optischer und Elektrostatischer Gitterpotentiale. *Annalen der Physik*, 64:253–287, 1921.

[49] H. J. C. Berendsen, J. P. M. Postma, W. F. van Gunsteren, A. DiNola, and J. R. Haak. Molecular Dynamics with Coupling to an External Bath. *Journal of Chemical Physics*, 81:3684–3690, 1984.

[50] H. C. Andersen. Molecular Dynamics at Constant Pressure and/or Temperature. *Journal of Chemical Physics*, 72:2384–2393, 1980.

[51] Daan Frenkel and Berend Smit. *Understanding Molecular Simulation: from Algorithms to Applications*. Academic Press, London, 2002.

[52] S. Nosé. A Unified Formulation of the Constant Temperature Molecular Dynamics Method. *Journal of Chemical Physics*, 81:511–519, 1984.

[53] W. G. Hoover. Canonical Dynamics: Equilibrium Phase-Space Distributions. *Physical Review A*, 31:1695–1697, 1985.

[54] G. M. Torrie and J. P. Valleau. Nonphysical Sampling Distributions in Monte Carlo Free-Energy Estimation: Umbrella Sampling. *Journal of Computational Physics*, 23:187–199, 1977.

[55] S. Kumar, D. Bouzida, R. H. Swensdon, P. A. Kollman, and J. M. Rosenberg. The Weighted Histogram Analysis Method for Free-Energy Calculations

on Biomolecules. I. the Method. *Journal of Computational Chemistry*, 13:1011–1021, 1992.

[56] W. D. Stein and W. R. Lieb. *Transport and Diffusion Across Cell Membranes*, pages 69–112. Academic Press, 1986.

[57] Thorsten Hartmann and Johannes Schmitt. Lipophilicity - Beyond Ocanol/Water: a Short Comparison of Modern Technologies. *Drug Discovery Today*, 1:431–439, 2004.

[58] Lynn Collins-Gold, Norbert Feichtinger, and Torbjorn Warnheim. Lipophilic Compounds have Great Potential in the Discovery Process. *Modern Drug Discovery*, 3:44–46, 2000.

[59] Eric. K. Rideal. The Calculation of the Potential of Mean Force using Computer Simulations. *Journal of Physical Chemistry*, 29:1585–1588, 1925.

[60] Xun Yan, Vaclav Janout, James T. Hsu, and Steven L. Regen. A Polymerized Calix[6]arene Monolayer Having Gas Permeation Selectivity That Exceeds Knudsen Diffusion. *Journal of the American Chemical Society*, 124:10962–10963, 2002.

[61] Junwei Li, Vaclav Janout, Donald H. McCullough 3rd, James T. Hsu, Quoc Truong, Eugene Wilusz, and Steven L. Regen. Exceptional Gas Permeation Selectivity of a Glued Langmuir-Blodgett Bilayer by pH Control. *Langmuir*, 20: 8214–8219, 2004.

[62] Catherine Venien-Bryan, Pierre-Francois Lenne, Cecile Zakri, Anne Renault, Alain Brisson, Jean-Francois Legrand, and Bruno Berge. Characterization of the Growth of 2d Protein Crystals on a Lipid Monolayer by Ellipsometry and Rigidity Mea-

surements Coupled to Electron Microscopy. *Biophysical Journal*, 74:2649–2657, 1998.

[63] Stefan Malcharek, Andreas Hinz, Lutz Hilterhaus, and Hans-Joachim Galla. Multilayer Structures in Lipid Monolayer Films Containing Surfactant Protein C: Effects of Cholesterol and Pope. *Biophysical Journal*, 88:2638–2649, 2005.

[64] Christopher J. Slevin, Steve Ryey, David J. Walton, and Patrick R. Unwin. A New Approach for Measuring the Effect of a Monolayer on Molecular Transfer Across an Air/Water Interface using Scanning Electrochemical Microscopy. *Langmuir*, 14:5331–5334, 1998.

[65] Susan Cannan, Jie Zhang, Frank Grunfield, and Patrick R. Unwin. Scanning Electrochemical Microscopy (SECM) Studies of Oxygen Transfer Across Phospholipid Monolayers Under Surface Pressure Control: Comparison of Monolayers at Air/Water and Oil/Water Interfaces. *Langmuir*, 20:701–707, 2004.

[66] S. Feller and A. D. MacKerell Jr. An Improved Empirical Potential Energy Function for Molecular Simulations of Phospholipids. *Journal of Physical Chemistry B*, 104:7510–7515, 2000.

[67] J. Vrabec, J. Stall, and H. Hasse. Molecular Models of Unlike Interactions in Fluid Mixtures. *Molecular Simulation*, 31:215–221, 2005.

[68] A. L. Galbrith and C. K. Hall. Vapor-Liquid Phase Equilibria for Mixtures Containing Diatomic Lennard-Jones Molecules. *Fluid Phase Equilibria*, 241:175–185, 2006.

[69] S. W. Chiu, Eric Jakobsson, Shankar Subramaniam, and H. Larry Scott. Combined Monte Carlo and Molecular Dynamics Simulation of Fully Hydrated Dioleyl and

Palmitoyl-Oleyl Phosphatidylcholine Lipid Bilayers. *Biophysical Journal*, 77:2462–2469, 1999.

[70] W. Smith, C. W. Yong, and P. M. Rodger. DL_POLY: Applications to Molecular Simulation. *Molecular Simulation*, 28:385–471, 2002.

[71] Benoit Roux. The Calculation of the Potential of Mean Force using Computer Simulations. *Computer Physics Communications*, 91:275–282, 1995.

[72] Izumi Kubo, Seiichi Adachi, Hidekatsu Maeda, and Atsushi Seki. Phosphatidylcholine Monolayers Observed with Brewster Angle Microscopy and Pi-A Isotherms. *Thin Solid Films*, 393:80–85, 2001.

[73] Alexandre Arnold, Isabelle Cloutier, Anna M. Ritcey, and Michele Auger. Temperature and Pressure Dependent Growth and Morphology of DMPC/DSPC Domains Studied by Brewster Angle Microscopy. *Chemistry and Physics of Lipids*, 133: 165–179, 2005.

[74] A. Bondi. Van der Waals Volumes and Radii. *Journal of Physical Chemistry*, 68: 441–451, 1964.

[75] D. R. Lide, editor. *Crc Handbook of Chemistry and Physics, Internet Version 2007*. Taylor and Francis, 87 edition, 2007.

[76] Shouzhong Zou, J. Spencer Baskin, and Ahmed H. Zewail. Molecular Recognition of Oxygen by Protein Mimics: Dynamics on the Femtosecond to Microsecond Time Scale. *Proceedings of the National Academy of Sciences of the United States of America*, 99:9625–9630, 2002.

[77] Annika Malkia, Peter Liljeroth, and Kyosti Kontturi. Drug Transfer through

Biomimetic Langmuir-Blodgett Monolayers at a Liquid-Liquid Interface. *Analytical Sciences*, 17:345–348, 2001.

[78] Tzung-Han Chou, I-Ming Chu, and Chien-Hsiang Chang. Interaction of Paclitaxel with DSPC in Monolayers at the Air/Water Interface at Different Temperatures. *Colloids and Surfaces B: Biointerfaces*, 25:147–155, 2002.

[79] Erik Lindahl and Olle Edholm. Mesoscopic Undulations and Thickness Fluctuations in Lipid Bilayers from Molecular Dynamics Simulations. *Biophysical Journal*, 79:426–433, 2000.

[80] S. J. Marrink and A. E. Mark. Effect of Undulations on Surface Tension in Simulated Bilayers. *Journal of Physical Chemistry B*, 105:6122–6127, 2001.

[81] Feng Sun. Constant Normal Pressure, Constant Surface Tension, and Constant Temperature Molecular Dynamics Simulation of Hydrated 1,2-Dilignoceroylphosphatidylcholine Monolayer. *Biophysical Journal*, 82:2511–2519, 2002.

[82] Jose Alejandre, Dominic J. Tildesley, and Gustavo A. Chapela. Fluid Phase Equilibria using Molecular Dynamics: the Surface Tension of Chlorine and Hexane. *Molecular Physics*, 85:651–663, 1995.

[83] Jose Alejandre, Dominic J. Tildesley, and Gustavo A. Chapela. Molecular Dynamics Simulation of the Orthobaric Densities and Surface Tension of Water. *Journal of Chemical Physics*, 102:4574–4583, 1995.

[84] Elizabeth A. Dolan, Richard M. Venable, Richard W. Pastor, and Bernard R. Brooks. Simulations of Membranes and Other Interfacial Systems using P21 and PC Periodic Boundary Conditions. *Biophysical Journal*, 82:2317–2325, 2002.

[85] Harden McConnell and Arun Radhakrishnan. Theory of the Deuterium NMR of Sterol-Phospholipid Membranes. *Proceedings of the National Academy of Sciences of the United States of America*, 103:1184–1189, 2005.

[86] Richard W. Pastor, Richard M. Venable, and Martin Karplus. Model for the Structure of the Lipid Bilayer. *Proceedings of the National Academy of Sciences of the United States of America*, 88:892–896, 1991.

[87] J. Lyklema and H. P. Leeuwen. *Fundamentals of Interface and Colloid Science*. Morgan Kauffman, 1962.

[88] Bruce Alberts, Alexander Johnson, Julian Lewis, Martin Raff, Keith Roberts, and Peter Walter. *Molecular Biology of the Cell*, chapter 10. Garland Science, 2002.

[89] Bruce Alberts, Alexander Johnson, Julian Lewis, Martin Raff, Keith Roberts, and Peter Walter. *Molecular Biology of the Cell*, chapter 14. Garland Science, 2002.

[90] F. D. Gunstone, J. L. Harwood, and F. B. Padley. *The Lipid Handbook*. Chapman and Hall, 1986.

[91] Bruce Alberts, Alexander Johnson, Julian Lewis, Martin Raff, Keith Roberts, and Peter Walter. *Molecular Biology of the Cell*, page 589. Garland Science, 2002.

[92] Bruce Alberts, Alexander Johnson, Julian Lewis, Martin Raff, Keith Roberts, and Peter Walter. *Molecular Biology of the Cell*, page 589. Garland Science, 2002.

[93] Yuri N. Antonenko, Peter Pohl, and Gennady A. Denisov. Permeation of Ammonia Across Bilayer Lipid Membranes Studied by Ammonium Ion Selective Microelectrodes. *Biophysical Journal*, 72:2187–2195, 1997.

[94] Tian-Xiang Xiang and Bradley D. Anderson. Phospholipid Surface Density Determines the Partitioning and Permeability of Acetic Acid in DMPC:Cholesterol Bilayers. *Journal of Membrane Biology*, 148:157–167, 1995.

[95] Tian-Xiang Xiang and Bradley D. Anderson. Permeability of Acetic Acid Across Gel and Liquid-Crystalline Lipid Bilayers Conforms to Free-Surface-Area Theory. *Biophysical Journal*, 72:223–237, 1997.

[96] J. R. Alger and J. H. Prestegard. Nuclear Magnetic Resonance Study of Acetic Acid Permeation of Large Unilamellar Vesicle Membranes. *Biophysical Journal*, 28:1–14, 1979.

[97] Yuri N. Antonenko and Alexander A. Bulychev. Measurements of Local pH Changes Near Bilayer Lipid Membrane by Means of a pH Microelectrode and a Protonophore-Dependent Membrane Potential. Comparison of the Methods. *Biochimica et Biophysica Acta*, 1070:279–282, 1991.

[98] Yuri N. Antonenko and Peter Pohl. Steady-State Nonmonotonic Concentration Profiles of Bilayer Lipid Membranes in the Unstirred Layers. *Biochimica et Biophysica Acta*, 1235:57–61, 1995.

[99] Veronika Yu. Evtodienko, Olga N. Kovbasnjuk, Yuri N. Antonenko, and Lev S. Yaguzhinsky. Effect of the Alkyl Chain Length of Monocarboxylic Acid on the Permeation through Bilayer Lipid Membranes. *Biochimica et Biophysica Acta*, 1281:245–251, 1996.

[100] Andrey V. Krylov, Peter Pohl, Mark L. Zeidel, and Warren G. Hill. Water Permeability of Asymmetric Planar Lipid Bilayers: Leaflets of Different Composition

Offer Independent and Additive Resistances to Permeation. *Journal of General Physiology*, 118:333–340, 2001.

[101] Eli Orbach and Alan Finkelstein. The Nonelectrolyte Permeability of Planar Lipid Bilayer Membranes. *Journal of General Physiology*, 75:427–436, 1980.

[102] Peter Pohl, Sapar M. Saparov, and Yuri N. Antonenko. The Effect of a Transmembrane Osmotic Flux on the Ion Concentraion Distribution in the Immediate Membrane Vicinity Measured by Microelectrodes. *Biophysical Journal*, 72:1711–1718, 1997.

[103] Peter Pohl, Sapar M. Saparov, and Yuri N. Antonenko. The Size of the Unstirred Layer as a Function of the Solute Diffusion Coefficient. *Biophysical Journal*, 75: 1403–1409, 1998.

[104] Anit V. Thomae, Heidi Wunderli-Allenspach, and Stefanie D. Kramer. Permeation of Aromatic Carboxylic Acids Across Lipid Bilayers: the pH-Partition Hypothesis Revisited. *Biophysical Journal*, 89:1802–1811, 2005.

[105] Michael Tsionsky, Junfeng Zhou, Shigura Amemiya, Fu-Ren F. Fan, and Allen J. Bard. Scanning Electrochemical Microscopy. 38. Application of SECM to the Study of Charge Transfer through Bilayer Lipid Membranes. *Analytical Chemistry*, 71:4300–4305, 1999.

[106] Anne Walter, David Hastings, and John Gutknecht. Weak Acid Permeability through Lipid Bilayer Membranes. *Journal of General Physiology*, 79:917–933, 1982.

[107] J. M. Wolosin and Hagai Ginsburg. The Permeation of Organic Acids through

Lecithin Bilayers Resemblance to Diffusion in Polymers. *Biochimica et Biophysica Acta*, 389:20–33, 1975.

[108] Sharman D. O'Neill and A. Carl Leopold. An Assessment of Phase Transitions in Soybean Membranes. *Plant Physiology*, 70:1405–1409, 1982.

[109] R. B. Gennis. *Biomembranes*, pages 235–322. Springer, 1989.

[110] Kely M. Mahar Doan, Joan E. Humphreys, Lindsey O. Webster, Stephen A. Wring, Larry J. Shampine, Coette J. Serabjit-Singh, Kimberly K. Adkison, and Joseph W. Polli. Passive Permeability and P-Glycoprotein-Mediated Efflux Differentiate Central Nervous System (CNS) and Non-CNS Marketed Drugs. *Journal of Pharmacology and Experimental Therapeutics*, 303:1029–1037, 2002.

[111] Stephan Doppenschmitt, Hildegard Spahn-Langguth, Carl Gunner Regardh, and Peter Langguth. Role of P-Glycoprotein-Mediated Secretion in Absorptive Drug Permeability: an Approach using Passive Membrane Permeability and Affinity to P-Glycoprotein. *Journal of Pharmaceutical Sciences*, 88:1067–1072, 1999.

[112] Sapar M. Saparov, Yuri N. Antonenko, and Peter Pohl. A New Model of Weak Acid Permeation through Membranes Revisited: Does Overton Still Rule? *Biophysical Journal*, page L88, 2006.

[113] A D Sen, V G Anicich, and T Arakelian. Dielectric Constant of Liquid Alkanes and Hydrocarbon Mixtures. *Journal of Physics D: Applied Physics*, 25:516–521, 1992.

[114] David W Deamer and J Wylie Nichols. Proton Flux Mechanisms in Model and Biological Membranes. *Journal of Membrane Biology*, 107:91–103, 1989.

[115] Donald Cairns. *Essentials of Pharmaceutical Chemistry*. Pharmaceutical Press, 2003.

[116] E. Gottlieb, S. M. Armour, M. H. Harris, and C. B. Thompson. Mitochondrial Membrane Potential Regulates Matrix Configuration and Cytochrome C Release During Apoptosis. *Nature Cell Death and Differentiation*, 10:709–717, 2003.

[117] Hideo Yamasaki, Shigeki Furuya, Akira Kawamura, Akio Ito, Shigeki Okayama, and Mitsuo Nishimura. Induction of the H+ Release from Thylakoid Membranes by Illumination in the Presence of Protonophores at High Concentrations. *Plant Cell Physiology*, 32:925–934, 1991.

[118] Tian-Xiang Xiang and Bradley D. Anderson. Permeability of Acetic Acid Across Gel and Liquid-Crystalline Lipid Bilayers Conforms to Free-Surface-Area Theory. *Biophysical Journal*, 75:2658–2671, 1998.

[119] Hiroshi Yamada, Tomokazu Matsue, and Isamu Uchida. A Microvoltammetric Study of Permeation of Ferrocene Derivatives through a Planer Bilayer Lipid Membrane. *Biochimica et Biophysica Acta*, 180:1330–1334, 1991.

[120] Tomokazu Matsue, Hitoshi Shiku, Hiroshi Yamada, and Isamu Uchida. Permselectivity of Voltage-Gated Ion Channel Studied by Microamperometry. *Journal of Physical Chemistry*, 98:11001–11003, 1994.

[121] Marylou Gonsalves, Anna L. Barker, Julie V. Macpherson, Patrick R. Unwin, Danny O'Hare, and C. Peter Winlove. Scanning Electrochemical Microscopy as a Local Probe of Oxygen Permeability in Cartilage. *Biophysical Journal*, 78:1578–1588, 2000.

[122] Erik R. Scott and Henry S. White. Scanning Electrochemical Microscopy of a Porous Membrane. *Journal of Membrane Science*, 58:71–87, 1991.

[123] Chalres Ernest Overton. *Studien Uber Die Narkose*. Fischer, Jena, 1901.

[124] C. E. Overton. *Studies in Narcosis*. Chapman and Hall, 1991.

[125] R. M. Wightman and D. O. Wipf. *Electroanalytical Chemistry Vol. 15*. Marcel Dekker, 1989.

[126] R. H. Bartels, J. C. Beatty, and B. A. Barsky. *Ion Association*. Morgan Kauffman, 1962.

[127] C. W. Davies. *An Introduction to Splines for use in Computer Graphics and Geometric Modelling*. Butterworths, 1989.

[128] D. M. Miller. Evidence That Interfacial Transport is Rate-Limiting During Passive Cell Membrane Permeation. *Biochimica et Biophysica Acta*, 1065:75–81, 1991.

[129] H Raghuraman and Amitabha Chattopadhyay. Influence of Lipid Chain Unsaturation on Membrane-Bound Melittin: a Fluorescence Approach. *Biochimica et Biophysica Acta*, 1665:29–39, 2004.

[130] Holger S. Scheidt, Alexander Vogel, Andreas Eckhoff, Bernd W. Koenig, and Daniel Hunster. Solid-State NMR Characterization of the Putative Membrane Anchor of Twd1 from Arabidopsis Thaliana. 36:393–404, 2007.

[131] Thomas Huber, Ana V. Botelho, Klaus Beyer, and Michael F. Brown. Membrane Model for the G-Protein-Coupled Receptor Rhodopsin: Hydrophobic Interface and Dynamical Structure. *Biophysical Journal*, 86:2078–2100, 2004.

[132] Heedeok Hong and Lukas K. Tamm. Elastic Coupling of Integral Membrane Protein Stability to Lipid Bilayer Forces. *Proceedings of the National Academy of Sciences of the United States of America*, 101:4065–4070, 2004.

[133] Hyunbum Jang, Buyong Ma, Thomas B. Woolf, and Ruth Nussinov. Interaction of Protegrin-1 with Lipid Bilayers: Membrane Thinning Effect. *Biophysical Journal*, 91:2848–1859, 2006.

[134] Monica L. Frazier, Jenny R. Wright, Antje Pokorny, , and Paulo F. F. Almeida. Investigation of Domain Formation in Sphingomyelin/Cholesterol/POPC Mixtures by Fluorescence Resonance Energy Transfer and Monte Carlo Simulations. *Biophysical Journal*, 92:2422–2433, 2007.

[135] Rebekah H. Gensure, Mark L. Zeidel, and Warren G. Hill. Lipid Raft Components Cholesterol and Sphingomyelin Increase H+/OH- Permeability of Phosphatidylcholine Membranes. *Biochemical Journal*, 398:485–495, 2006.

[136] Oscar Domenech, Sandra Merino-Montero, M. Teresa Montero, and Jordi Hernandez-Borrell. Surface Planar Bilayers of Phospholipids Used in Protein Membrane Reconstitution: an Atomic Force Microscopy Study. *Colloids and Surfaces B: Biointerfaces*, 47:102–106, 2006.

[137] Duane A. Redfern and Arne Gericke. Domain Formation in Phosphatidylinositol Monophosphate/Phosphatidylcholine Mixed Vesicles. *Biophysical Journal*, 86: 2980–2992, 2004.

[138] Derek Marsh. Polarity and Permeation Profiles in Lipid Membranes. *Proceedings of the National Academy of Sciences of the United States of America*, 98:7777–7782, 2002.

[139] Gerhard Schwarz, Rui ting Zong, and Teodor Popescu. Kinetics of Melittin Induced Pore Formation in the Membrane of Lipid Vesicles. *Biochimica et Biophysica Acta*, 1110:97–104, 1992.

[140] Aden Hodzic, Michael Rappolt, Heinz Amenitsch, Peter Laggner, and Georg Pabst. Differential Modulation of Membrane Structure and Fluctuations by Plant Sterols and Cholesterol. *Biophysical Journal*, 94:3935–3944, 2008.

[141] W.W. Sukowskia, D. Pentaka, K. Nowaka, and A. Sukowska. The Inuence of Temperature, Cholesterol Content and pH on Liposome Stability. *Journal of Molecular Structure*, 744.

[142] Ole G. Mouritsen and Martin J. Zuckermann. What's So Special About Cholesterol? *Lipids*, 39:1101–1113, 2004.

[143] Omar Bakht, Priyadarshini Pathak, and Erwin London. Effect of the Structure of Lipids Favoring Disordered Domain Formation on the Stability of Cholesterol-Containing Ordered Domains (Lipid Rafts): Identication of Multiple Raft-Stabilization Mechanisms. *Biophysical Journal*, 93:4307–4318, 2007.

[144] Andrey Filippov, Greger Oradd, and Goran Lindblom. Sphingomyelin Structure Inuences the Lateral Diffusion and Raft Formation in Lipid Bilayers. *Biophysical Journal*, 90:2086–2092, 2006.

[145] W. Humphrey, A. Dalke, and K. Schulten. VMD - Visual Molecular Dynamics. 14:33–38, 1996.

[146] Marja T. Hyvonen and Petri T. Kovanen. Molecular Dynamics Simulations of Unsaturated Lipid Bilayers: Effects of Varying the Numbers of Double Bonds. 34: 294–305, 2005.

[147] Pawe Weronski, Yi Jiang, and Steen Rasmussen. Molecular Dynamics Study of Small PNA Molecules in Lipid-Water System. *Biophysical Journal*, 92:3081–3091, 2007.

[148] Justin Gullingsrud and Klaus Schultern. Lipid Bilayer Pressure Proles and Mechanosensitive Channel Gating. *Biophysical Journal*, 86:3496–3509, 2004.

[149] G. Lantzsch, H. Binder, and H. Heerklotz. Surface Area Per Molecule in Lipid/C12e. Membranes as Seen by Fluorescence Resonance Energy Transfer. *Journal of Fluorescence*, 4:339–343, 1994.

[150] B. Konig, U. Dietrich, and G. Klose. Hydration and Structural Properties of Mixed Lipid/ Surfactant Model Membranes. *Langmuir*, 13:525–532, 1997.

[151] Rodrigo F. M. de Almeida, Aleksandre Fedorov, and Manuel Prieto. Sphingomyelin/Phosphatidylcholine/Cholesterol Phase Diagram: Boundaries and Composition of Lipid Rafts. *Biophysical Journal*, 85:2406–2416, 2003.

[152] Ryan White, Eric Ervin, Tinglu Yang, Xin Chen, Susan Daniel, Paul Cremer, and Henry White. Single Ion-Channel Recordings Using Glass Nanopore Membranes. *Journal of the American Chemical Society*, 129:11766–11775, 2007.